



SPACOMM 2016

The Eighth International Conference on Advances in Satellite and Space
Communications

ISBN: 978-1-61208-453-4

RESENS 2016

The International Symposium on Advances in Remote Sensing Technologies and Computation

February 21 - 25, 2016

Lisbon, Portugal

SPACOMM 2016 Editors

Timothy Pham, Jet Propulsion Laboratory/ California Institute of
Technology, USA

Kamal Harb, KFUPM, Saudi Arabia

SPACOMM 2016

Forward

The Eighth International Conference on Advances in Satellite and Space Communications (SPACOMM 2016), held between February 21-25, 2016 in Lisbon, Portugal, continued a series of events attempting to evaluate the state of the art in academia and industry on the satellite, radar, and antennas based communications, bringing together scientists and practitioners with challenging issues, achievements, and lessons learnt.

Significant efforts have been allotted to design and deploy global navigation satellite communications systems. Satellite navigation technologies, applications, and services still experience challenges related to signal processing, security, performance, and accuracy. Theories and practices on system-in-package RF design techniques, filters, passive circuits, microwaves, frequency handling, radars, antennas, and radio communications and radio waves propagation have been implemented. Services based on their use are now available, especially those for global positioning and navigation. For example, it is critical to identify the location of targets or the direction of arrival of any signal for civilians or on-purpose applications; smart antennas and advanced active filters are playing a crucial role. Also progress has been made for transmission strategies; multiantenna systems can be used to increase the transmission speed without need for more bandwidth or power. Special techniques and strategies have been developed and implemented in electronic warfare target location systems.

The conference had the following tracks:

- Signal processing in telecommunications
- Satellite and space communications

The conference also featured the following symposium:

- **RESENS 2016, *The International Symposium on Advances in Remote Sensing Technologies and Computation***

We take here the opportunity to warmly thank all the members of the SPACOMM 2016 technical program committee, as well as the numerous reviewers. The creation of such a high quality conference program would not have been possible without their involvement. We also kindly thank all the authors that dedicated much of their time and effort to contribute to SPACOMM 2016. We truly believe that, thanks to all these efforts, the final conference program consisted of top quality contributions.

Also, this event could not have been a reality without the support of many individuals, organizations and sponsors. We also gratefully thank the members of the SPACOMM 2016 organizing committee for their help in handling the logistics and for their work that made this professional meeting a success.

We hope SPACOMM 2016 was a successful international forum for the exchange of ideas and results between academia and industry and to promote further progress in the field of

satellite and space communications. We also hope that Lisbon, Portugal, provided a pleasant environment during the conference and everyone saved some time to enjoy the beauty of the city.

SPACOMM 2016 Advisory Committee

Stelios Papaharalabos, National Centre for Scientific Research "Demokritos", Greece

Piotr Tyczka, Poznan University of Technology, Poland

Michael Sauer, Corning Cable Systems, USA

Ling Pei, Finnish Geodetic Institute, Finland

SPACOMM 2016

Committee

SPACOMM 2016 Advisory Committee

Stelios Papaharalabos, National Centre for Scientific Research "Demokritos", Greece
Piotr Tyczka, Poznan University of Technology, Poland
Michael Sauer, Corning Cable Systems, USA
Ling Pei, Finnish Geodetic Institute, Finland

SPACOMM 2016 Technical Program Committee

Ashfaq Ahmed, Politecnico di Torino, Italy
Ayman Mahmoud Ahmed, NARSS-Cairo, Egypt
Mohamed Al-Mosawi, University of Portsmouth, UK
Petko Bakalov, ESRI Redlands CA, USA
Marco Baldi, Università Politecnica delle Marche - Ancona, Italy
Mark Bentum, University of Twente & ASTRON, The Netherlands
Igor Bisio, University of Genoa - Italy, Italy
Pierre Borne, Ecole Centrale de Lille, France
Shkelzen Cakaj, Telecom of Kosovo / Prishtina University, Kosovo / Polytechnic University of Tirana, Albania
Enzo Alberto Candreva, University of Bologna, Italy
Joseph C. Casas, NASA, USA
Emmanuel Chaput, IRIT-CNRS, France
Bruno Checcucci, Perugia University, Italy
Yao-Yi Chiang, Spatial Sciences Institute - University of Southern California, USA
Vittorio Dainelli, Rheinmetall Italia S.p.A. - Rome, Italy
Leonardo Dagui de Oliveira, Escola Politécnica da Universidade de Sao Paulo, Brazil
Francescantonio Della Rosa, Tampere University of Technology, Finland
Ke Deng, RMIT University, Australia
Felix Flentge, ESA/ESOC HSO-GIB - Darmstadt, Germany
Jie Gao, Stony Brook University, USA
Thierry Gayraud, LAAS-CNRS, Université de Toulouse, France
Mathieu Gineste, Thales Alenia Space, France
Erik Hoel, Esri, USA
Tzung-Pei Hong, National University of Kaohsiung, Taiwan
Suk-seung Hwang, Chosun University, Republic of Korea
Rajasekar Karthik, Oak Ridge National Laboratory, USA
Konstantinos Kontis, The University of Manchester, UK

Otto Koudelka, TU Graz, Austria
Anirban Kundu, Netaji Subhash Engineering College, India
Massimiliano Laddomada, Texas A&M University - Texarkana, USA
Haibin Liu, China Aerospace Engineering Consultation Center, China
Simona Lohan, Department of Electronics and Communications Engineering, Tampere University of Technology, Finland
Krešimir Malaric, University of Zagreb, Croatia
Herwig Mannaert, University of Antwerp, Belgium
Emmanouel T. Michailidis, University of Piraeus, Greece
Marina Mondin, Politecnico di Torino, Italy
Brian Niehoefer, TUV Informationstechnik GmbH, Germany
Nele Noels, University of Gent, Belgium
Stelios Papaharalabos, National Centre for Scientific Research "Demokritos", Greece
Ling Pei, Shanghai Jiao Tong University, China
Cathryn Peoples, Queen Mary University of London, UK
Dionysia K. Petraki, National Technical University of Athens, Greece
Timothy Pham, Jet Propulsion Laboratory / California Institute of Technology, USA
Prashant Pillai, University of Bradford, UK
Luigi Portinale, Università del Piemonte Orientale "A. Avogadro" - Alessandria, Italy
Ronald Raulefs, German Aerospace Center, Germany
Vincent Roca, INRIA Rhone-Alpes, France
Pedro Agustín Roncagliolo, University of La Plata, Argentina
Alexandru Rusu-Casandra, Politehnica University of Bucharest, Romania
Heung-Gyoon Ryu, Chungbuk National University, Republic of Korea
Michael Sauer, Corning Cable Systems, USA
Paresh Saxena, Ansur Technologies, Barcelona, Spain
Ana Maria Sierra Diaz, Telefónica I+D - Madrid, Spain
Jens Timmermann, Cooperative State University (DHBW) Ravensburg, Germany
Yosef Gavriel Tirat-Gefen, Castel Research Inc., USA
Piotr Tyczka, Poznan University of Technology, Poland
Ouri Wolfson, University of Illinois, USA
Xi Zhang, Illinois Institute of Technology, USA
Huiyu Zhou, Queen's University Belfast, UK
Qiang Zhu, University of Michigan, USA
Zhiwen Zhu, Communications Research Centre Canada, Canada

RESENS 2016

RESENS 2016 Technical Program Committee

Agnes Begue, UMR-TETIS, France
Jean-Marc Delvit, CNES, France
Ronan Fablet, Institut Telecom/Telecom Bretagne, France
Feng Gao, USDA-ARS Hydrology & Remote Sensing Lab, USA

Olaf Hellwich, Technische Universität Berlin, Germany

Laurent Linguet, University of French Guiana, France

Keith Morrison, Cranfield University, UK

Giorgio Pasquettaz, CRF, Italy

Irina Sergievskaya, Institute of Applied Physics of Russian Academy of Sciences, Russia

Zhengwei Yang, National Agricultural Statistics Service - United States Department of Agriculture, USA

Copyright Information

For your reference, this is the text governing the copyright release for material published by IARIA.

The copyright release is a transfer of publication rights, which allows IARIA and its partners to drive the dissemination of the published material. This allows IARIA to give articles increased visibility via distribution, inclusion in libraries, and arrangements for submission to indexes.

I, the undersigned, declare that the article is original, and that I represent the authors of this article in the copyright release matters. If this work has been done as work-for-hire, I have obtained all necessary clearances to execute a copyright release. I hereby irrevocably transfer exclusive copyright for this material to IARIA. I give IARIA permission to reproduce the work in any media format such as, but not limited to, print, digital, or electronic. I give IARIA permission to distribute the materials without restriction to any institutions or individuals. I give IARIA permission to submit the work for inclusion in article repositories as IARIA sees fit.

I, the undersigned, declare that to the best of my knowledge, the article does not contain libelous or otherwise unlawful contents or invading the right of privacy or infringing on a proprietary right.

Following the copyright release, any circulated version of the article must bear the copyright notice and any header and footer information that IARIA applies to the published article.

IARIA grants royalty-free permission to the authors to disseminate the work, under the above provisions, for any academic, commercial, or industrial use. IARIA grants royalty-free permission to any individuals or institutions to make the article available electronically, online, or in print.

IARIA acknowledges that rights to any algorithm, process, procedure, apparatus, or articles of manufacture remain with the authors and their employers.

I, the undersigned, understand that IARIA will not be liable, in contract, tort (including, without limitation, negligence), pre-contract or other representations (other than fraudulent misrepresentations) or otherwise in connection with the publication of my work.

Exception to the above is made for work-for-hire performed while employed by the government. In that case, copyright to the material remains with the said government. The rightful owners (authors and government entity) grant unlimited and unrestricted permission to IARIA, IARIA's contractors, and IARIA's partners to further distribute the work.

Table of Contents

Industrial Wireless Sensor Networks (ISWN): Requirements and Solutions <i>Abdullah Al-Yami, Wajih Abu-Al-Saud, Kamal Harb, and Baqer Al-Ramadan</i>	1
The Design of Sparse and Non-sparse FIR Filters Using Linear Complementarity Problem Approach <i>Muhammad Muzammal Naseer, Kamal Harb, and Ahmad Nuseirat</i>	7
Measurements of UWB Propagation and Transmission for Wireless Links in Spacecrafts <i>Miyuki Hirose and Takehiko Kobayashi</i>	12
Mode Selection Algorithm for Advanced TOA Trilateration Techniques <i>Sajina Pradhan and Suk-seung Hwang</i>	18
Playback Data Analysis Utility for a LEO Satellite <i>Dongseok Chae</i>	23
Preliminary Design of S-AIS Payload for KOMPSAT-6 <i>Yong-Min Lee, Jin-Ho Jo, and Byoung-Sun Lee</i>	27
Performance Analysis of Operational Ka-band Link with Kepler <i>Timothy Pham and Jason Liao</i>	30
Simulation of SAR Jammer Techniques and Hardware Implementation for Point Scatterer Modelling <i>Emrah Ener</i>	36
Fast and Efficient Satellite Imagery Fusion Using DT-CWT and WZP <i>Yonghyun Kim, Jaehong Oh, and Yongil Kim</i>	42

Industrial Wireless Sensor Networks (ISWN): Requirements and Solutions

Abdullah Al-Yami, Wajih Abu-Al-Saud, Kamal Harb, and Baqer Al-Ramadan
 abdullah.yami.22@aramco.com, kharb@uohb.edu.sa, {Wajih, Bramadan}@kfupm.edu.sa
 KFUPM, Dhahran, Saudi Arabia

Abstract—Industrial Wireless Sensor Networks (IWSN) are preferred over bulky wired networks in industrial monitoring and automation. These sensors are used to access locations, which are technically unreachable. The use of IWSN not only reduced the cost of automation systems but also played a significant role in alarm management by real time data transfer. ZigBee and WirelessHART are already deployed protocols for IWSN. ISA100.11a developed by International Society of Automation was specially designed for IWSN. The main features of this standard are low power consumption, real time fast data transfer, scalability, security, reliability, co-existence with other network architectures and robustness in harsh industrial environments. To achieve these features, these protocols use layer structure, which provides security, fast and reliable data transfer. IEEE 802.15.4 is used at its physical layer with variable data slots. This paper presents the results of the simulation of ISA100 done on Pymote framework which is extended by one of the authors. A test bed is implemented in the lab using the Yokogawa field devices. This paper discusses the simulated and practical results obtained from operation of ISA100.11a.

Keywords—ISA100.11a; Yokogawa field wireless devices; Industrial wireless sensor networks; IWSN; OMNET++;

I. INTRODUCTION

Wireless Sensor Networks (WSN) [1][2] are small sensors that are deployed in remote locations to sense particular conditions and send information pertaining to these conditions to a Central Control Room (CCR). WSN are ad hoc in nature and their number is often large. They work with limited resources and are usually non replaceable. WSN have endless applications; it can be used in defense to monitor borders. They are also used by environmentalists to monitor environmental changes such as temperature and humidity in certain regions. For industries, WSNs can sense temperature, pressure, etc. of certain devices. WSN have certain limitations such as low range, small battery size, and non-reusable structure which require a very resource efficient algorithm. Industrial Wireless Sensor Network (IWSN) evolved from WSN and are specially designed keeping in mind the demands and nature of industry [1]-[4].

IWSNs use replaceable batteries and generally have wider range than WSNs. IWSNs have an edge over traditional wired structures since they can be installed easily anywhere in industry without heavy support structures. IWSNs can also work efficiently where wired networks are technically not installable such as on moving or rotating objects.

Another important industrial requirement is the stability of the system. The system should be stable and easy to handle and maintain [5]. Also, deployed networks should be reliable and secure with high data rate support. Many protocols are developed that support the above functionalities. Zigbee is a wireless open global standard

which satisfies the unique needs of low power, low cost and wireless mobile-to-mobile (M2M) networking. It is also used in IWSNs [6]. Zigbee is standardized by Zigbee alliance which consists of more than 300 companies. It can support star, mesh and tree topologies [7][8].

Another developed protocol is Highway Addressable Remote Transducer Protocol commonly known as WirelessHART and approved by International Electrotechnical Commission (IEC). WirelessHART is simple, secure, reliable, and uses TDMA with mesh topology. HART, like OSI model, uses many layers that add to security, integrity and reliability of the system [9]. The power consumption of HART is low compared to Zigbee with high security standard.

ISA100, designed by International Society of Automation, supports high data rates up to 250 Kbps. Security and Integrity is provided by layered architecture. 6LoWPAN, used in network layer, provides efficient routing and also enables IWSN to co-exist with other IWSN protocols. At the level of Physical Layer, IEEE 802.15.4 is used, which uses Carrier Sense Multiple Access with Collision Avoidance (CSMA-CA) [4][10][11]. ISA works on 2.4 GHz free band with 16 channels. Transmitter complexity is significantly decreased by using Orthogonal Quadrature Phase Shift Keying (O-QPSK), which avoids the zero state and thus has a constant envelope transmission [12][13].

ISA100 uses the following layers to optimize performance:

1. A graphical user interface at its application layer.
2. For fast and reliable data transfer, UDP is used at the transport layer.
3. At the network layer, IPV6 over Low power Wireless Personal Area Network (6LoWPAN) which can work with other networks.
4. At the data link layer, variable slot scheme is used.
5. IEEE 802.15.4 is used at the physical layer, which is spectrally efficient and minimizes collisions between the adjacent nodes.

IWSN protocols usually use two type of devices to send data to CCR.

- 1) Field devices whose prime function is to sense the data and transmit it.
- 2) Gateway devices are responsible for receiving data and providing reliable transmission to CCR. Field devices can also reroute the packet to gateway devices. Far end devices usually transfer data over more than one hop.

TABLE I. ZIGBEE TEST OUTPUT FOR HUMIDITY AND TEMPERATURE.

Device	09:00 AM	10:00 AM	11:00 AM	12:00 PM	01:00 PM	02:00 PM	03:00 PM
2091	6302.2	6610.5	6785.4	7583.3	8714.4	9341.3	8184.7
2094	6328.1	6590.7	6767.0	6910.9	6974.3	7000.3	8126.4
2103	6346.5	6628.2	6835.1	7902.9	8350.3	9231.3	8135.6
2105	6324.3	6514.1	6738.8	6898.2	7324.0	7480.0	7411.3
2107	6335.0	6635.3	6824.5	7612.7	8846.6	9494.0	7964.1

This paper provides a lab test evaluation of both indoor and outdoor Zigbee, WirelessHART and ISA100-based systems. The kit presented in Figure 1 is used for Zigbee testing. Zigbee tests are performed on Memsic WSN kits. The topologies and results are compared. The remaining part of the paper simulates the ISA100 on Pymote, which is a Python based framework for WSN simulation and was extended to support our simulation.

This paper is described in four sections. Section II describes the lab test by using Zigbee and WirelessHART protocol. Section III presents ISA100 simulation. The purpose of the ISA100 is to find the appropriate range and terrain of the IWSN. It also describes different methods related to wireless communications. Discussion and results are also presented. Finally, we conclude this study in Section IV.

II. LAB TEST

A. Zigbee Test

Zigbee is currently the oldest and most widely used WSN protocol. Many vendors provide Zigbee-based products [7]. Memsic Inc. is one such manufacturer, whose devices can be used for conducting outdoor tests. These devices are able to sense voltage, humidity, temperature and pressure in a particular location. Their WSN kit provides an end-to-end enabling platform for the creation of wireless sensor networks. A windows application called MoteView is provided as an interface between a user and the deployed sensor network. MoteView also provides the tools to simplify deployment and monitoring. It also makes it easy to connect to a database, to analyze, and to graph sensor readings. It also provides node health statistics in terms of transmission quality, number of drop packets, retries, etc.

The topology for our experiment is shown in Figure 1. Devices numbered 2091, 2094, 2103, 2105, 2107 as presented in TABLE I. act as sensor devices which sense the above mentioned parameters and send them to gateway device GW.

Upon receiving the data, the GW displays the transmitted values in a GUI and alarms are raised if some parameter makes an abrupt change. For illustration, one of the collected parameters containing humidity and temperature (Humtemp) is shown in TABLE I.

At the start of the test, packets started flowing from sensor devices to the gateway device at regular intervals. TABLE I. shows the Humtemp data received from sensor devices averaged over an hour.

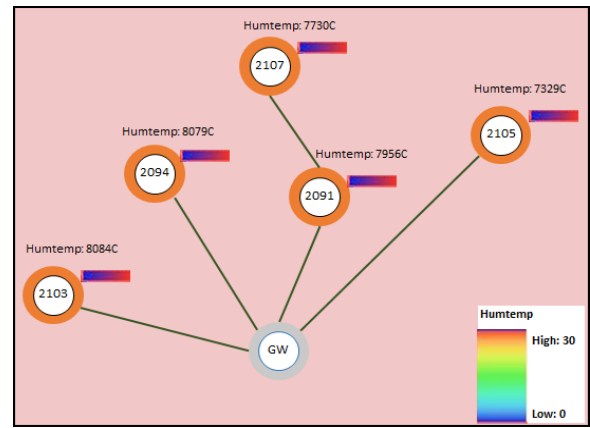


Figure 1. Topology for humidity/temperature measurements.

B. WirelessHART Test

Another industrial protocol is WirelessHART, which can coexist with other networks. This test is performed on Emerson devices, which use HART as shown in 0. Like other devices, the kit composes of sensor and gateway devices, where the used topology is shown in Figure 2, which serve to collect and transfer data.

The HART uses mesh protocol and when the setup is turned on, each device is connected to every other device in its range. The link configuration and stability according to the device tags is shown in Figure 2, which explains the link of gateway with the sensor nodes. It also shows the number of neighbor sensors against every device as well. The reliability of the link and Received Signal Strength Intensity (RSSI) is also depicted.

C. ISA100 Test

The purpose of this experiment is to find the appropriate range and terrain of the IWSN. Instruments used for testing are the Yokogawa wireless kit shown in Figure 3, which consist of field and gateway devices. If the path stability or reliability decreases as a result of any environmental change, the device will try to switch to an alternative path.

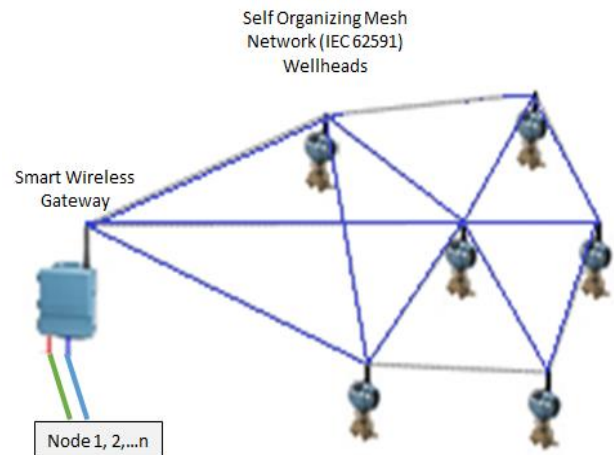


Figure 2. Wireless HART test topology.

TABLE II. GUI APPLICATION OF HART TEST.

HART Tag	Node state	Active neighbors	Neighbors	Service Denied	Reliability	Missed Updates	Path Stability	RSSI	Joins	Join Time
385PT0026A		SFNY 385PT0701B 385PT0211B 385PT0501B	4		100.0%	0	100.0%	-49 dB	1	11/24/11 23:21:44
385PT0211B		SFNY 385PTT0806 385PT0026A 385PT0501B	4		100.0%	0	100.0%	-44 dB	1	11/24/11 23:21:26
385PT0501B		SFNY 385PT0211B 385PT0026A	3		100.0%	0	100.0%	-57 dB	1	11/24/11 23:20:35
385PT0701B		SFNY 385PT0026A	2		100.0%	0	100.0%	-49 dB	1	11/24/11 23:21:50
385PT0806		SFNY 385PT0211B 385PT0807	3		100.0%	0	100.0%	-44 dB	1	11/24/11 23:21:02
385TT0807		SFNY 385PTT0806	2		100.0%	0	100.0%	-60 dB	1	11/24/11 23:21:08



Figure 3. Yokogawa field device kit.

The test was performed in two terrains, namely Plane ground and Rough ground (in which there are buildings and structures separating the field device from the gateway device). Two different environments are chosen so as to find the attenuation and signal degradation in the two surface cases.

These experiments were conducted at King Fahad University of Petroleum and Minerals (KFUPM) in an outdoor environment. Figure 3 shows the real test on rough ground. Topologies used for this experiment for the irregular and regular surfaces are shown in Figure 4 and

Figure 5, respectively. A temperature sensor and two pressure sensors are used to sense the data and transfer it to the gateway device. TABLE III. shows the device type and tags used.

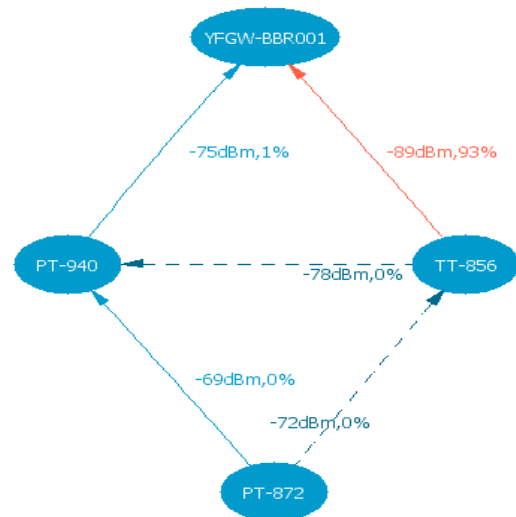


Figure 4. ISA100 test for irregular surface.

ISA100 takes into account the direct communication node and neighboring node for data transfer and in case if one node goes down it can automatically switch to another route based on the Packet Error Rate (PER) and RSSI. In the two topologies, we have seen that the sensor devices are connected to the gateway device directly or indirectly.

There are two kinds of connections shown in the topologies. Solid lines are actual communication routing between the device and gateway. In Figure 4, the device TT-856 was experiencing a higher PER while communicating to gateway device. Dotted lines are alternate routes, which are used in case of fault or errors. For each link, the RSSI and PER as a percentage are indicated.

TABLE III. ISA100 DEVICE TAGS AND TYPES.

Device TAG	Functionality	Type
PT-872	IO Device +Router	Pressure Sensor
PT-940	IO Device +Router	Pressure Sensor
TT-856	IO Device +Router	Temperature Sensor
YFGW-BBR001	Gateway Device	Gateway Device

As the direct link was noisy, so the data was transmitted by alternate route. A detailed statistics after collecting data from the two terrains is clearly shown in TABLE IV. Here, we can see the low RSSI and high PER being highlighted.

D. Discussion

In the lab test, protocols stack that are available in the market are tested. Zigbee is the earliest with simple protocol set. HART and ISA100 are developed later with high data rate, efficiency and reliability. Zigbee application does not show the network related stats but depicts a clear picture of the parameters. HART on the other hand has support to the other networks and it can also show the clear picture of network elements in GUI. ISA100 significantly shows good results in different terrains. These lab tests help in understanding the difference in protocols and application level support provided by the vendors in industry.

III. ISA100 SIMULATION

Simulation has always been very popular among network-related research. Several simulators have been developed to implement and study algorithms for wireless networks. Some are general purpose while others are design for specific purpose and vary in features and the level of complexity. They support certain hardware and communication layers assumptions, and provide set of tools for deployment scenarios, modeling, analysis, and visualization. Classical simulation tools include NS-2/3, OPNET, OMNeT++, J-Sim, and TOSSIM [14][15][16].

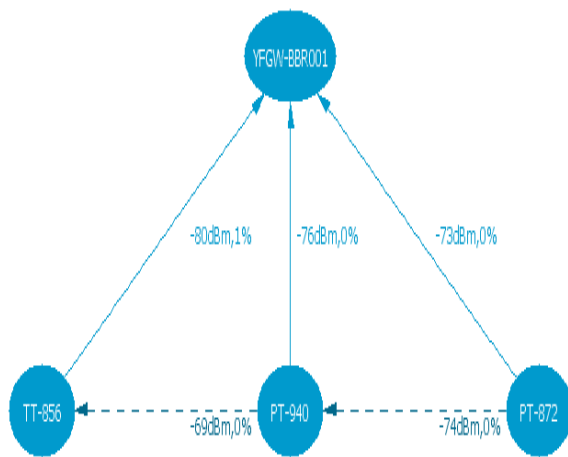


Figure 5. ISA 100 test for plane surface.

TABLE IV. NETWORK STATISTICS COLLECTED FROM ISA TEST.

Device TAG	Average Distance		Average RSSI (dBm)		Average PER (%) and Hop count	
	Flat Terrain	Rough Terrain	Flat Terrain	Rough Terrain	Flat Terrain	Rough Terrain
PT-872	600 m	1000 m	-73	-69	0 / 1	0 / 2
PT-940	600 m	1000 m	-76	-75	0 / 1	1 / 1
TT-856	600 m	1000 m	-81	-89	0 / 1	93 / 1
				-75		0.63 / 2

After some research, we concluded that Python-based tools completely fulfill our requirements. We decided to use Pymote, which is a high level Python library specifically designed for wireless networks to perform event based simulation of distributed algorithms [17][18]. The user can implement their ideas in Python; which has become popular in academia and industry. The library is developed without much abstraction and therefore can be used or extended using Python's highly expressive native syntax. The library particularly focuses on fast and accurate implementation of ideas at algorithm level using formally defined distributed computing environment.

A. The Simulation

The base station is placed in middle of n randomly deployed EHWSN nodes over a 600 m by 600 m area. We consider registration and data packet sizes of 100 bytes while the acknowledgment packet size of 15 bytes. Some other parameters are shown in TABLE V. 5.

A simple topology generated for simulation using the Pymote is shown in Figure 6. The center node (#1) acts as the base station for the other nodes (numbered 2 to 11). First, we evaluate the performance by changing the number of nodes (from 5 to 50). In this simulation, we kept the fixed data rate of one message every 5 seconds. Secondly, we vary the data rate from one message every 5 seconds to a message every second and keep the number of nodes fixed at 10.

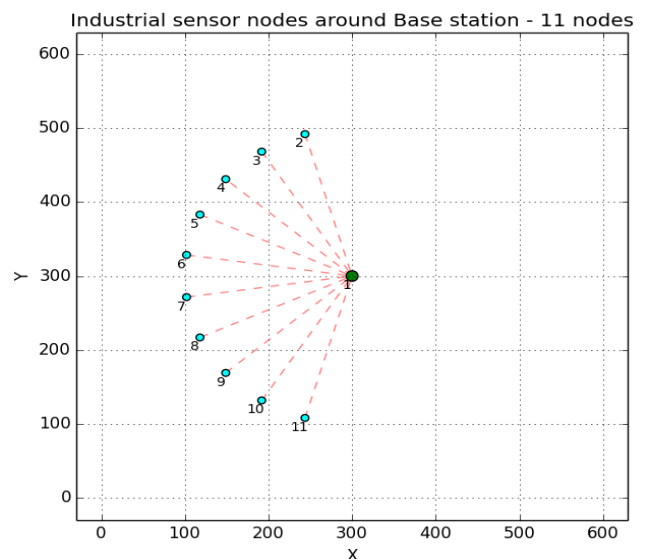


Figure 6. Topology with 10 nodes.

TABLE V. Simulation parameters.

Parameter	Name	Value
Min. Received signal power threshold	P_RX_THRESHOLD	-70 dbm
Frequency	FREQ	2.4 Ghz
n	No. of nodes	5 - 50
S_d	Data packet size	100 bytes
S_a	Ack packet size	15 bytes

Energy consumption for all nodes combined, and base station (in mJoules). The results for simulation run for 5 to 45 nodes (with increment of 5) is shown in Figure 7. Count of received packet and lost packets at the base station are also shown in the same figure.

For the following simulation, the number of nodes are kept fixed at 10 and monitor the link quality index (LQI) and RSSI of received signal at the base station when nodes were sending data at variable rate. The SNR levels are shown in Figure 8. The simulation results are comparable with the experimental results in terms of PER and RSSI.

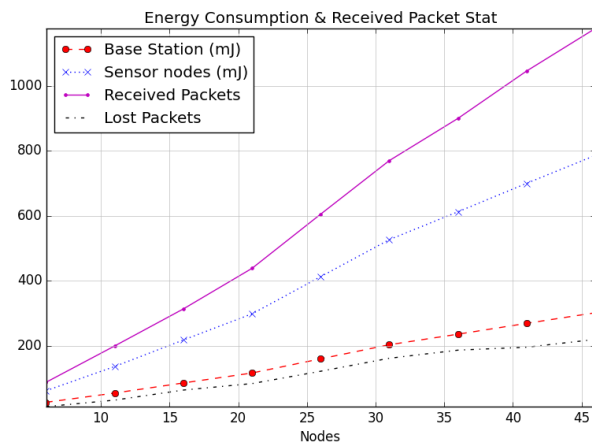


Figure 7. Energy consumption and stats at base station.

IV. CONCLUSION

In this paper, we have studied and conducted the lab test of Zigbee, Wireless HART and ISA100. The results are compared and analyzed in order to evaluate the best protocol for IWSNs. ISA100 was also simulated using the Pymote framework Based on the studies it can be concluded that ISA100 is better than HART and far better than Zigbee protocol. ISA100 uses CSMA-CA with OQPSK, which make it efficient at its physical layer. For routing, IPV6 helps ISA100 to coexist with any other legacy network. IPV6 also helps to carry traffic over a network without any routing gateway support. The Yokogawa field wireless kit offers a far better range that is greater than 800 meters, which is suitable for bigger industries and cuts the cost of additional gateway devices used to connect all the edges in a factory. The results of the simulation of ISA100 done on Pymote framework are comparable with the experimental results.

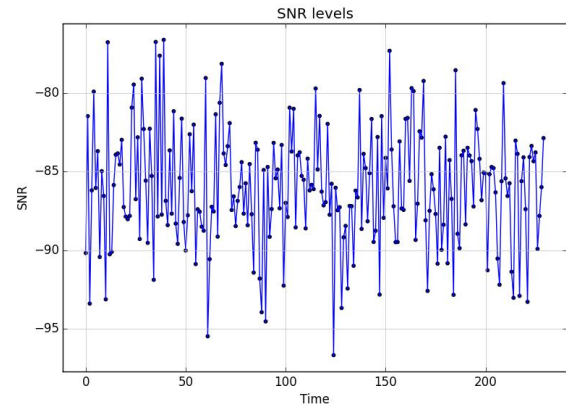


Figure 8. SNR of received signal at base station.

ACKNOWLEDGMENT

The authors wish to thank the management of Saudi Aramco for supporting this research and for facilitating the logistics needed for installing IWSN system and collecting data. In addition, the experiment was made possible by the support of Yokogawa and Emerson who supplied the gateway and field devices.

REFERENCES

- [1] I. Akyildiz, W. Su, Y. Sankarasubramaniam, and E. Cayirci, "A survey on sensor networks," *IEEE Communications Magazine*, Aug. 2002, vol. 40, no. 8, pp. 102–114.
- [2] A. Al-Yami, K. Harb, and S. H. Abdul-Jauwad, "Industrial Wireless Sensor Networks in the Perspective of Diversity and Spectral Efficiency," *Proc. of the IEEE 11th Malaysia International Conference on Communication (MICC 2013)*, Malaysia, Kuala Lumpur, Nov. 2013, pp. 390–395.
- [3] M.-S. Pan and Y.-C. Tseng, "Communication Protocols and Applications for Zigbee-Based Wireless Sensor Networks," *Taiwan-French Conference on Information Technology*, March 2006, pp. 1–8.
- [4] A. Al-Yami and W. Abu-Al-Saud, "Practical vs. Simulated Results of ISA100 Physical Layer," *Proc. of the IEEE Sixth International Conference on Intelligent Systems, Modelling and Simulation*, Malaysia, Feb. 2015, pp. 226–230.
- [5] A. Willig, K. Matheus, and A. Wolisz, "Wireless Technology in Industrial Networks," *Proceedings IEEE*, June 2005, Vol. 93, no. 6, pp. 1130–1151.
- [6] J. Song, S. Han, A. K. Mok, D. Chen, M. Lucas, and M. Nixon, "WirelessHART: Applying Wireless Technology in Real-Time Industrial Process Control," *Real-Time and Embedded Technology and Applications Symposium (RTAS) IEEE*, April 2008, pp. 377–386.
- [7] Zigbee alliance, "ZigBee: The Open, Global Wireless Standard for Connecting Everyday Devices," Website: <http://zigbee.org>, last accessed date Oct. 2015.
- [8] J. P. Thomese, "Fieldbus Technology in Industrial Automation," *proceedings of the IEEE*, June 2005, Vol. 93, no. 6, pp. 1073–1101.
- [9] P. Ferrari, A. Flammini, S. Rinaldi, and E. Sisinni, "Performance assessment of a WirelessHART network in a real-world testbed," *IEEE International in Instrumentation and Measurement Technology Conference (MTC)*, May 2012, pp. 953–957.
- [10] N. Q. Dinh, K. Sung-Wook, and K. Dong-Sung, "Performance evaluation of priority CSMA-CA mechanism on ISA100.11a wireless network," *Computer Standards & Interfaces*, Elsevier, Jan. 2012, vol. 34, no. 1, pp. 117–123.
- [11] P. Park, P. D. Marco, P. Soldati, C. Fischione, and K. H. Johansson, "A Generalized Markov Chain Model for Effective Analysis of Slotted IEEE 802.15.4," *Mobile Adhoc and Sensor Systems, IEEE 6th International Conference*, Macau, Oct. 2009, pp. 130–139.

- [12] M. Nixon, "A Comparison of WirelessHART and ISA100.11a," Whitepaper, Emerson Process Management, July 2012, pp. 1–36.
- [13] ISA100 Wireless Compliance Institute, "Isa100 wireless systems for automation," Website: <https://www.isa.org/isa100/>, last accessed date Sept. 2015.
- [14] A. Sobeih, W. Chen, J. Hou, and L. Kung, "J-sim: A simulation environment for wireless sensor networks," in Proceedings of the 38th annual Symposium on Simulation. IEEE Computer Society Washington, DC, USA, 2005, pp. 175–187.
- [15] Q. Ali, A. Abdulmaojod, and H. Ahmed, "Simulation & Performance Study of Wireless Sensor Network (WSN) Using MATLAB," 1st International Conference on Energy, Power and Control (EPC-IQ), Nov. 2010, pp. 307–314.
- [16] I. A. Qutaiba (2012), Simulation Framework of Wireless Sensor Network (WSN) Using MATLAB/SIMULINK Software, MATLAB - A Fundamental Tool for Scientific Computing and Engineering Applications - Volume 2, Prof. Vasilios Katsikis (Ed.), ISBN: 978-953-51-0751-4, InTech, DOI: 10.5772/46467. Available from: <http://www.intechopen.com/books/matlab-a-fundamental-tool-for-scientific-computing-and-engineering-applications-volume-3>, last accessed date Oct. 2015.
- [17] Y. Tselishchev, A. Boulis, and L. Libman, "Experiences and Lessons from Implementing a Wireless Sensor Network MAC Protocol in the Castalia Simulator," Wireless Communications and Networking Conference (WCNC), 2010 IEEE, April 2010, vol. 1, no. 6, doi: 10.1109/WCNC.2010.5506096, pp. 18–21.
- [18] D. Arbula and K. Lenac, "Pymote: High Level Python Library for Event-Based Simulation and Evaluation of Distributed Algorithms," International Journal of Distributed Sensor Networks, Dec. 2012, vol. 2013, pp. 1-12.

The Design of Sparse and Non-Sparse FIR Filters using Linear Complementarity Problem Approach

Muhammad Muzammal Naseer, Kamal Harb, Ahmad Nuseirat

Electrical Engineering Department

KFUPM/UOHB University, Saudi Arabia

Email: 1- muz.pak@gmail.com; 2- kamal_harb@hotmail.com; 3- anuseirat@anu.edu.jo

Abstract—In this article, the problem of linear phase finite impulse response (FIR) filter design is reconsidered as a linear complementarity problem (LCP) with a weighting strategy. The LCP is not an optimization technique because there is no objective function to optimize; however, quadratic programming, one of the applications of LCP, can be used to find an optimal solution for the 1D FIR filter. Quadratic programs are an extremely important source of applications of LCP; in fact, several algorithms for quadratic programs are based on LCP. It has been shown that, by selecting proper weights, the LCP approach is capable of producing equiripple response. Since length of the impulse response of discrete time filters is often an indicator of computational cost, an algorithm is proposed that iteratively thins the impulse response of a non-sparse filter. The resulting LCP has been solved by a computationally effective Lemke's algorithm. Different examples are presented to illustrate the efficiency of the proposed methods.

Keywords—Finite Impulse Response (FIR); Lemke's algorithm; Linear Complementarity Problem (LCP); Quadratic Program (QP).

I. INTRODUCTION

The linear phase finite impulse response (FIR) filters are essential in many applications and there are many well documented techniques in literature for designing such filters [1]–[10]. In [3], Vaidyanathan et. al designed the linear phase FIR filters by minimizing a quadratic measure of the error in the passband and stopband. In [4], Medlin et. al introduced the Lagrange multiplier method to design FIR filters for multirate applications. In [5], M. H. Er and C. K. Siew presented the FIR filter design problem as a quadratic program (QP) with quadratic constraints. Rabiner [2] used the theory of linear programming to design discrete time FIR filters with equiripple response. Nuseirat [1] studied the design problem using the LCP approach.

The classical LCP has been explicitly stated by Du val in 1940 [11]. The LCP is not an optimization technique as there is no objective function to optimize, however, QP, one of the applications of LCP, can be used to find an optimal solution for the linear phase FIR filter. QPs are extremely important source of application for the LCP. There are several highly effective algorithms for solving QPs that are based on the LCP [9] [11].

In filter design problems, it is required to optimize a desired frequency response by minimizing an error norm, which can be measured in L_2 or L_∞ norm. L_2 is

known for its poor performance especially at band edges (*Gibb's Phenomenon*). In [1], the author tried to improve the performance by simply removing the transition region from the error measure but the presented examples show that a compromise has to be made at one of the band edges.

We revisit the problem with a weighting strategy and show that QP converted into LCP is capable of producing equiripple response filters comparable with Park and McClellan [6] who used polynomial interpolation technique to solve for the desired filters. The resulted LCP-QP is solved by the most robust Lemke's algorithm. Based on pivoting, Lemke is a direct algorithm. It is computationally very effective as no matrix inversion is needed [1].

In many applications, the number of arithmetic operations indicate the cost of implementation, thus reducing the length of impulse response that is designing sparse filters is beneficial not only in terms of computational cost but also in hardware and energy consumption [13] [14]. Sparse filters offer opportunity to omit the arithmetic operations associated with zero-valued coefficients. In this article, a simple iterative algorithm is proposed to reduce the number of coefficients of a non-sparse filter.

This paper is organized as follows: Section II presents the problem formulation, and shows the effect of LCP-QP with weights on the design problem. Section III describes an iterative algorithm to thin the impulse response. Section IV presents the discussion and simulation results. Finally, we conclude in Section V.

II. PROBLEM FORMULATION

For simplicity of presentation, consider the frequency response of type I FIR filter given by [1] [13] [14]:

$$H(\omega) = \sum_{n=0}^{N-1} h(n) \cos(\omega n), \quad (1)$$

where $\{h_n\}$, $n = 0, \dots, N-1$ is the impulse response. Discretizing ω as ω_k , $1 \leq k \leq L$, the frequency response in (1) can be written in the following matrix form:

$$\mathbf{H} = \mathbf{C}\mathbf{h}, \quad (2)$$

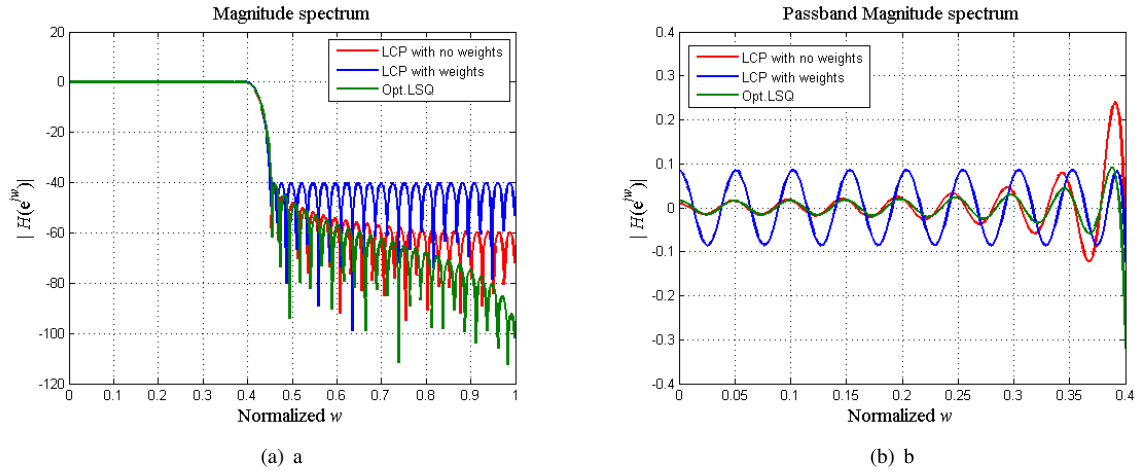


Figure 1. Performance comparison of LCP with and without weights compared with the optimal least square method. It is clear that with appropriate weights LCP approach is capable of producing FIR filters with equiripple response.

where

$$\mathbf{C} = \begin{bmatrix} 1 & \cos(w_1) & \dots & \dots & \cos(Nw_1) \\ \vdots & \vdots & \vdots & \vdots & \vdots \\ 1 & \cos(w_m) & \dots & \dots & \cos(Nw_m) \\ \vdots & \vdots & \vdots & \vdots & \vdots \\ 1 & \cos(w_L) & \dots & \dots & \cos(Nw_L) \end{bmatrix}$$

and

$$\mathbf{h} = [h[0] \quad h[1] \quad \dots \quad h[N-1] \quad h[N]]^T$$

Since LCP is solved for a positive vector, the impulse response has to be written as a difference of two non-negative vectors [1]:

$$\mathbf{h} = \mathbf{h}^+ - \mathbf{h}^- \quad (3)$$

Using (2) and (3), the frequency response of a discrete time filter becomes [1]:

$$\mathbf{H} = \mathbf{B}\mathbf{d}, \quad (4)$$

where $\mathbf{B} = [\mathbf{C} \quad -\mathbf{C}]$ and $\mathbf{d} = \begin{bmatrix} \mathbf{h}^+ \\ \mathbf{h}^- \end{bmatrix}$. For a desired frequency response \mathbf{D} , error vector will be [1]:

$$\mathbf{E} = \mathbf{B}\mathbf{d} - \mathbf{D}. \quad (5)$$

The problem of finding \mathbf{h} can be formulated by minimizing the squared error [1]:

$$\begin{aligned} &\text{Minimize } \varepsilon(\mathbf{d}) = \mathbf{E}^T \mathbf{E} \\ &\text{Subject to} \\ &|\mathbf{W} \times \mathbf{E}| \leq \delta, \end{aligned} \quad (6)$$

where \mathbf{W} is a strictly positive weighting vector and δ , is the tolerance scheme. The objective function in (6) can be written as:

$$\begin{aligned} \varepsilon(\mathbf{d}) &= \mathbf{E}^T \mathbf{E}, \\ &= (\mathbf{B}\mathbf{d} - \mathbf{D})^T (\mathbf{B}\mathbf{d} - \mathbf{D}), \\ &= (\mathbf{d}^T \mathbf{B}^T - \mathbf{D}^T) (\mathbf{B}\mathbf{d} - \mathbf{D}), \\ &= \mathbf{d}^T \mathbf{B}^T \mathbf{B}\mathbf{d} - \mathbf{d}^T \mathbf{B}^T \mathbf{D} - \mathbf{D}^T \mathbf{B}\mathbf{d} + \mathbf{D}^T \mathbf{D}, \quad (7) \\ &= \mathbf{d}^T \mathbf{B}^T \mathbf{B}\mathbf{d} - 2\mathbf{d}^T \mathbf{B}^T \mathbf{D} + \mathbf{D}^T \mathbf{D}. \end{aligned}$$

$$\varepsilon(\mathbf{d}) = \frac{1}{2} \mathbf{d}^T \mathbf{Q}\mathbf{d} - \mathbf{d}^T \mathbf{R} + \mathbf{D}^T \mathbf{D},$$

where $\mathbf{d} \in R^{2N+2}$, $\mathbf{Q} = 2\mathbf{B}^T \mathbf{B}$ is symmetric and semi-positive definite matrix and $\mathbf{R} = 2\mathbf{B}^T \mathbf{D}$. The linear constraints in problem (6) can be written in a compact form as follows:

$$\begin{aligned} &|\mathbf{W} \times \mathbf{E}| \leq \delta \\ &|\mathbf{B}\mathbf{d} - \mathbf{D}| \leq \frac{\delta}{\mathbf{W}} \\ &\underbrace{\begin{bmatrix} \mathbf{B} \\ -\mathbf{B} \end{bmatrix}}_{\mathbf{A}} \mathbf{d} \leq \underbrace{\begin{bmatrix} \mathbf{D} + \frac{\delta}{\mathbf{W}} \\ -\mathbf{D} + \frac{\delta}{\mathbf{W}} \end{bmatrix}}_{\mathbf{b}}. \end{aligned} \quad (8)$$

In compact form, the above minimization problem becomes [1]:

$$\begin{aligned} &\text{Minimize } f(\mathbf{d}) = \frac{1}{2} \mathbf{d}^T \mathbf{Q}\mathbf{d} - \mathbf{d}^T \mathbf{R} + \mathbf{D}^T \mathbf{D} \\ &\text{Subject to} \\ &\mathbf{A}\mathbf{d} \leq \mathbf{b} \\ &\mathbf{d} \geq 0. \end{aligned} \quad (9)$$

The Kuhn-Tucker necessary conditions for the above QP in (9) are that there must exist vectors $\mathbf{u} \in R^{2N+2}$, $\mathbf{v} \in R^{2L}$, $\lambda \in R^{2L}$ such that [1] [9] [11]:

$$\begin{aligned} &-\mathbf{R} + \mathbf{Q}\mathbf{d} + \mathbf{A}^T \lambda - \mathbf{u} = 0, \\ &\mathbf{A}\mathbf{d} + \mathbf{v} = \mathbf{b}, \\ &\mathbf{u} \geq 0, \quad \mathbf{v} \geq 0, \quad \mathbf{d} \geq 0, \quad \lambda \geq 0, \quad \mathbf{u}^T \mathbf{d} = 0, \quad \mathbf{v}^T \lambda = 0. \end{aligned} \quad (10)$$

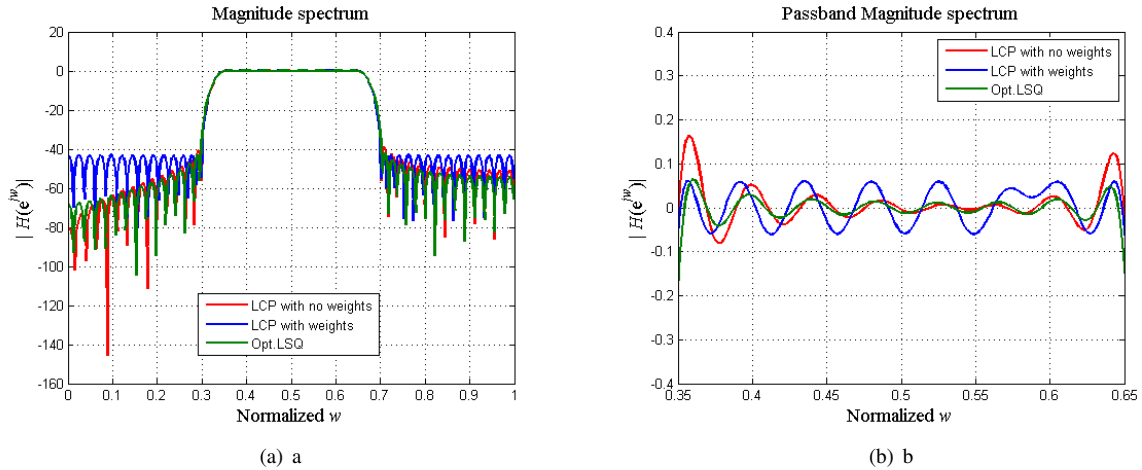


Figure 2. Performance comparison of LCP with and without weights compared with the optimal least square method. Again with appropriate weights, the LCP approach produces equiripple response.

Clearly, this can be written as:

$$\begin{pmatrix} \mathbf{u} \\ \mathbf{v} \end{pmatrix} \equiv \begin{pmatrix} -\mathbf{R} \\ \mathbf{b} \end{pmatrix} + \begin{pmatrix} \mathbf{Q} & \mathbf{A}^\tau \\ -\mathbf{A} & 0 \end{pmatrix} \begin{pmatrix} \mathbf{d} \\ \lambda \end{pmatrix},$$

$$\mathbf{u} \geq 0, \mathbf{v} \geq 0, \mathbf{d} \geq 0, \lambda \geq 0, \mathbf{u}^\tau \mathbf{d} = 0, \mathbf{v}^\tau \lambda = 0. \quad (11)$$

Thus, the minimization problem in (6) represents a LCP. In a compact form, the LCP for the problem in (6) can be written as [1]:

$$\begin{aligned} \mathbf{z} - \mathbf{M}\mathbf{w} &= \mathbf{q}, \\ \mathbf{z} &\geq 0, \quad \mathbf{w} \geq 0, \quad \mathbf{z}^\tau \mathbf{w} = 0, \end{aligned} \quad (12)$$

where $\mathbf{M} = \begin{bmatrix} \mathbf{Q} & \mathbf{A}^\tau \\ -\mathbf{A} & 0 \end{bmatrix}$, $\mathbf{z} = \begin{bmatrix} \mathbf{u} \\ \mathbf{v} \end{bmatrix}$, $\mathbf{w} = \begin{bmatrix} \mathbf{d} \\ \lambda \end{bmatrix}$ and $\mathbf{q} = \begin{bmatrix} -\mathbf{R} \\ \mathbf{b} \end{bmatrix}$. If \mathbf{Q} is semi positive definite then \mathbf{M} is also a semi positive semi-definite matrix [1] [11].

LCP Solver:

There are two main families of algorithms are available to solve for the LCP(q,M) (12): *a)* direct algorithms and *b)* indirect algorithms. In this research, the most robust and direct Lemke's algorithm [1] [9] [11] is used to solve LCP (12).

A. Design Examples

In this section, a set of design examples are provided. The objective here is to show various FIR filter designs via LCP with and without weights compared with optimal least square method. Figure 1 shows the design of 79th-order linear phase lowpass FIR filter. The tolerance scheme for the passband $[0, 0.4\pi]$ and stopband $[0.45\pi, \pi]$ is 0.02 [1].

Another example of the 87th-order linear phase bandpass FIR filter design is shown in Figure 2. Tolerance schemes for the passband $[0.35\pi, 0.65\pi]$ and stopband $[0, 0.3\pi]$, $[0.7\pi, \pi]$ are 0.04 and 0.06 respectively [1].

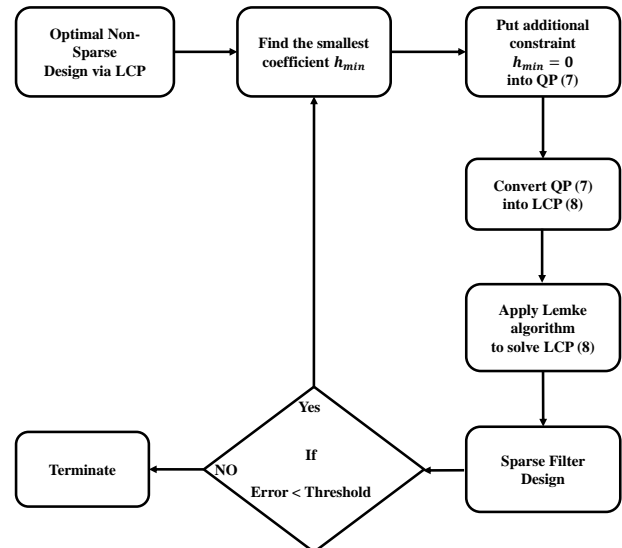


Figure 3. LCP based successive thinning algorithm to design sparse FIR digital filter.

Design examples show that with the appropriate weighting strategy LCP method [1] can lead to FIR filters with equiripple response.

III. SPARSE FILTER DESIGN USING LCP

Since in many applications, the number of arithmetic operations indicate the cost of implementation, thus reducing the length of impulse response that is designing sparse filters is beneficial not only in term of computational cost but also in hardware and energy consumption [13] [14]. To test the performance of LCP in context of spares filter designing, we proposed a simple algorithm shown in Figure 3 that iteratively thins the impulse response of

TABLE I. PERFORMANCE OF LCP IN THE CONTEXT OF SPARSE AND NON-SPARSE FILTER DESIGN

No. of coefficients	Non-zero weights	zero weights	Max.pass-band error [dB]	Min.stop-band attenuation [dB]
79	79	0	0.0852	-40.2
79	61	18	0.1148	-37.57
61	61	0	0.1956	-32.89

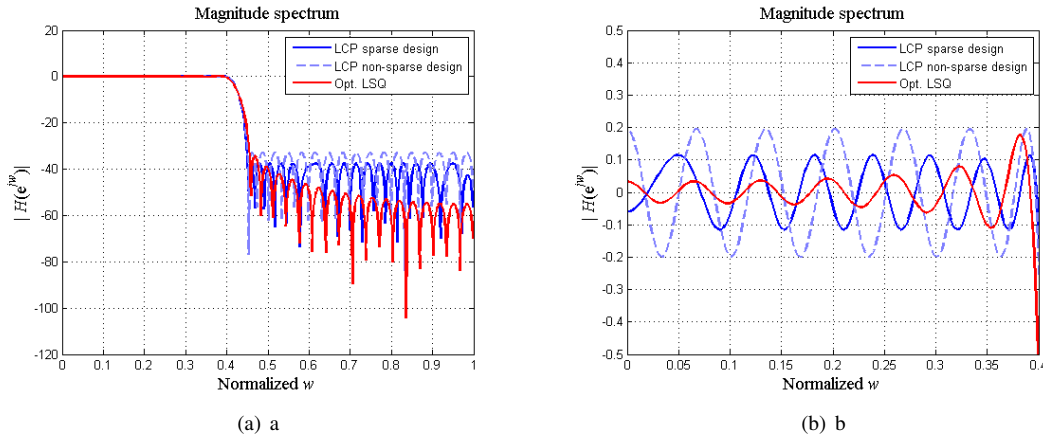


Figure 4. Performance comparison of sparse and non-sparse filters with 61 non-zero co-coefficients. This can be observed that sparse FIR filter designed by LCP offer advantage, when compared to its equivalent non-sparse filter designed by LCP and optimal least square method.

a non-sparse filter. For successive thinning of the impulse response, usually we start with higher no. of coefficients than required [13] [14].

Application of Successive thinning algorithm:

The successive thinning algorithm shown in Figure 3 is applied on the 79th order non-sparse filter shown in Figure 4 with passband $[0, 0.4\pi]$ and stop-band $[0.45\pi, \pi]$. Figure 4 and Table I compare the sparse and non-sparse FIR filters designed by LCP approach.

IV. DISCUSSION RESULTS

In [1], the author used quadratic measure to design digital filters via LCP without weights and tried to minimize the effect of Gibb's phenomenon by ignoring the transition band and simply removing it from the error measure. Thus, the presented examples show that a compromise has to be made at one of the band edges. However, the FIR examples presented in sections II and III showed the efficiency of the proposed weighting strategy.

Moreover, it has been observed that, the LCP-solvers like Lemke's algorithm are very sensitive to the frequency grid. Different passband to stopband frequency grid (p/s-fg) ratio can lead to different solutions. The denser the frequency grid in passband compared to the stop-band, the smaller the error in passband but at a cost of increased error in stopband and vice versa. To show the effect of frequency grid ratio, a 95th order FIR filter with passband

$[0, 0.11\pi]$ and stopband $[0.15\pi, \pi]$ designed by LCP is shown in Figure 5.

V. CONCLUSION AND FUTURE WORK

In this paper, the problem of linear phase FIR filter design is reconsidered as a LCP with a weighting strategy. The LCP is not an optimization technique because there is no objective function to optimize; thus, the design problem of the linear phase 1D FIR filter is formulated via quadratic programming, and then the equivalent semidefinite LCP form is obtained by applying the Karush Kuhn Tucker conditions. One advantage of LCP is its well-developed theory because there are a number of algorithms available to solve a particular LCP. In the case of an FIR filter, the resulted semidefinite LCP is solved by the most robust Lemkes algorithm. It is shown with simulations that with a proper weighting strategy LCP can lead to equiripple solution for 1D FIR filters. In addition, a simple but effective algorithm is presented to design sparse FIR filters. Sparse filters designed by the proposed successive thinning algorithm outperform the non-sparse filters with equal number of non-zero coefficients.

Future work is in progress to extend the LCP technique in order to design two dimensional FIR filter.

REFERENCES

- [1] A. M. Al-Fahed Nuseirat, "Design of linear phase FIR filters via linear complementarity problem (LCP) approach," Interna-

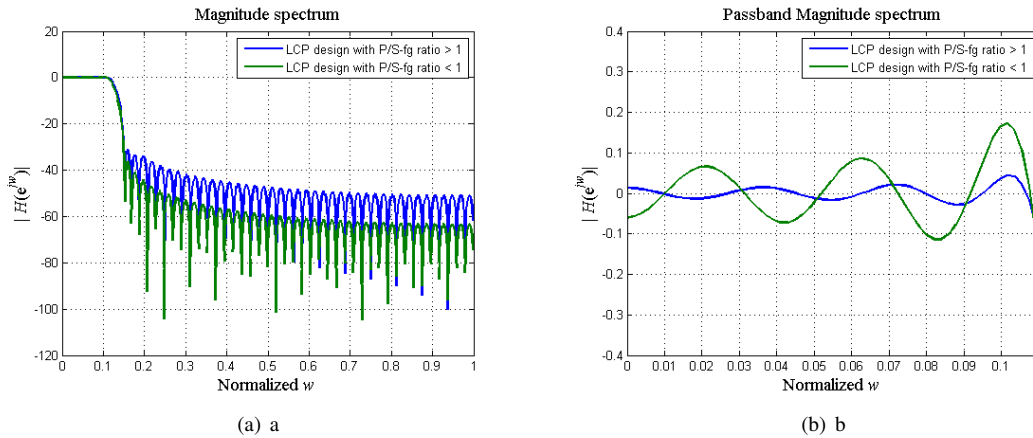


Figure 5. Performance of LCP designed FIR filters without weights. Effect of passband to stopband frequency grid (p/s-fg) ratio can be observed on Magnitude spectrum.

- tional Journal of Circuit Theory and Applications Sept. 2005, vol. 33, no. 5, pp. 353-364.
- [2] L. R. Rabiner, "The design of finite impulse response digital filters using linear programming techniques," Bell System Technical Journal Aug. 1972, vol. 51, no.6, pp. 1117-1198.
 - [3] P. P. Vaidyanathan and T. Q. Nguyen, "Eigenfilters: a new approach to least-square FIR filter design and applications including Nyquist filters," IEEE Transactions on Circuits and Systems, Jan. 1987, vol. 34, no. 1, pp. 11-23.
 - [4] G. W. Medlin, J. W. Adams, and C.T. Leondes, "Lagrange multiplier approach to the design of FIR filters for multirate applications," IEEE Transactions on Circuits and Systems, Aug. 2002, vol. 35, no.10, pp. 1210-1219.
 - [5] M. H. Er and C. K. Siew, "Design of FIR filters using quadratic programming approach," IEEE Transactions on Circuits and Systems II Aug. 2002, vol. 42, no. 3, pp. 217-220.
 - [6] T. W. Parks and J. H. McClellan, "Chebyshev approximation for nonrecursive digital filters with linear phase," IEEE Trans.Circuit Theory, Mar. 1972, vol. 19, pp. 189-194.
 - [7] V. R. Algazi, M. Suk, and R. Chong-Suck, "Design of almost minimax FIR filters in one and two dimensions by WLS technique," IEEE Transactions on Circuits and Systems Jan. 2003, vol. 33, no. 6, pp. 590-596.
 - [8] M. Lang, I. W. Selesnick, and C. S. Burrus, "Constrained least squares design of 2-D FIR filters," IEEE Transactions on Signal Processing, May 1996, vol. 44, no. 5, pp. 1234-1241.
 - [9] K. G. Murty, Linear Complementarity: Linear and Nonlinear Programming, 1997.
 - [10] A. Chandra and S. Chattopadhyay, "Design optimization of powers-of-two FIR filter using self-organizing random immigrants GA," International Journal of Electronics, 2015, vol. 102, no. 1, pp. 127-140.
 - [11] O. L. Mangasarian and J. S. Pang, "The Linear Complementarity Problem," SIAM Journal on Matrix Analysis and Applications, 1995, Vol. 16, no. 2, pp. 359-368.
 - [12] A. Fischer, "A Newton-Type Method for Positive-Semidefinite Linear Complementarity Problems," Journal of optimization theory and applications, September 1995, vol. 86, no. 3, pp. 585-608.
 - [13] T. Baran, D. Wei, and A. V. Oppenheim, "Linear Programming Algorithms for Sparse Filter Design," IEEE Transaction on signal processing, March 2010, no. 3, vol. 58, pp. 1605-1617.
 - [14] D. Wei, C. K. Sestok, and A. V. Oppenheim, "Sparse Filter Design Under a Quadratic Constraint:Low-Complexity Algorithms," IEEE Transaction on signal processing, Feb. 2013, no. 4, vol. 61, pp. 857-870.

Measurements of UWB Propagation and Transmission for Wireless Links in Spacecrafts

Miyuki Hirose and Takehiko Kobayashi

Wireless Systems Laboratory
Tokyo Denki University
Tokyo, Japan
miyuki@wsl.c.dendai.ac.jp

Abstract—This paper presents measurement and characterization of ultra wideband propagation with a view to (at least partly) replacing wired interface buses in spacecrafts with wireless links. Channel responses in the frequency- and time-domain, spatial distributions of UWB and narrowband propagation gains, delay spreads, and throughputs were measured with use of four different-sized shield boxes (simulating miniature satellites). In terms of Frequency domain, narrowband resulted in nearly 35-dB fading at several “dead spots” caused by multipath environment, UWB yielded none. However, significantly long delay spreads and thus limited link performance are caused by multipaths within a conductive enclosure. Even in such an environment, it was found that delay spreads can be suppressed by partially paneling a radio absorber and apertures (perforated on the outer surface of satellites). The results revealed that commercially-available UWB devices were capable of accommodate up to 480-Mb/s data buses within spacecrafts.

Keywords- *intra-spacecraft wireless communication; ultra-wideband; radio propagation; delay spreads.*

I. INTRODUCTION

Recently, a number of studies have been reported about wireless communications in closed and semi-closed environments [1]-[4]. We proposed wireless communication within a spacecraft for replacing wired interface buses with wireless links and experimentally studied ultra wideband (UWB) radio propagation in a small scientific spacecraft [5]. Narrowband wireless links within a spacecraft were numerically calculated and evaluated in [6]. However, narrowband wireless communication systems cause spatial fading in multipath environments and therefore need a substantial amount of fading margin. On the other hand, UWB signals suffer less from multipath fading, and thus provide more dependable, higher-speed links (e.g., maximum of 400 Mb/s per node attained with SpaceWire [7], equaling the standards of a wired onboard data bus).

As on-board mission equipment diversifies, the volume and weight of cable used to interconnect subsystems increase. Since data buses used in manned spacecrafts are required to be tripled, the weight becomes further significantly heavy. Moreover, spacecrafts have been assembled manually for the most part, resulting in high costs and long lead times. Particularly, harnessing, interconnecting, and testing interface buses have been becoming much more time-consuming, as spacecraft complexity increases [8]. Although wireless technologies have not been utilized within spacecrafts as a

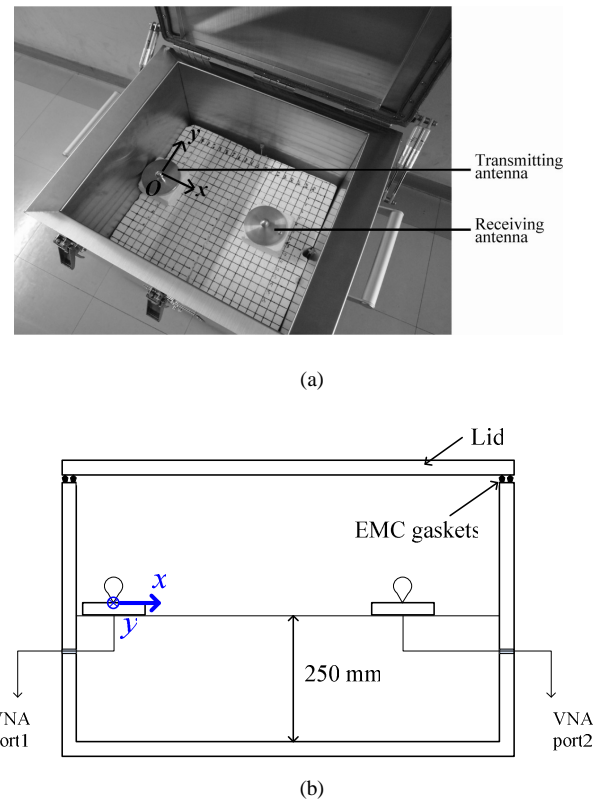


Figure 1. Measurement setup in a shield box: (a) top and (b) side views.

physical layer of data buses, applying wireless technologies to a portion of signal wires could be extremely useful. A use of wireless connections within the spacecrafts could contribute to: (i) reduction of cable weight and launching cost as a result, (ii) reduction in the cost of manufacture, and (iii) more flexibility in layout of spacecraft subsystems, and (iv) more reliable connections at rotary, moving, and sliding joints. In this study, UWB signal propagation was measured (3.1 — 10.6 GHz, the full-band UWB, 4.2 — 4.8 GHz, a part of the low-band UWB proved in Japan, and 7.4 — 7.9 GHz, a part of the high-band UWB approved in Japan) in a shield box. In Section II, our experiment setup was presented. Measurement results of propagation and transmission are described in Section III and IV respectively. Section V concludes the paper.

II. EXPERIMENT SETUP

A shield box, 430 mm long \times 470 mm wide \times 435 mm high, simulating a small scientific spacecraft “INDEX/REIMEI” (launched in 2005) was used for the measurements. Within the shield box, the transmitting antenna was fixed at 250 mm above the bottom and adjacent to the center of a 430-mm side, as shown in Fig. 1. This position was defined as the origin of the Cartesian coordinate, whose x and y axes were parallel to the sides. The receiving antenna was scanned within a region $0 \leq x$ [mm] ≤ 340 and $-140 \leq y$ [mm] ≤ 140 in 20-mm intervals on a polystyrene foam stage (virtually transparent to microwave). Since the minimum distance between the antenna electric centers was $120 \text{ mm} < \lambda_L / 2\pi$ (λ_L is the wavelength at the lowest frequency), all the measurements were carried out in a far-field region. The transmitting and receiving antennas were omnidirectional, vertically polarized, low voltage-standing-wave-ratio UWB monopole antennas [5]. Their circular ground planes were 100 mm in diameter. During the measurements, the conductive top lid was closed.

Frequency- and time-domain propagation gains were measured with a microwave vector network analyzer (VNA). Major specifications of the measurements are listed in Table I. From the frequency-domain power gain data, the UWB propagation gains were calculated by summing the power of the gains between the feeding points of the antennas over the occupied bandwidth:

$$PG_{UWB} = 10 \log \left(\frac{1}{f_H - f_L} \sum_{f_i=f_L}^{f_H} 10^{\frac{PG_{dB}(f_i)}{10}} \right), \quad (1)$$

where $PG_{dB}(f_i)$ is the propagation gain in dB measured at a frequency f_i , and f_L and f_H are the lowest and the highest frequencies; and the continuous wave (CW) propagation gains at the center frequency ($= 6.85$ GHz) were extracted therefrom. Root-mean-square (rms) delay spread was calculated from the time-domain power gain (delay profile) $P(\tau_i)$, where τ_i is the i -th path delay. The rms delay spread (S) is given by

$$S = \sqrt{\frac{\sum_i \tau_i^2 P(\tau_i)}{\sum_i P(\tau_i)} - \left(\frac{\sum_i \tau_i P(\tau_i)}{\sum_i P(\tau_i)} \right)^2}, \quad (2)$$

where the summations are taken above a threshold level -20 dB below the maximum of $P(\tau_i)$.

A commercially-available device of WiMedia [9] was used in the experiments to facilitate a high data rate and to reduce the fading margin. Its major specifications are listed in Table II. The WiMedia, a high-speed wireless personal area communication standard, utilizes a multiband-OFDM. In OFDM, the input data are divided into blocks of the same size, where each block is referred to as an OFDM symbol. By appending a cyclic prefix to each OFDM symbol, intersymbol interference can be removed as long as the prefix is longer than the impulse response of the channel (typically represented by the delay spread). The multiband-OFDM employs a 60.61-ns zero postfix. When the delay spreads are sufficiently shorter than 60.61 ns, therefore, the WiMedia devices can be used,

TABLE I. SPECIFICATIONS OF THE MICROWAVE VECTOR NETWORK ANALYZER.

Model	Agilent E8362B		
Bandwidth	3.1-10.6 GHz (full-band)	4.2 - 4.8 GHz (low-band)	7.4 - 7.9 GHz (high-band)
Frequency sweeping points by VNA	7501	601	501
Calibration	Internal function of the VNA		

TABLE II. PARAMETERS OF A WiMEDIA DEVICE UNDER TEST.

Nominal maximum bit rate	72 Mbps
Modulation	QPSK-OFDM
Frequency	4.2 - 4.8 GHz (low-band) 7.3 - 7.9 GHz (high-band)
Duration of cyclic prefix	60.61 ns

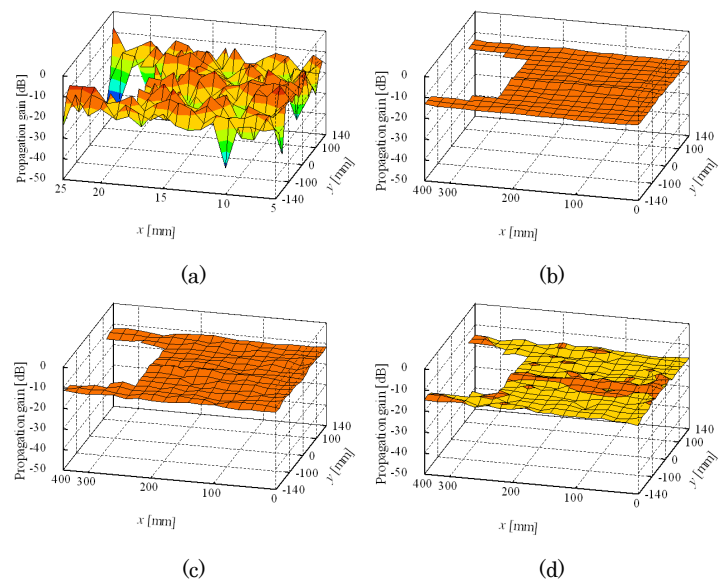


Figure 2. Spatial distribution of propagation gain within the shield box: (a) CW and (b) full-, (c) low-, and (d) high-band UWB.

which yield the maximum data rate of 480 Mbps, within the spacecrafts. Nonetheless, nominal bit rate of the device under test in this paper was 72 Mbps according to specifications.

III. PROPAGATION RESULTS

The spatial distributions of continuous wave (CW) and UWB propagation gains within the shield box are shown in Fig. 2. Since the shield box didn't have a precise symmetry, the propagation gain of CW was asymmetric. Propagation gains ranged $-41 - 6.1$ dB for CW, $-15 - -12$ dB for the full-, $-14 - -9.7$ dB for the low-, and $-19 - -13$ dB for the high-band UWB. While CW resulted in up to 35 dB fading at several “dead spots” caused by multipath interference, propagation gain variations were 4.7, and 4 dB for full-, low-, and high-band UWB. Spatial distribution of delay spreads for full-band UWB is depicted in Fig. 3. The delay spreads ranged from 43.7

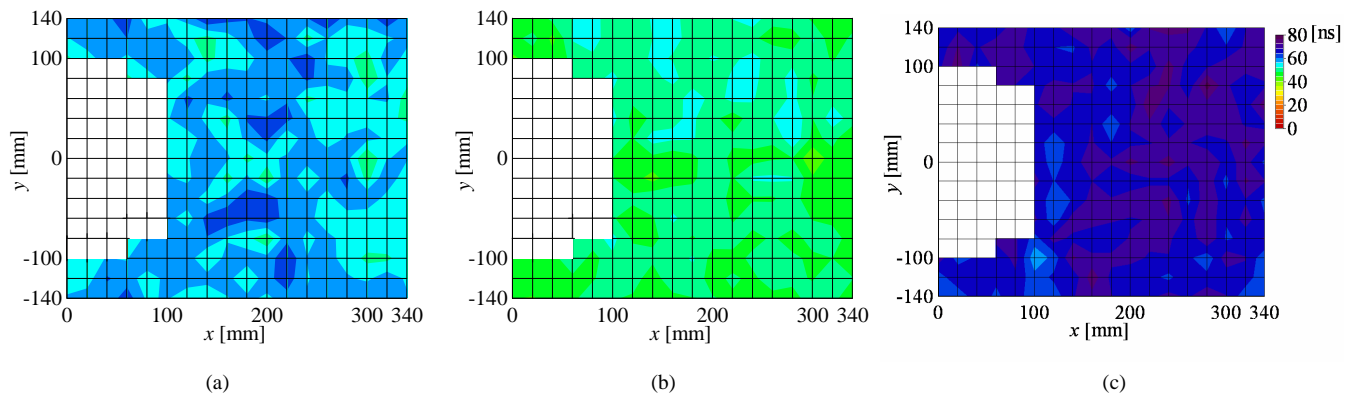


Figure 3. Spatial distribution of delay spreads for: (a) full- (3.1 - 10.6 GHz), (b) low- (4.2 - 4.8 GHz), and (c) high-band UWB (7.4 - 7.9 GHz).

TABLE III. DIMENSION OF THE INNER VOLUME USED FOR EXPERIMENTS.

	Width [mm]	Depth [mm]	Height [mm]	Volume [m ³]
V	470	430	435	8.8×10^{-2}
$V/2$			218	4.4×10^{-2}
$V/4$			108	2.2×10^{-2}
$V/8$			54	1.1×10^{-2}

to 64.3 ns. The conductive enclosures yields a long delay spread which causes inter-symbol interference, and hence an irreducible error floor when the modulation symbol time is of the same order as the delay spread.

A. Effects of Volume

The inner volume (V) of the box was varied between 1.1, 2.2, 4.4, and $8.8 \times 10^{-3} \text{ m}^3$, as listed in Table III, with use of polystyrene-foam parallelepipeds, covered with aluminium foil and fitted to the bottom of the box. The height of the transmitting and receiving antennas was approximately a half of the box height. Examples of frequency-domain propagation gains are presented measured at $(x, y) = (300, 0)$ with a volume of $1.1 \times 10^{-2} \text{ m}^3$ and $8.8 \times 10^{-2} \text{ m}^3$, in Fig. 4. The frequency- and time-domain gains increase with the inner volume [10]. At a given delay time, a multipath component arrives at the receiving antenna after a different number of reflections on the walls for different-sized boxes, while the traveling time is the same, and hence the total free space propagation loss is the same. The number of reflections increases with decreasing the inner volume, since a mean free path length between reflections is approximately proportional to $V^{1/3}$. Since total reflection losses on the conductive (but not perfectly conductive) walls are roughly proportional to the number of reflections, the propagation gain at a given delay time decreases with increasing inner volume.

The delay spreads were found at more than 85 ns for $V = 8.8 \times 10^{-3} \text{ m}^3$, while 5 ns for $V = 1.1 \times 10^{-3} \text{ m}^3$. Delay spreads against the inner volume are plotted in Fig. 5 for full-, low-, and high-band UWB. In all cases, the delay spreads increased with the inner volume. Delay profiles at $(300, 0)$ were calculated by the FDTD method and the delay spreads were derived therefrom, when the height was varied between 435, 218, 108, and 54 mm, while the bottom area was fixed at $430 \text{ mm} \times 470 \text{ mm}$. The heights of the antennas were half of the

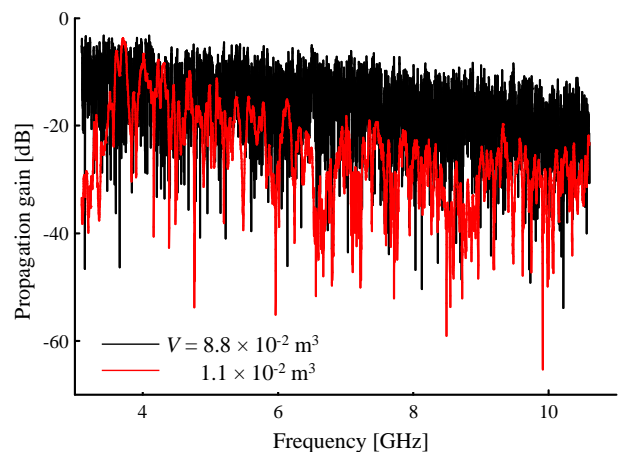
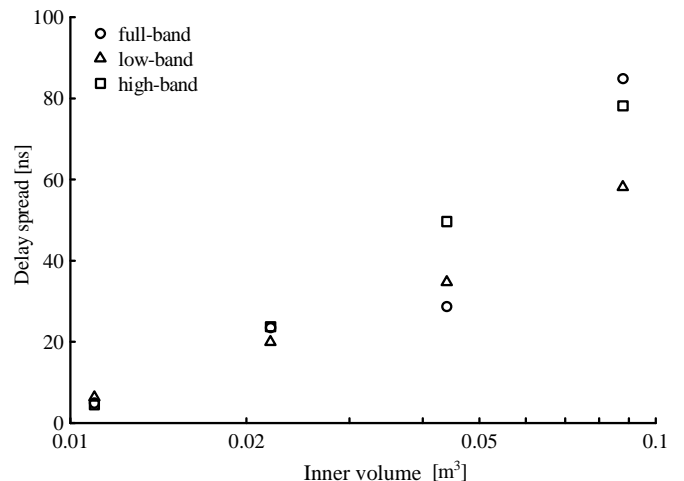

 Figure 4. Examples of frequency response measured in the shield boxes ($V = 8.8$ and $1.1 \times 10^{-2} \text{ m}^3$).


Figure 5. Delay spreads against the inner volume.

inner height of the box. In both cases of simulation and measurement, the delay spreads increased with the inner volume, as shown in Fig. 6. The measurement result is indicated by a circle in Fig. 6. The difference between the simulation and the measurement may be attributed to the electromagnetic energy leakage of the shield box (shielding

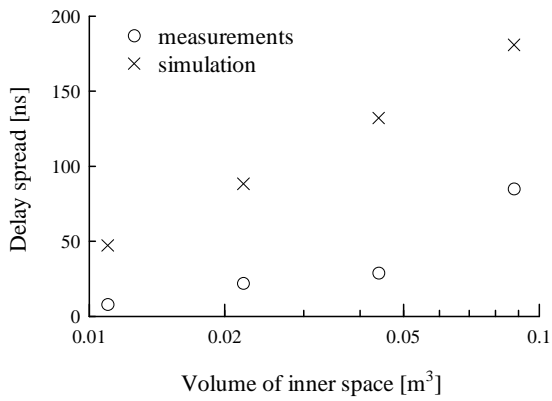


Figure 6. Delay spreads against the inner volume of shield boxes.

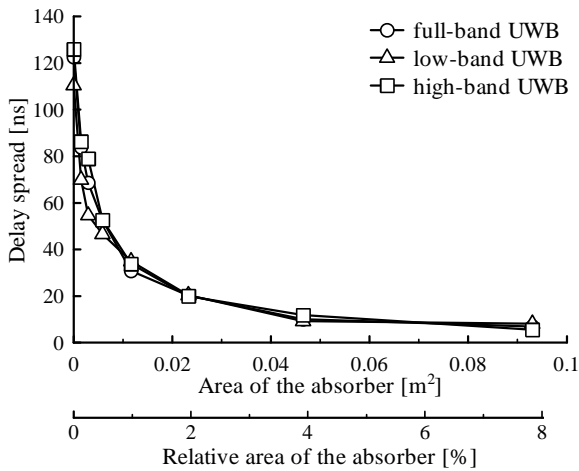


Figure 7. Delay spreads versus area of the absorber.

effectiveness was approximately 60 dB), while the perfect shielding was assumed in the simulation. The longer delay paths were attributed to the heavy multipaths within the conductive closed space.

B. Effects of Radio Absorber

A patch of a thin elastic radio absorber was attached at the center of the bottom of the shield box to suppress the delay spreads [5]. The absorbers, 2.3 and 1.8 mm thick, usable in vacuum, attenuated radio wave reflection by 20 dB at 4 and 7 GHz, respectively, and by 10 dB within a 1.5-GHz bandwidth. The absorber of 2.3-mm thickness was used for low-band UWB experiments, and that of 1.8 mm for full- and high-band. Propagation properties were measured while the patch of the strip was $0.093 \text{ m}^2 (= 305 \text{ mm square}) \times 2^{-n}$, where $n = 0, 1, 2, \dots, 6$, corresponding $8 \times 2^{-n} \%$ against the total inner surface.

The radio absorber panel can suppress the long delay spreads, as shown in Fig. 7. Received energy losses caused by the radio absorber were estimated: the absorbers of 0.003 m^2 (0.6% against the total inner surface area) and 0.013 m^2 area (4% against the total inner surface area) resulted in 2 and 5 dB

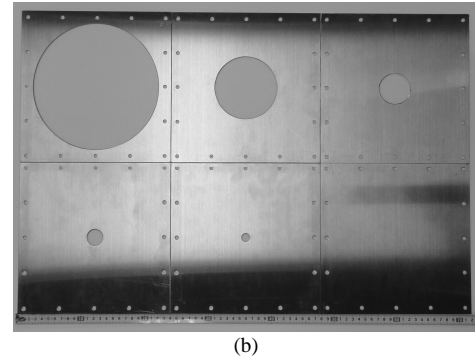
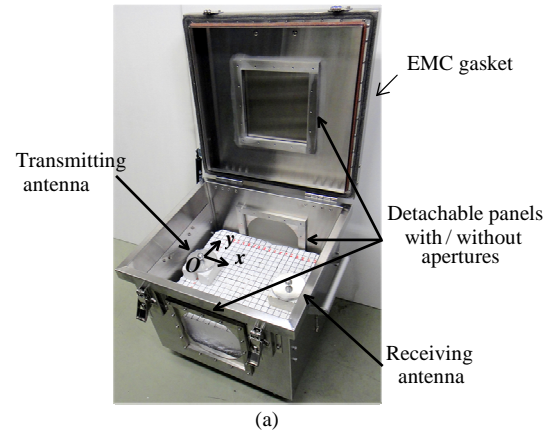


Figure 8. The measurement setup: (a) a shield box had three square holes and (b) panels (240 mm × 240 mm) with and without circular holes.

in energy loss, respectively. Including these energy losses, the relation between the fading depth and the occupied bandwidth was derived, similarly to the case of no absorber. While the absorber panel was placed in the center of the bottom of the box in this experiment, Sasaki *et al.* reported that radio reverberation characteristics were almost independent of the position of a small piece of absorber lining within a shielding chamber [11].

C. Effect of Apertures on the Surface

The effect of aperture size on UWB propagation was evaluated inside the shield box. The box (the same size of the shield box) had three $200 \text{ mm} \times 200 \text{ mm}$ square holes: one in the center of the top lid and the others in the center of both side surfaces, as shown in Fig. 8. For changing total area of apertures, conductive $240 \text{ mm} \times 240 \text{ mm}$ square panels with or without circular apertures were attached on the holes with use of conductive gaskets between mating surfaces. The diameter of the circular apertures was 12.5, 25, 50, 100, or 200 mm.

The UWB propagation gains were almost invariable for the total area of apertures normalized by the total area of the inner surface between 0.01 and 0.1% , and gradually decreased with the area beyond 10^{-3} m^2 or 0.1% , as shown in Fig. 9. The lower UWB propagation gains in the high-band UWB were ascribable to longer free space propagation losses. The delay spreads were gradually decreased with the total area of apertures, as shown in Fig. 10. The propagation gain, the delay

profiles, and the delay spreads were found statistically unvaried between the regions near and far from the apertures [12].

IV. TRANSMISSION PERFORMANCE

A commercially-available device of WiMedia [8] was used to measure link throughputs. The link throughputs were measured with use of a pair of WiMedia devices, one of which was links to a solid state drive (SSD) via USB 2.0 interface, and the other was connected to a personal computer with a built-in SSD via a PCMCIA interface. Since the throughputs fluctuated typically ± 4 Mb/s per trial, a number of trials (normally 35) were carried out to reduce the variation within ± 1 Mb/s.

Throughputs against the inner volume are plotted in Fig. 11 for full-, low-, and high-band UWB. The throughputs decreased with increasing the inner volume, which was attributable to wider delay spreads. The throughput for low- and high-band UWB was up to 96 and 100 Mb/s, when the absorber panel covered 4 and 8% of the total inner surface area, respectively, as shown in Fig. 12. With apertures, the throughputs were almost invariable for the normalized area of apertures between 0.05 and 0.4%, and gradually increased with the area beyond 0.4%, as shown in Fig. 13. When the delay spreads are suppressed sufficiently shorter than the symbol duration, we can use the WiMedia devices, which yield the maximum data rate of 480 Mb/s, within the spacecrafts.

V. CONCLUSIONS

Ultra wideband (from 3.1 — 10.6 GHz, 4.2 — 4.8 GHz, and 7.4 — 7.9 GHz) and CW (6.85 GHz) propagation and transmission were measured and characterized inside a shield box emulating a small spacecraft. While CW resulted in nearly 35-dB fading at several “dead spots” caused by multipath environment, UWB yielded none. The UWB systems have therefore an advantage over narrowband from the viewpoint of reducing fading margins. No dependence on the distance was observed for UWB propagation gain, delay spread, or throughput, and no apparent spatial correlation between them.

The conductive enclosures caused abundant multipaths and long delay spreads. The delay spreads can be suppressed with the use of a small patch of radio absorber and/or with apertures. Propagation gain decreased and the fluctuation range of the gain increased when increasing the area of radio absorber attached on an inner surface. On the other hand, propagation gains were almost invariable for the total area of apertures normalized by the total area of the inner surface between 0.01 and 0.1%, and gradually decreased with the area beyond 0.1%. The higher UWB propagation gains in the high-band UWB were ascribable to higher free space propagation losses. For empty enclosures, an 4% area of radio absorber can suppress the delay spreads less than 10 ns. With 0.1% area of apertures, the delay spreads were found at less than 11 ns. The off-the-shelf WiMedia devices can be used to accommodate up to 480-Mb/s data buses within spacecraft, as long as the delay spread is suppressed far below 60 ns, from the viewpoint of propagation.

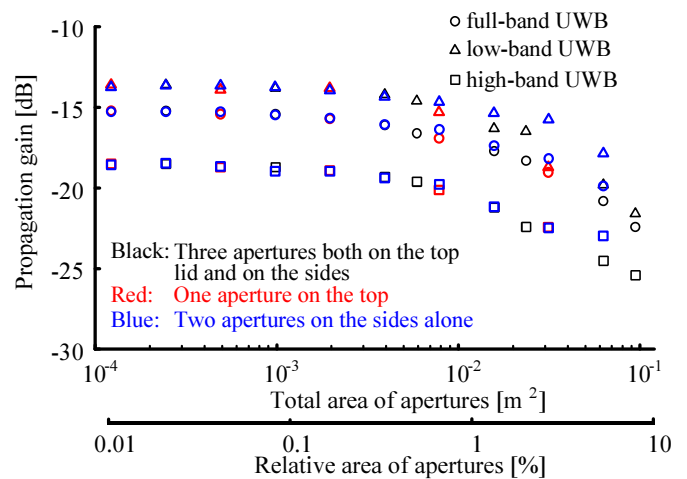


Figure 9. UWB Propagation gains versus total area of apertures.

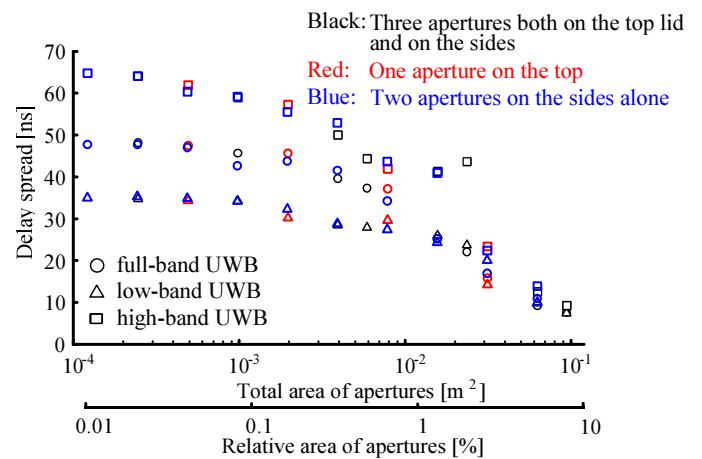


Figure 10. Delay spreads versus total area of apertures.

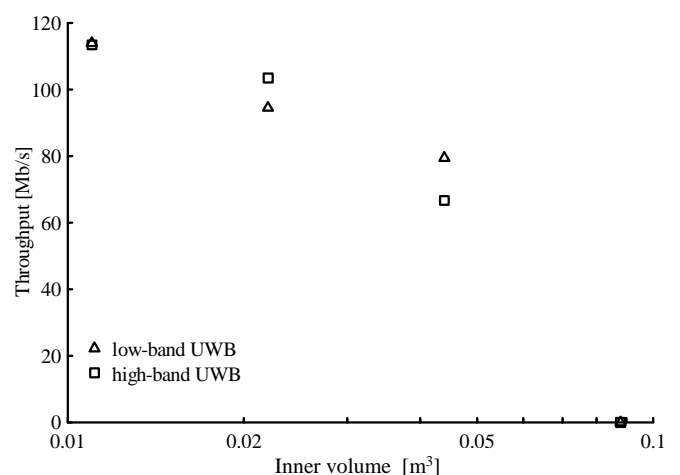


Figure 11. Throughputs against the inner volume.

ACKNOWLEDGMENT

This work was supported by JSPS KAKENHI Grant Number 15J11299.

REFERENCES

- [1] T. Kobayashi, "Measurements and characterization of ultra wideband propagation channels in a passenger-car compartment," *IEICE Trans. Fundamentals*, vol. E89-A, no. 11, pp. 3089-3094, 2006.
- [2] M. Ohira, T. Umaba, S. Kitazawa, H. Ban, and M. Ueba, "Experimental characterization of microwave radio propagation in ICT equipment for wireless harness communications," *IEEE trans. Antennas Propag.*, vol. 59, pp. 4757-4765, Dec. 2011.
- [3] J. Gelabert, A. Kavatzikidis, D. J. Edwards, and C. J. Stevens, "Experimental UWB channel characterisation of an electromagnetically small environment," in *Proc. 2009 Loughborough Antennas and Propagat. Conf. (LAPC 2009)*, pp. 381-384, UK, Nov. 2009.
- [4] Z. Li, A. Junshe, X. Yifang, and X. Weiming, "A protocol designed for intra-spacecraft impulse radio ultra-wideband communications," in *Proc. IEEE Intl. Conf. Wireless for Space and Extreme Environments (WiSEE2014)*, Netherlands, Oct. 2014.
- [5] A. Matsubara, A. Tomiki, T. Toda, and T. Kobayashi, "Measurements and characterization of ultra wideband propagation within spacecrafts—proposal of wireless transmission for replacing wired interface buses," in *Advances in Spacecraft Technologies*, pp. 61-74, IN-TECH, 978-953-307-551-8, Vienna, Austria, Feb. 2011.
- [6] P-N. Gineste, Y. Herlem, A. Outay, and P. Pelissou, "Assessment of wireless link budget in a satellite by modelling techniques," in *2012 ESA Workshop on Aerospace EMC*, pp. 1-6, Venice, Italy, May 2012.
- [7] European Cooperation for Space Standardization, Standard ECSS-E-ST-50-12C, "SpaceWire – links, nodes, routers and networks, July 2008.
- [8] R. Amini, G. Aalbers, R. Hamann *et al.*, "New generations of spacecraft data handling systems: less harness, more reliability," in *57th Intl. Astronautical Congress (AIAA 2006-448)*, Oct. 2006.
- [9] G. Heidari, *WiMedia UWB – Technology of Choice for Wireless USB and Bluetooth*, New York, John Wiley & Sons, 2008.
- [10] M. Hirose and T. Kobayashi, "Effects of inner volume on UWB propagation channels within closed spaces," in *Intl. Conf. on Ultra-Wideband (ICUWB 2014)*, pp. 1-6, France, Aug. 2014.
- [11] K. Sasaki, I. Oshima, and Y. Karasawa, "A reverberation chamber to realize multipath-rich environment [II]: Environment control by electromagnetic wave absorbing sheet," in *IEICE Technical Report A-P2008-9*, pp. 13-18, Sep. 2008 (in Japanese).
- [12] S. Hamada, A. Tomiki, T. Toda, and T. Kobayashi, "Wireless connections within spacecrafts to replace wired interface buses," *IEICE Trans. Fundamentals*, vol. E96-A, no. 5, May 2013.

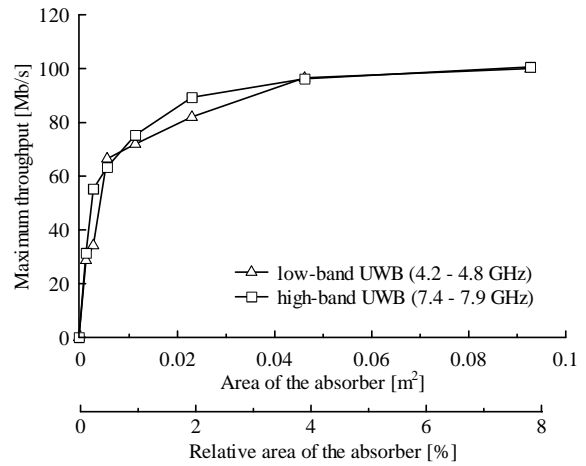


Figure 12. Throughputs measured at (300, 0) versus total area of apertures.

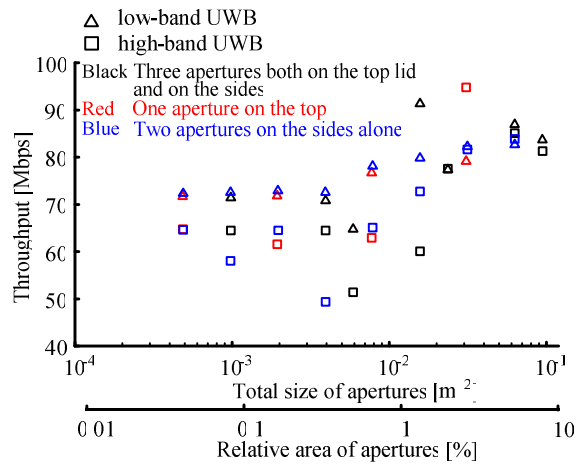


Figure 13. Throughputs measured at (300, 0) versus total area of apertures.

Mode Selection Algorithm for Advanced TOA Trilateration Techniques

Sajina Pradhan

Dept. of Advanced Parts and Materials Engineering
Chosun University
Gwangju, Republic of Korea
sajinapra@hotmail.com

Suk-seung Hwang

Dept. of Electronic Engineering
Chosun University
Gwangju, Republic of Korea
hwangss@chosun.ac.kr (corresponding author)

Abstract—The location detection technology (LDT) with various applications is one of the core techniques for the mobile communication system. The time-of-arrival (TOA) trilateration, which is a representative approach of network-based LDTs, estimates the location of a mobile station (MS) using an intersection point of three circles based on signals from at least three base stations (BS). Since the distance between MS and BS is generally estimated by the number of delay samples and it is an integer number, the radius of circles is usually increased and three circles may not meet at a point, which results in the serious estimation error. In order to overcome this problem, the shortest distance and the line intersection algorithms for the general case and the comparison approach of intersection distances for the specific case have been recently proposed. In this paper, we provide the selection methodology between these two cases for using the line intersection algorithm or the comparison approach of intersection distances, for the MS location estimation. The selection procedure for both cases is based on comparing the radiuses of two large circles to distances between four intersection points of a small circle with others and center coordinates of corresponding large circles.

Keywords—location detection; time-of-arrival; trilateration; mode selection; three circles intersection.

I. INTRODUCTION

Recently, the location estimation of MS has received a great attention, because a lot of information related to the MS location is being utilized in many communication services such as location based services (LBS). More and more researches focus on estimating the accurate MS location with the low cost, the high performance, and the reliability of the components. In USA, the MS location estimation should follow the requirement of locating emergency 911 (E-911) services [1]. LBSs involve the ability to find the geographical location of MS and provide services based on its location. The main objective of these services is to assist with the exact information in real time at the right place likes finding patient, children, elder person, transportation services, location of food court, and necessary things [2]-[6].

For estimating the location of MS, several techniques are commonly utilized based on the received signal strength (RSS), TOA, angle of arrival (AOA), and time difference of arrival (TDOA) [7][8]. The TOA trilateration method, which is one of representative location estimation approaches, estimates the MS location using the intersection point of

three circles with their centers corresponding BS coordinates and radiuses corresponding the distances between MS and BSs. However, since we generally estimate the distance between MS and BS counting the number of delay samples, which is an integer, the estimated distance may be slightly increased and three circles based on the radiuses corresponding to the estimated distance may not intersect at a single point. Therefore, three circles have total six intersection points causing estimation error for the accurate location of MS. In order to solve this problem, recently, the shortest distance algorithm [9] and the line intersection algorithm [10] have been proposed for the general case. In general, the line intersection algorithm has better performance than the shortest algorithm, because it considers the increasing factor of the estimated circles. However, its estimation performance may be degraded for the specific case, in which a small circle is located inside the area of two large circles and it intersects two large circles at four intersection points. In order to improve this problem, the comparison approach of intersection distances for the specific case has been proposed in [11]. It calculates four distances between two neighbor intersections among four intersection points of a small circle and two large circles, and compares them. From the compared result, we select the shortest distance and determine the averaged coordinate of two intersection points corresponding to the shortest distance as the estimated location of MS.

Although this approach has better performance than the line intersection algorithm for the general case, it has worse performance than the line intersection algorithm for the above specific case. Thus, we should select better algorithm according to both cases for the optimized performance. In this paper, we propose a mode selection algorithm for using the line intersection algorithm or the comparison approach of intersection distances, according to two cases of the general case or the specific case. In order to select the proper mode between both approaches, the proposed algorithm considers four intersection points related to a small circle and other two large circles. Note that we consider three circles with a small circle and two large circles in the specific case. For the proposed method, we calculate the distance between one of four intersection points and the center of the circle which is not related to the corresponding intersection. We repeat the previous calculation for all four intersections and get four distances from the calculated results. Finally, this algorithm compares each distance to the radius of the circle related to

the center used to calculating its distance. If all four distances are shorter than the corresponding radiuses, we determine that it is the specific case and select the comparison approach of intersection distances for the advanced TOA trilateration technique. However, if at least one distance is longer than them, we determine that it is the general case and select the line intersection algorithm.

The rest of the paper is organized as follow: Section II describes TOA trilateration algorithms, i.e. the line intersection algorithm for the general case and the comparison approach of intersection distances for the specific case. Section III describes the proposed mode selection algorithm for differentiating the general case and the specific case. The performance of the proposed algorithm is discussed by computer simulation results in Section IV. Finally, the conclusion is presented in Section V.

II. ADVANCED TOA TRILATERATION ALGORITHMS

The trilateration technique estimates the location of MS using the intersection points of three circles based on radiuses corresponding to distances between MS and BSs and center corresponding to coordinates of BSs. The Euclidean distance between MS and the i th BS is given by

$$r_i = \sqrt{(x - x_i)^2 + (y - y_i)^2} \quad i = 1, 2, 3 \quad (1)$$

where (x, y) is the true coordinate of MS and (x_i, y_i) is the coordinate of the i th BS. The location of MS is determined by a unique intersection point of three circles, shown in Figure 1. The distance between MS and BS is usually estimated counting the number of time delay samples. Since that number must be an integer, it is given by

$$n_i = \text{ceil}\left(\frac{r_i}{c} \times f\right) \quad (2)$$

where n_i is the number of delay samples, "ceil" is the round up function used to make an integer value, f is the particular carrier frequency, and c is the velocity of the light. The increased distance between MS and BS due to counting the number of delay samples, ed_i , is given by

$$ed_i = \frac{n_i \times c}{f}. \quad (3)$$

Since the radius of circle may be increased by the increased distance, three circles may not meet at a single point and they have six intersection points, which results in the location estimation error shown in Figure 2. In order to solve this problem, recently, a couple of algorithms have been proposed. In this paper, we consider two advanced TOA trilateration algorithms such as the line intersection algorithm having good performance in the general case and the comparison approach of intersection distances having good performance in the specific case.

A. Line Intersection Algorithm

Three circles based on the estimated distances between MS and BSs do not intersect at a unique point, because each

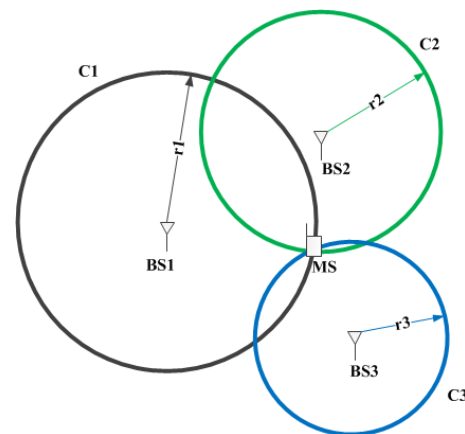


Figure 1. Three intersecting circles to locate MS at a unique point in the general case.

TABLE I. LINE INTERSECTION ALGORITHM

1. Calculate the estimated distance between each BS and MS after counting number of time delay sample, and is given by $ed_i = \frac{n_i \times c}{f}.$
2. Generate three circle equations using estimated distance $\hat{x}^2 + \hat{y}^2 + a_i \hat{x} + b_i \hat{y} + c_i = 0$ where $a_i = -2x_i, b_i = -2y_i$, and $c_i = x_i^2 + y_i^2 - ed_i^2$.
3. Obtain the estimated location of MS (\hat{x}, \hat{y}) , using $\hat{x} = \frac{(c_2 - c_1)(b_2 - b_3) - (c_3 - c_2)(b_1 - b_2)}{(a_1 - a_2)(b_2 - b_3) - (a_2 - a_3)(b_1 - b_2)},$ and $\hat{y} = \frac{(a_1 - a_2)(c_3 - c_2) - (c_2 - c_1)(a_2 - a_3)}{(a_1 - a_2)(b_2 - b_3) - (a_2 - a_3)(b_1 - b_2)}.$

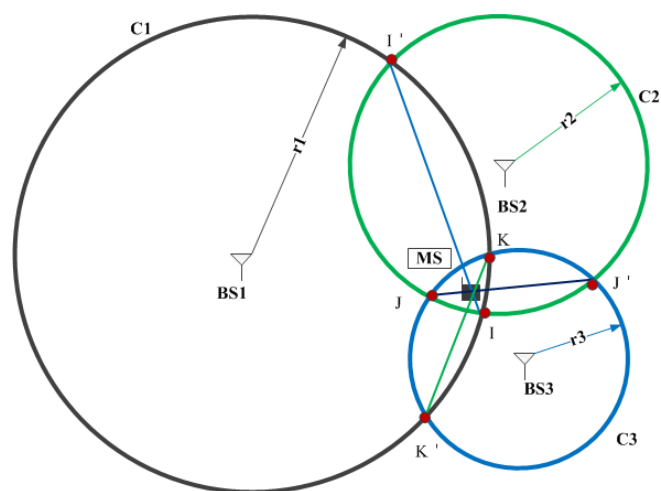


Figure 2. Line intersection at a single point to estimate MS location in the general case.

radius corresponding the estimated distance is generally increased comparing to the original radius. Based on the calculated radiuses, they meet at six intersection points. From the six relevant intersection points, we make three straight lines which connect two intersection points for specific two circles among entire three circles. These three

straight lines must meet at a point and this algorithm determines the intersection point of three lines as the location of MS as shown in Figure 2. Table I summarizes the line intersection algorithm in the general case.

B. Comparison Approach of Intersection Distances

Although the line intersection algorithm has good performance for estimating the MS location in general case, it may have the poor performance in the specific case, where a small circle is located in the area of two large circles, shown in Figure 3. In order to improve this problem, the comparison approach of intersection distances has been proposed, specialized in the specific case. This algorithm focuses on distances between two neighboring points of four interior intersections related to a small circle, among six entire intersection points, shown in Figure 4. First of all, it calculates two distances between two sets of points. They are calculated from two intersecting points of the small circle with one large circle to the neighboring intersection points of the small circle and another large circle. After calculating two distances, we compare them and select the shorter distance. Finally, this algorithm determines the averaged coordinate of two intersections corresponding to the shorter distance as the MS location.

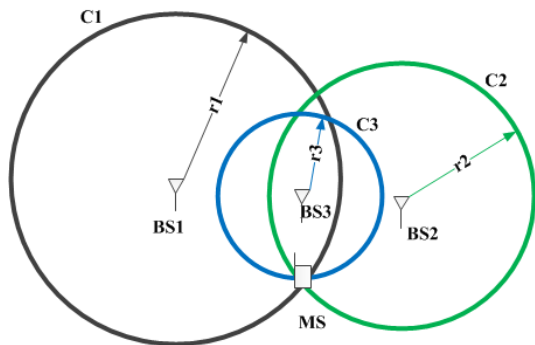


Figure 3. Three intersecting circles to locate MS at a unique point in the specific case

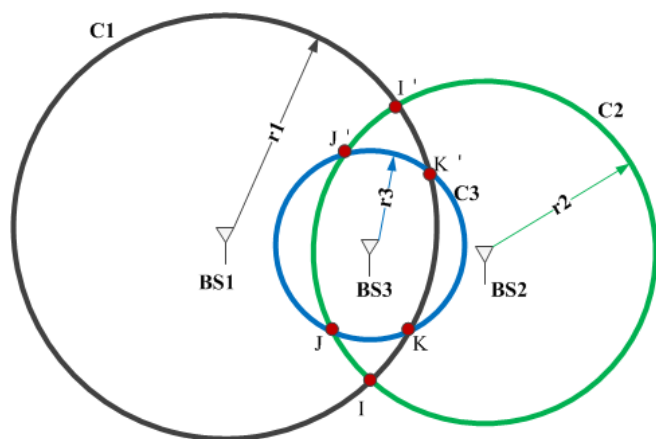


Figure 4. Three intersecting circles with the increased radius in the specific case.

TABLE II. COMPARISON APPROACH OF INTERSECTION DISTANCES

1. Initialize the circles C1, C2, and C3, based on centers of BSs and radiuses equal to estimated distances.
2. Find all six intersections coordinate points I, J, K, I', J', and K'.
3. Take two intersection points of a small circle C3 with two large circles C1 and C2 (J', K') and calculate distance between two points (distance between J' and K').
4. Repeat step 3 for other intersection points (J, K).
5. Compare two distances ((distance J'K') and (distance JK)).
6. Select the shorter distance between two distances.
7. Take two intersection points corresponding to the selected distance.
8. Calculate the averaged coordinate of two intersection points and determine it as the estimated MS location, given by $\hat{x} = \frac{J'_x + K'_x}{2}$, $\hat{y} = \frac{J'_y + K'_y}{2}$.

The detail step of comparison approach of intersection distances algorithm has been summarized in Table II.

III. MODE SELECTION ALGORITHM

The line intersection algorithm and the comparison approach of intersection distances have the good performance for estimating the MS location for the general case and the specific case, respectively. For the optimized location estimation, we should select an algorithm between both according to the case. In this section, we propose the mode selection algorithm for distinguishing the general case and the specific case. If the algorithm selects the general case, it employs the line intersection algorithm for estimating the MS location. However, if it selects the specific case, it employs the comparison approach of intersection distances.

In order to select the case mode, the proposed algorithm calculates four distances related to centers of two large circles and four intersection points of a small circle with two large circles. Each distance is calculated from the center of each large circle to the intersection of the small circle with another large circle, defined as

$$d_{lk} = \sqrt{(x_l - x_k)^2 + (y_l - y_k)^2} \quad l = 1, 2, k = 1, 2, \quad (4)$$

where (x_l, y_l) is a coordinate of the l th large circle and (x_k, y_k) is a coordinate of the intersection point of the small circle with another large circle. Next, the distances related to the l th large circle are compared to the radius of the l th large circle; d_{11} and d_{12} are compared to r_1 and d_{21} and d_{22} are compared to r_2 . If all distances related to the l th large circle are shorter than the radius of the l th large circle (d_{11} and d_{12} are shorter than r_1 and d_{21} and d_{22} are shorter than r_2), it selects the specific case mode and employs the comparison approach of intersection distances. Otherwise, it selects the general case mode and employs the line intersection algorithm.

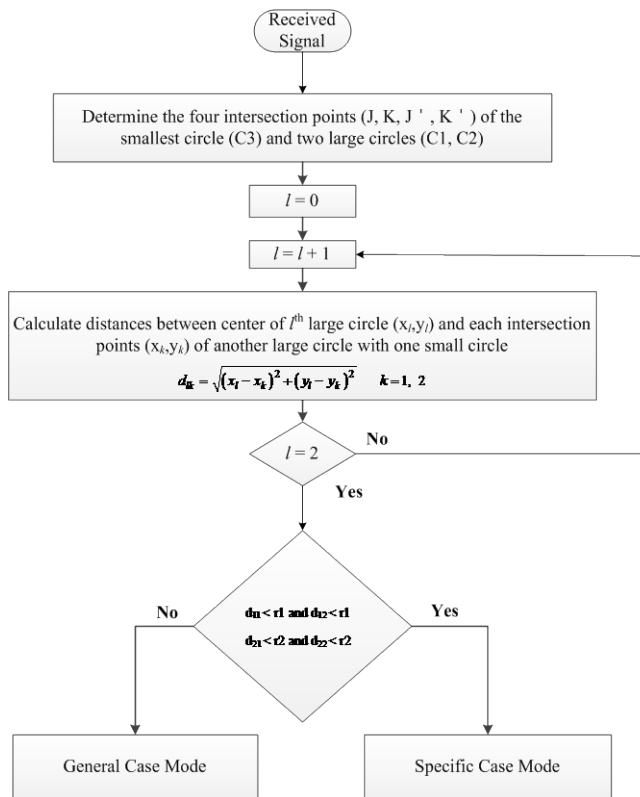


Figure 5. Flow chart for the mode selection algorithm.

TABLE III. MODE SELECTION ALGORITHM

1.	Find the two intersection points (J, J') formed by the small circle C3 intersected with the large circle C2.
2.	Calculate the distances from the center of the large circle C1 (x_1, y_1) to the two intersection points (J, J'), given by $d_{1k} = \sqrt{(x_1 - x_k)^2 + (y_1 - y_k)^2}$ $k = 1, 2$.
3.	Find the two intersection points (K, K') formed by small circle C3 intersected with the large circle C1.
4.	Calculate the distances from the center of the large circle C2 (x_2, y_2) to the two intersection points (K, K'), given by $d_{2k} = \sqrt{(x_2 - x_k)^2 + (y_2 - y_k)^2}$ $k = 1, 2$.
5.	Compare the radius of C1, r_1 , to d_{11} and d_{12} .
6.	Compare the radius of C2, r_2 , to d_{21} and d_{22} .
7.	a. $d_{11} < r_1$ and $d_{12} < r_1$, and $d_{21} < r_2$ and $d_{22} < r_2$ ☞ Specific Mode (employing comparison approach of intersection distances)
	b. Otherwise
	☞ General Mode (employing line intersection Algorithm)

Figure 5 shows a flow chart for the proposed mode selection algorithm and Table III summarizes steps of the algorithm. Using this mode selection algorithm, we may get the optimized performance for estimating the location of MS for the general case and the specific case.

IV. COMPUTER SIMULATIONS

In this section, we provide computer simulation results to illustrate the location estimation performance for the proposed approach. For the simulation, we consider three fixed BSs and two cases for coordinates of BSs and MS for distinguishing the general case and the specific case:

1. General case: three BSs with coordinates of (-1000, 5000), (6000, -3000), and (-7000, 600).

2. Specific case: three BSs with coordinates of (-3000, 5000), (1500, 3000), and (7000, 600).

The unit of the coordinate is meter (m) and we consider the different carrier frequencies of 50MHz, 100MHz, 500MHz, 1GHz, 5GHz, and 10GHz. Also, we consider two scenarios for the occurrence possibility of the general case and the specific case:

1. First scenario: 90% general case and 10% specific case.

2. Second scenario: 95% general case and 5% specific case.

case.

We assume that the MS location coordinate is randomly chosen with ranges from -100 to 100 and from -500 to 500 for the first case and the second case, respectively.

The performances of the location estimation algorithm are evaluated by the mean square error (MSE). The error between the true MS position and the estimated MS position is defined as

$$Error_{Position} = \sqrt{(x - \hat{x})^2 + (y - \hat{y})^2} \quad (5)$$

and MSE for estimating the MS position is given by

$$MSE_{Position} = E[Error_{Position}^2]. \quad (6)$$

The simulation results of the MSE for the MS location estimation verses frequencies for the first scenario are shown in Figures 6 and 7, for the first and second cases, respectively. In addition, the simulation results of the MSE for the MS location estimation verses frequencies in the second scenario are shown in Figures 8 and 9, for the first and second cases, respectively. From figures, we observe that the MSE of the advanced TOA trilateration based on the mode selection algorithm is lower than the MSE of that based on only the line intersection algorithm. Note that the difference between two curves for the first scenario is larger than the difference for the second scenario, because the occurrence possibility of the specific case in the first scenario is higher than it in the second scenario.

V. CONCLUSION

The line intersection algorithm has good location estimation performance for the general case, but it may have the serious location estimation error for the specific case, where a small circle is located in the area of two large circles. Although the comparison approach of intersection distances has worse performance for estimating the MS location compared to the line intersection algorithm in the general case, it has good performance in the specific case. In order to alternately use both algorithms according to the proper case, in this paper, we proposed the mode selection algorithm. The

proposed algorithm compares the distances between the intersection points of the small circle and one large circle to the radius of another large circle. If all distances are shorter than the corresponding radiuses, it selects the specific case mode and employs the comparison algorithm of intersection distances. Otherwise, it selects the general case and employs the line intersection algorithm. The performance for the proposed algorithm was illustrated through computer simulations.

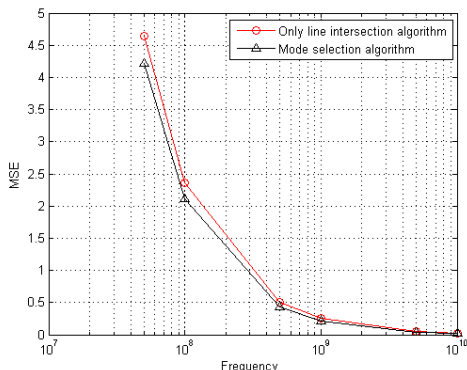


Figure 6. MSE curves for the first scenario for the first case

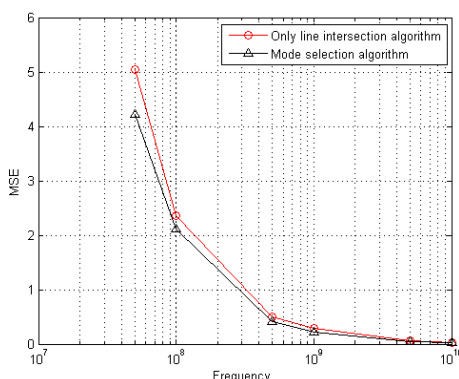


Figure 7. MSE curves for the first scenario for the second case

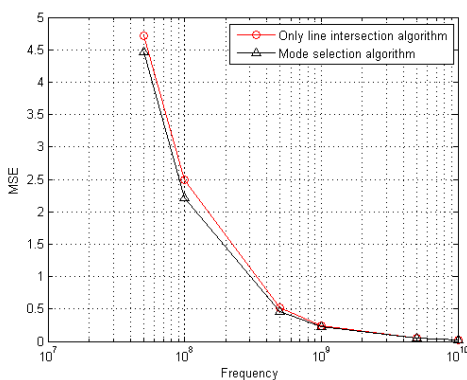


Figure 8. MSE curves for the second scenario for the first case.

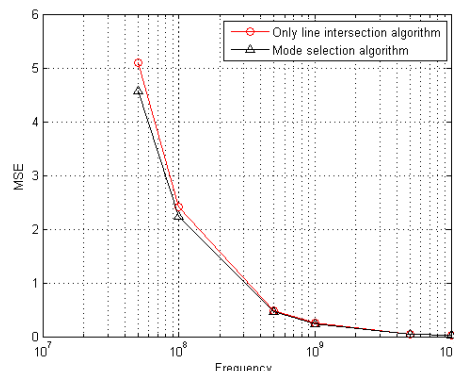


Figure 9. MSE curves for the second scenario for the second case.

ACKNOWLEDGMENT

This research was supported by Basic Science Research Program through the National Research Foundation of Korea (NRF) funded by the Ministry of Education, Science and Technology (No. 2015-053557 and No. NRF-2015R1D1A1A01058827).

REFERENCES

- [1] F. C. Commission, "Revision of the Commission's Rules to Insure Compatibility with Enhanced 911 Emergency Calling Systems," FCC Docket No. 94-102, July 1996.
- [2] C. Drane, M. Macnaughton, and C. Scott, "Positioning GSM Telephones," IEEE Communications Magazine, vol. 36, no. 4, April 1998, pp. 46-59.
- [3] Y. Zhao, "Standardization of Mobile Phone Positioning for 3G Systems," IEEE Communications Magazine, vol. 40, July 2002, pp. 108-116.
- [4] J. J. Caffery, "Wireless Location in CDMA Cellular Radio Systems," Kluwer Academic Publishers, Boston, Mass, USA 2000.
- [5] H. Koshima and J. Hoshen, "Personal locator services emerge," IEEE Spectrum, vol. 37, no. 2, February 2000, pp. 41-48.
- [6] A. Kupper, "Location based services fundamentals and operation," John Wiley & Sons Ltd, The Atrium, Southern Gate, Chichester, West Sussex PO19 8 SQ, England, 2005.
- [7] J. M. Zagami, S. A. Parl, J. J. Busgang, and K. D. Melillo, "Providing Universal Location services using a wireless E911 location Network," IEEE Communications Magazine, April 1998, pp. 66-71.
- [8] S. Tekinay, E. Chao, and R. Richton, "Performance Benchmarking for Wireless Location Systems," IEEE Communications Magazine, April 1998, pp. 72-76.
- [9] S. Pradhan and S. S. Hwang, "A TOA Shortest Distance Algorithm for Estimating Mobile Location," The Journal of the Korea Institute of Electronic Communication Sciences, vol. 8, no. 12, 2013, pp. 1883-1890.
- [10] S. Pradhan, S. S. Hwang, H. R. Cha, and Y. C. Bae, "Line Intersection Algorithm for the Enhanced TOA Trilateration Technique," International Journal of Humanoid Robotics, vol. 11, no. 4, 2014, pp. 1442003.
- [11] S. Pradhan and S. S. Hwang, "TOA trilateration algorithm based on comparison of intersection distances," The 16th International Symposium on Advanced Intelligent Systems, November 2015.

Playback Data Analysis Utility for a LEO Satellite

Dongseok Chae

Satellite Flight Software Team
 Korea Aerospace Research Institute
 Daejeon, Korea
 email: dschae@kari.re.kr

Abstract— All telemetry data generated on a low earth orbit satellite are stored in a mass memory and downlinked to the ground together with the real time data during the contact time. The playback telemetry data are stored in the ground station as a playback raw data file, which includes all types of telemetry frames. The file should be analyzed if there is any error in telemetry format and frame sequences. And also, it needs to separate the file by each frame type, and combine or split the playback files by the size or by the time for the convenience of the post processing. The playback data analysis utility is developed to perform the above requirements. It can be used for analyzing the playback data file generated by the ground test equipment during the ground test phase, as well as the real playback data file received from the satellite. This paper shortly introduces the telemetry data storage and downlink operation in a low earth orbit satellite developed in Korea, and presents the playback data analysis utility program.

Keywords-telemetry; downlink; playback.

I. INTRODUCTION

All telemetry frames generated on the satellite are stored in a mass memory of the On-Board Computer (OBC) [1]. The mass memory data structure is showed in Figure 1, and it is divided into blocks that are called pages. Each memory module has 2048 pages and a page consists of 128 Kbytes. Normally, one memory module is used and the other is ready for the backup. If required, both memory modules can be used at the same time [2]. The page structure is showed in Figure 2. A number of 585 Virtual Channel Data Unit (VCDU) frames are stored on each page. The telemetry frame format is derived from Consultative Committee for Space Data Systems (CCSDS) VCDU format [3].

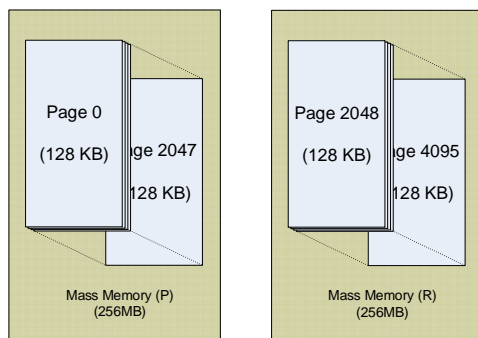


Figure 1. Mass memory structure for telemetry storage

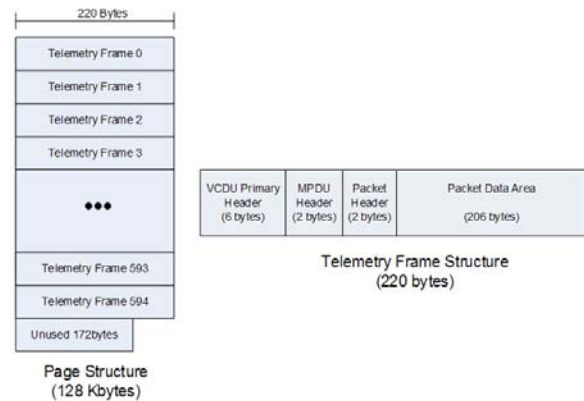


Figure 2. Page and frame structure

There are many telemetry types including several kinds of State of Health (SOH) frames, specified dump area frames, Precision Orbit Determination (POD) related frames, Precision Attitude Determination (PAD) related frames, and so on. Each telemetry frame has its own VCDU ID and sequence counter, and stored in the mass memory in chronological order without overwriting older data which has not yet been downlinked. The newly generated telemetry frames are stored on the memory location pointed out by the current write pointer.

There are two downlink rates: low downlink rate (4096bps) and high downlink rate (1.5626Mbps). Only real time telemetry frames can be downlinked to the ground in the low downlink rate. In the high downlink rate, there are two downlink modes: real-time mode and playback mode. Only real-time telemetry frames are downlinked in the real-time mode and real-time and playback telemetry frames stored in the mass memory are downlinked in the playback mode. 2 real-time frames in low downlink rate and 2 to 4 real-time frames in the high downlink rate can be downlinked to the ground every second. A total of 762 telemetry frames including 2 to 4 real time frames can be downlinked to the ground every second in the high downlink rate.

Playback operation is started by ground commands. Several types of the playback commands are used. Upon receipt of the playback command, telemetry frames are downlinked from the last playback pointer or specified start address designated by the command until the current write pointer or specified end address designated by command is reached. The downlink mode is automatically switched to the

real-time mode when the playback is completed. The playback telemetry data are stored in the ground station as a playback raw data file, which includes all types of telemetry frames. The file should be analyzed if there is any error in telemetry format and frame sequences. And the summary information (start/end time, the total number of frame, the number of each frame, and so on) of the telemetries included in the file need to be exposed. And also, it needs to separate the playback file into the individual frames, and combine or split the playback files by the size or by the time for the convenience of the post processing. The playback data analysis utility program is developed to perform the above requirements. It can be used for analyzing the playback data file generated by the ground test equipment during the ground test phase, as well as the real playback data file received from the satellite. Section II describes the utility program overview. Section III describes the utility program details. And conclusion closes the article.

II. UTILITY PROGRAM OVERVIEW

The major functions of the playback data analysis utility program are as follows:

- Extracts each telemetry frame from the raw data file and check if there is any error in the telemetry frame format and individual frame sequences.
- Reports the file information including start/end time, the total number of frame, the number of each frame, and the error information
- Lists the total frame sequence and the individual frame sequences
- Stores the individual raw data frames in binary or text format
- Combines two playback files and splits a playback file into two playback files

The feature of the program is that it is possible to use easily on the other satellite programs by adjusting the several identification data fields dedicated to each satellite. And it can be used for analyzing the playback data file generated by the ground test equipment during the ground test phase, as well as the real playback data file received from the satellite. There are three types of telemetry data frame lengths in playback file stored in the ground station or the ground test equipment. The data structure of each frame length is described in Table 1. All types of frames can be used as the program input.

TABLE I. DATA STRUCTURE OF EACH FRAME SIZE

Frame Length (byte)	Structure
224	Sync Pattern(4)+VCDU(220)
256	Sync Pattern(4)+VCDU(220)+Reed-Solomon Code(32)
288	Frame Header(64)+VCDU(220)+R-S Code(32)

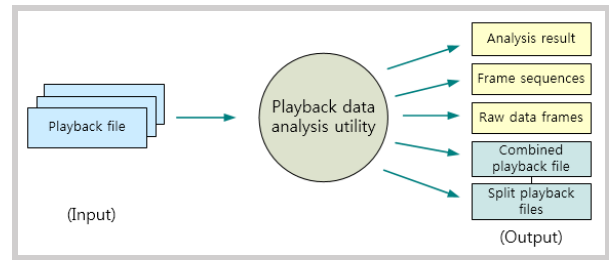


Figure 3. Input / output of the program

Figure 3 shows the input/output of the program. The outputs are the analysis result of the playback data file, frame sequences, individual raw data frames in binary or text format, combined playback file, and split playback files.

III. PROGRAM DETAILS

A. Playback data analysis

When the playback file to be analyzed is selected, the file type and frame size are checked in advance, and then each frame is checked if the header format coincides with the CCSDS telemetry frame format and each VCDU sequence counter is incremented orderly in accordance with each frame type. After extracting and checking all frames included in the file, it displays the check result including the start/end On-Board Time (OBT), the total number of frame, the number of each frame and error information. Total frame sequence and individual frame sequence can be stored as separated files. And individual raw data in binary or text format can be also stored as separated files. The storage of the frame sequences and raw data can be controlled by the user selection wholly or individually. Figure 4 shows the major control process of the playback data file analysis program. And Figure 5 shows the Graphical User Interface (GUI) of the program and an example of the analysis result of a selected playback file. Figure 6 shows an example of the frame sequences and raw data outputs derived from a playback data file.

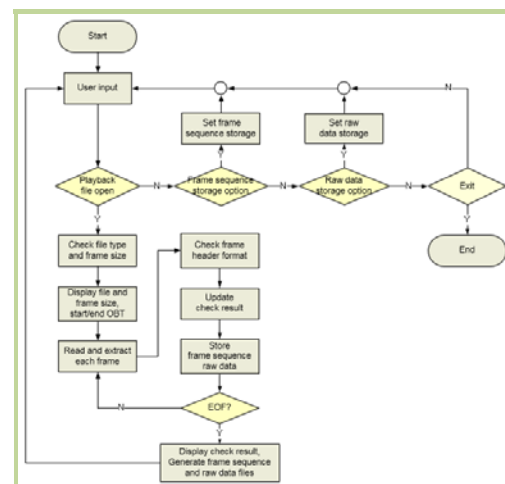


Figure 4 Major control process of the analysis program

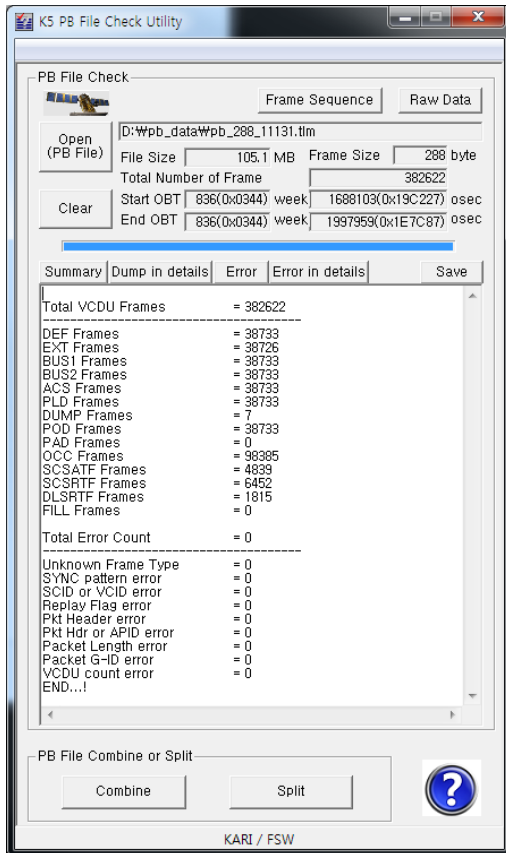


Figure 5. GUI of the playback file analyzer and an example

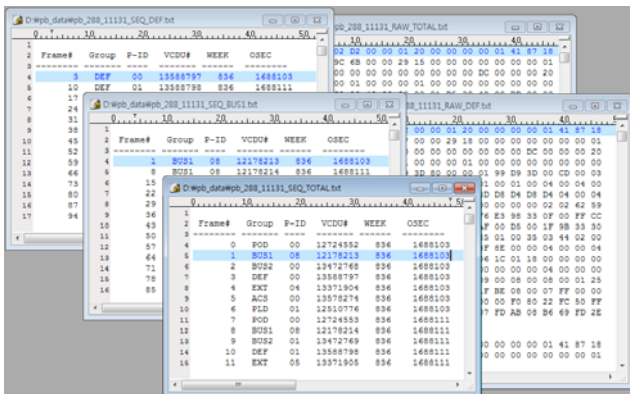


Figure 6 Example of the frame sequences and raw data outputs

B. Playback Files Combine

According to the file size or start/end time of the file, it can be required to combine two playback files. The playback file combine function is used to combine two separate files into a file. When two files for combining are selected, the format and frame size of two files are checked whether they consist of correct format and they are same frame size, and they are also checked the continuity or overlapping. If two files are not continuous in time sequence, the warning message is reported. If two files have overlapping frames,

the number of overlapping frames is calculated automatically and reported. According to the user selection, overlapping frames can be excluded when combined file is generated.

Figure 7 shows the GUI of the playback files combine program and a combining example with two playback files. The information of two playback files before combining and the combined playback file is summarized in Table 2. There are 19 overlapping frames in two playback files and they are excluded in combined file.

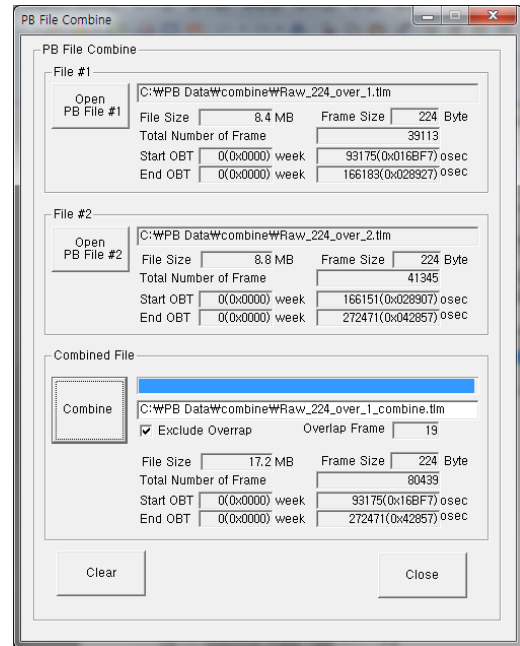


Figure 7. Playback files combine program and an example

TABLE II. PLAYBACK FILES COMBINE EXAMPLE

Item	File #1	File #2	Combined File
File Size	8.4MB	8.8MB	17.2MB
Frame #	39113	41345	80439
Start Time	93175	166151	93175
End Time	166183	272471	272471

C. Playback File Split

According to the file size or start/end time of the file, it can be required to split a playback file. The playback file split function is used to split a file into two separate files. When a playback file for split is selected, basic information about the file such as file size, frame size, start/end time are displayed. And the information about two half sized files are displayed as default. The sizes of two files can be adjusted by Microsoft Foundation Class (MFC) slider control. And more exact file size can be set by writing the number of frame size of the first split file. The information of two files to be split is displayed continuously during adjusting the file size.

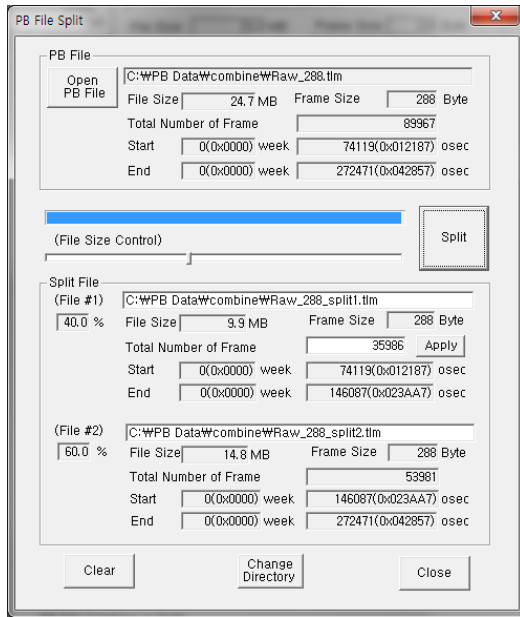


Figure 8. Playback file split program and an example

TABLE III. PLAYBACK FILE SPLIT EXAMPLE

Item	File	Split File #1	Split File #2
File Size	24.7MB	9.9MB	14.8MB
Frame #	89967	35986	53981
Start Time	74119	74119	146087
End Time	242471	146087	272471

Figure 8 shows the GUI of the playback file split program and a split example. The information of the original playback file and two split playback files after splitting is summarized in Table 3.

IV. CONCLUSION

In this paper, the telemetry data storage and downlink operation in a low earth orbit satellite developed in Korea is shortly introduced. And the playback data analysis utility program including playback files combine and split functions are presented. This utility program can be used for analyzing the playback data generated in satellite test phase, as well as the real playback data received from the satellite

REFERENCES

- [1] Y. K. Lee, J. H. Won, and S. K. Lee, "A study of common OBC HW architecture for LEO & GEO satellite", IEICE Technical Report, Oct. 2009, pp. 77-83.
- [2] D. S. Chae, "Telemetry Storage and Downlink Management for a LEO Satellite", SPACOMM, Feb. 2014, pp18-21.
- [3] CCSDS 102.0-B-5 Consultative Committee for Space Data Systems Packet Telemetry.
- [4] CCSDS 873.0-R-2, Spacecraft onboard interface services—file and packet store services, 2011, Draft recommendation for space data system practices.
- [5] J. R. Wertz, W. J. Larson, Space Mission Analysis and Design, Third edition, Microcosm Press, Torrance Ca, USA, 1999.
- [6] G. Casperson, Software System Development for Spacecraft Data Handling & Control, TERMA Electronics AS, 1999.
- [7] Microsoft Visual Studio 2008 version 9.0.21022.8 RTM(C), Microsoft Corporation, 2007.

Preliminary Design of S-AIS Payload for KOMPSAT-6

Yong-Min Lee, Jin-Ho Jo, Byoung-Sun Lee
Aerospace ICT Research Department
Electronics and Telecommunications Research Institute
Daejeon, Republic of Korea
ymlee01@etri.re.kr, jhjo@etri.re.kr, lbs@etri.re.kr

Abstract— Space-based Automatic Identification System (AIS) payload was preliminarily designed for KOMPSAT-6 satellite. The AIS payload is to be a secondary payload of the KOMPSAT-6 satellite. The AIS payload receives and provides the AIS signal data for ship collision avoidance and traffic management by means of on-board processing (OBP) and on-ground processing (OGP). This paper focuses on the preliminary design of AIS payload for KOMPSAT-6 satellite from the point of view of electrical and mechanical interfaces.

Keywords - S-AIS; on-board processing; on-ground processing; KOMPSAT-6.

I. INTRODUCTION

Automatic Identification System (AIS) is basically a short range coastal traffic system used for Ship-to-Ship and Ship-to-Shore (4S) communications. AIS is required to be fitted on every seagoing vessel of 300 gross tons or more. Its purpose is to help ship crews avoid collision with other vessels as well as to allow maritime authorities to track and monitor ship movements [1]. Today's AIS allows ships to communicate with other ships and land based base stations through Very High Frequency (VHF) signals. This means that it is not possible to communicate outside the field of vision.

An AIS receiver in a satellite will extend the range considerably and make it easier to monitor ship traffic and fishing. The altitude of the satellite gives the AIS receiver a long range and the satellite can therefore make observations over large sea areas. The signals are strong enough to be received by a satellite in low Earth orbit by performing the analysis described in [2].

Korea Multi-Purpose Satellite-6 (KOMPSAT-6) is going to be launched for two main missions and one of them is to handle the expected volume of AIS messages around Korean peninsula. A preliminary design of AIS payload has been proposed with emphasis on the interfaces between Integrated Bus Management Unit (IBMU) and AIS receiver, including deployable AIS antennas.

The rest of this paper is structured as follows. In Section II, we present the S-AIS system overview. In Section III, we introduce the preliminary design and we discuss it from the point of view of electrical and mechanical interfaces. Section IV concludes the paper.

II. S-AIS SYSTEM FOR KOMPSAT-6

The main mission objectives of KOMPSAT-6 system are to expedite the provision of the space-borne Synthetic

Aperture Radar (SAR) standard images with sub-meter resolution required for the national demand in Geographical Information Systems (GIS), Ocean & Land management, Disaster monitoring, and Environment monitoring.

The mission applications (“GOLDEN”) are described as follows:

- **GIS:** Acquisition of independent high resolution images
- **Ocean & Land Management:** Survey of natural resources
- **Disaster & Environment Monitoring:** Surveillance of large scale disasters and its countermeasure

The KOMPSAT-6 satellite will be delivered to low Earth orbit in 2020 not only for all-weather day-night monitoring of Korean peninsula, but also for monitoring the ships around Korean peninsula. After achieving mission orbit and implementing In-Orbit Test (IOT), repetitive SAR and S-AIS observations for Earth's land and ocean will be conducted by Korea Aerospace Research Institute (KARI) for 5 years.

The overall operational concept of the S-AIS system is shown in Figure 1.

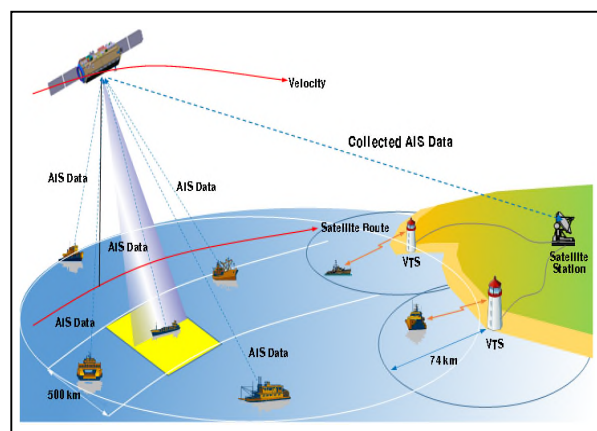


Figure 1. Operational Concept of S-AIS System for KOMPSAT-6

The AIS payload is to be placed in KOMPSAT-6 platform and the mission objectives of AIS payload are as follows:

- AIS signal collection from vessels on sea

- Raw data sampling for OGP (On Ground Processing) mode
- Demodulation of AIS burst signals for OBP (On Board Processing) mode

III. PRELIMINARY DESIGN

Space-based AIS payload has its own challenges due to the fact that AIS is primarily intended for sea-level reception and therefore leads to performance degradation when observed over large areas from space.

Another issue is the message collision and the message loss. All exchanged messages which are transmitted from ships on the sea should be synchronized and guaranteed the functions of the system without any message loss. On the other hand, all AIS messages received by the satellite from lots of vessels at the same time with the same frequency cause a message collision and lead to message loss [3].

In order to resolve the expected concerns above, S-AIS was designed as a reconfigurable AIS payload which operates in both on-board processing mode and on-ground processing mode, depending on the shipping traffic conditions of the field-of-view. Furthermore, the enhanced de-collision algorithms have been applied to successfully decode the collided signals during preliminary design phase.

A. Electrical Interface Design

The IBMU primary (RCL, PPS and COM) is connected to the AIS receiver primary (hot), and the IBMU redundant is connected to the AIS receiver redundant (cold), as shown in Figure 2. The AIS payload has the following electrical interface characteristics.

- RS-422/RS-485: 115.2 kbps, 230.4 kbps, 460.8 kbps and 921.6 kbps (Baud rate is selectable)
- PPS input: RS-422/RS-485
- Redundancy control: RS-422/RS-485
- Connectors: Antennas: SMA 50 Ohm female,
- Power: High performance micro D-subminiature
- Serial: High performance micro D-subminiature

This configuration offers complete redundancy on all parts and quadruple redundancy on the decoder boards and most of interface board.

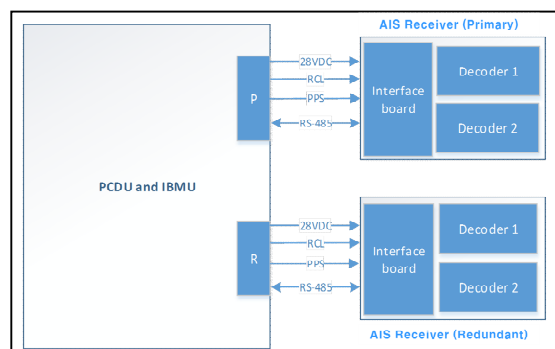


Figure 2. Electrical Interfaces between AIS Receiver between PCDU/IBMU

The Interface Board contains an RF front-end filter, one Low Noise Amplifiers (LNAs) for each antenna, external interface connectors, board connectors, power supply, and communication transceivers.

The RF front-end consists of a lumped RF filter followed by an LNA and switch. The redundancy control switch is used to route the output signal to the active Decoder Board. The 28VDC input supply is to be regulated to +5.0VDC (Volts of Direct Current) using two (one hot and one cold redundant) non-isolated DC/DC (Direct Current to Direct Current) converters. The DC/DC converters are enabled/disabled by the redundancy control signal, thus choosing which of the two Decoder Boards to be active. The regulators powering the RF front-end electronics are fed from the Decoder Board while the interface electronics are powered by regulators fed by the +5.0VDC. All transceiver circuits for the communication interfaces are also contained in the Interface Board and the interface transceivers are duplicated for redundancy purposes and the output enable pin is controlled by the redundancy control signal.

The Decoder Board contains the rest of the analogue receiver chains, analogue-to-digital converters and the digital platform for on-board processing and sample recording as shown in Figure 2. The digital hardware is based on a Field Programmable Gate Array (FPGA) and an anti-fuse FPGA is used to mitigate Single Event Upsets (SEUs) on the SRAM FPGA configuration data. A well proven watchdog functionality is implemented in the Anti-fuse FPGA as well.

The overall reliability value for AIS receiver is dependent on many factors. Primarily, it is the average lifetime ambient temperature and the average thermal cycles per orbit integrated over the lifetime that set the reliability figures. The temperature cycles per orbit integrated over lifetime is based on Coffin-Manson relationships, and is often not part of traditional reliability calculations. It is expected that the temperature cycles will only affect the board level soldering reliability. Table I shows the results of reliability calculations for the AIS receiver based on operating temperatures.

TABLE I. RELIABILITY CALCULATION FOR AIS RECEIVER BASED ON OPERATING TEMPERATURES

Ambient Temperature (T _a)	Temperature Cycles (ΔT)	Failure in Time (FIT)	Reliability R(t)
20 °C	±0 °C	182,5	0,9920
	±2.5 °C	222,2	0,9903
	±5 °C	278,2	0,9879
	±10 °C	507,1	0,9780
	±15 °C	917,3	0,9606
30 °C	±0 °C	391,8	0,9830
	±2.5 °C	414,3	0,9820
	±5 °C	479,6	0,9792
	±10 °C	846,2	0,9636
	±15 °C	1311,1	0,9442
40 °C	±0 °C	769,9	0,9668
	±2.5 °C	796,3	0,9657
	±5 °C	871,2	0,9626
	±10 °C	1175,7	0,9498
	±15 °C	1682,1	0,9290

B. Mechanical Interface Design

The mechanical interfaces design has been carried out for the AIS receiver and the AIS antennas mounting on the spacecraft. The unit accommodation design for KOMPSAT-6 is in a preliminary design phase so far. Mounting configurations of AIS receiver [4] and locations of antennas on the spacecraft are shown in Figure 3 for AIS receiver and Figure 4 for AIS antennas, respectively.

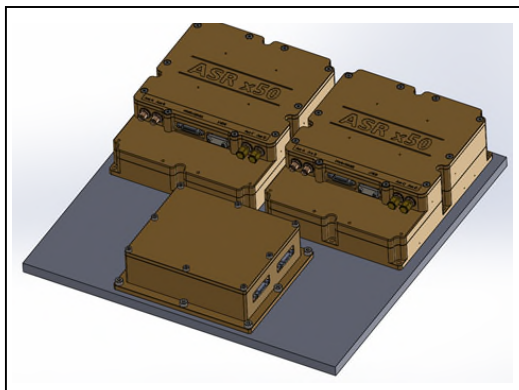


Figure 3. AIS Receiver Mechanical Configuration for Accommodation

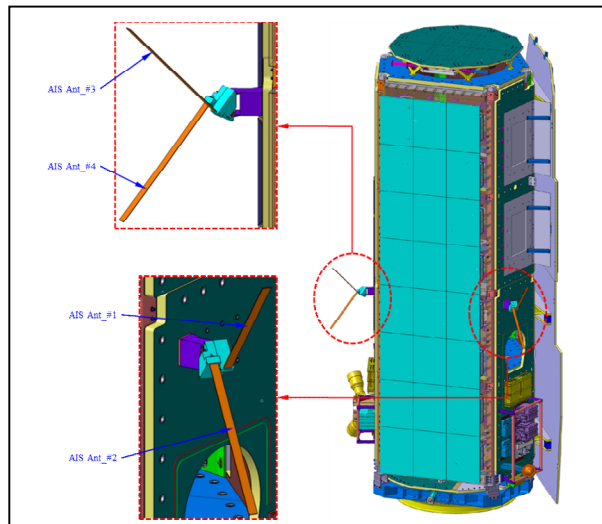


Figure 4. AIS Antennas Accommodation Design on Spacecraft

The AIS receiver consists of three inter-connected boards in a housing with all external connectors mounted at a recessed top front. The mounting points to the satellite structure are placed on a single plane at the bottom of the receiver. The enclosure is made as a non-magnetic metallic case which forms an all-enclosing electromagnetic and radiation shield. The mechanical design assumes a spacecraft manufacturing tolerance of $\pm 0.1\text{mm}$.

IV. CONCLUSIONS

ETRI is now aiming to design and develop the S-AIS system for KOMPSAT-6 using the experiences and well trained engineers from previous project, development of Communication, Ocean and Meteorological Satellite

(COMS). S-AIS is a system for AIS signal collection, down conversion, and demodulation of the AIS burst signals from vessels on the sea operating at VHF band.

In this paper, we have looked at electrical and mechanical interfaces of S-AIS system as a part of the preliminary design of AIS payload for KOMPSAT-6 satellite.

It is expected that the critical design and analysis will be performed in order to fix the S-AIS payload design as part of short term activities and future work.

REFERENCES

- [1] Guidelines for the Onboard Operational Use of Shipborne Automatic Identification Systems (AIS), IMO Resolution A.917(22).
- [2] Y. M. Lee and B. S. Lee, "Preliminary Performance Analysis of Space-based AIS Payload for KOMPSAT-6", SPACOMM 2015, April 19 - 24, 2015.
- [3] R. Goldsmith, "Preparatory Action for Assessment of the Capacity of Spaceborne Automatic Identification System Receivers to Support EU Maritime Policy : The PASTA MARE Project", Maritime forum, October 2010.
- [4] Design Definition File Summary Report, Issue 1A, ASRx50-KSX-DDF-014, Kongsberg Seatex AS, 2015.

Performance Analysis of Operational Ka-band Link with Kepler

Timothy Pham, Jason Liao
 Jet Propulsion Laboratory
 California Institute of Technology
 Pasadena, California, USA

e-mails: Timothy.Pham@jpl.nasa.gov Jason.Liao@jpl.nasa.gov

Abstract - This paper presents some observations on the signal behavior from an analysis of Kepler Ka-band link. The goal is to characterize the link performance with operational data obtained from the Deep Space Network (DSN) tracking of Kepler spacecraft. Kepler is the first mission supported by the DSN that uses Ka-band as a primary means to return science data. We examine how operational data may differ from the expectation. Operational data often show many surprises where data variations occur without an apparent cause. We try to quantify the signal power fluctuation so that future missions can adequately plan for the link design, especially for missions that operate with lower margin. We also attempt to quantify the effect of rains/heavy clouds and high winds.

Keywords - DSN; performance analysis; weather statistics; Kepler; Ka-band operations

I. INTRODUCTION

The National Aeronautics and Space Administration (NASA) Deep Space Network (DSN) serves as a communications infrastructure to enable mission controllers communicate with their spacecraft exploring the outer space. The DSN currently comprises of 13 antennas operating at multi-frequency of 2 GHz S-band, 8 GHz X-band and 26 GHz & 32 GHz Ka-band. The majority of 30-plus missions supported by the DSN use X-band. A few still use the narrower S-band while some are moving to the new broader Ka-band. Compared to X-band operation, Ka-band offers missions greater bandwidth that better supports higher data rates. The International Telecommunications Union allocates about 500 MHz for deep space Ka-band (32 GHz) and 1.5 GHz for the near Earth Ka-band (26 GHz), compared to 45 MHz each for deep space and near Earth X-band. Ka-band operation also offers roughly 5.5 dB advantage in the signal-to-noise ratio (SNR) performance, compared to the X-band operation, assuming the same transmitting power [1]. The 5.5 dB advantage is a result of a higher antenna gain at Ka-band due to greater operating frequency, mitigated by the higher system noise temperature.

Kepler mission is the first deep space mission that uses the 32-GHz deep space Ka-band as an operational link for telemetry return. The higher link performance, afforded by a higher SNR compared to the X-band link, allows for faster data downlink and enables spacecraft to devote more time on the collection of science data. Although Ka-band downlink was also conducted on some earlier missions, such as the Mars Global Surveillance (MGS) and Mars Reconnaissance Orbiter (MRO), it was only for the purpose

of technology demonstration - X-band was still the primary link for telemetry return. Two other ongoing missions - Cassini and Juno - has Ka-band signal, but it is a carrier only (without modulated telemetry) for the purpose of conducting radio science investigations. The received carrier's power, frequency and phase are used to infer the characteristics of planetary medium that the signal traverses.

Kepler mission has the advantage of operating at high SNR. Its healthy designed link margin, in the range of 4-5 dB, provides greater buffer to the impact of inclement weather. Other Ka-band missions to be launched in the near future, such as the Solar Probe Plus, will be operating at a much lower link margin. Thus, there is a strong interest in characterizing the link performance and signal fluctuation for better link design for future missions.

In this paper, we examine the data collected from Ka-band tracking of Kepler over yearlong period and try to provide the answer to these questions:

- (1) What is the typical variation in the signal SNR from one tracking pass to the next?
- (2) How often does rain negatively affect the link and cause data outage? How does the link behave in the presence of rains or heavy clouds?
- (3) How often does high wind affect the antenna pointing and thus the link performance? How much degradation does the signal experience?
- (4) What is the cumulative probability distribution of the signal fluctuation?

In Section II, we briefly describe the Ka-band operations of Kepler mission. General observations of the received signal characteristics, especially their variation from pass to pass, are discussed in Section III. Passes affected by the rain or cloud and high wind are discussed in Section IV and Section V, respectively. Section VI examines the statistics of signal power fluctuation. Conclusions are captured in Section VII.

II. KA-BAND OPERATIONS

The DSN has three tracking complexes spread evenly across the Earth longitudes in order to maintain a constant visibility with spacecraft in deep space. The three complexes are named the Goldstone, Canberra and Madrid Deep Space Communications Complexes, based on its location in the United States, Australia and Spain. The majority of the antennas are 34-m, with one 70-m at each site. Goldstone Complex currently has five operating antennas devoted to spacecraft tracking. Madrid and Canberra Complex each has four antennas. Within each

complex, two 34-m antennas are equipped with 32-GHz Ka-band reception that can be used to support Kepler and other missions, such as Cassini and Juno. For a complete description, the DSN also supports the 26-GHz near-Earth Ka-band with one 34-m antenna at each complex. The near-Earth Ka-band is relevant to some near future missions, such as the Transiting Exoplanet Survey Satellite (TESS) in 2017 and the James Webb Space Telescope (JWST) in 2018. The analysis of this paper is done with the 32 GHz Kepler data; however, the findings should be applicable to the operations at 26-GHz near-Earth Ka-band due to spectral proximity.

The Kepler spacecraft uses two different frequencies, X- and Ka-band, for return telemetry data. The spacecraft relies on X-band for the return of low-rate spacecraft engineering data (up to 16 kbps) and for radiometric measurement (e.g., Doppler and ranging). X-band tracking occurs every three or four days, more often than Ka-band tracking. Once a month, when the science data buffer onboard spacecraft is nearly full, Kepler spacecraft would turn its Ka-band high gain antenna to Earth and downlink the high-rate science data (up to 4.3 Mbps) that are collected over the month-long observations. The Ka-band downlink sessions last several hours and typically take place over two DSN complexes. X-band data are also received concurrently with Ka-band. The dual-frequency links offer an opportunity to validate the observed signal fluctuation. If it is caused by common source of errors, such as bad weather or pointing problem on the ground or flight antenna, the effect would show up in both links, with a smaller effect expected on the lower X-band frequency link.

III. SIGNAL VARIATIONS

In this section, we look at the performance characteristics of Kepler Ka-band passes. Figure 1 shows the link characteristics of all Ka-band passes in 2012. For each pass, the average telemetry symbol SNR (SSNR) and associated standard deviation, the observed SSNR minima and maxima are plotted. The label “DOYxx/DSS-xx” indicates the day of year (DOY) the pass took place and the antenna – Deep Space Station (DSS) – used for tracking (Goldstone: DSS-25 and -26; Canberra: DSS-34 and -35; Madrid: DSS-54 and -55).

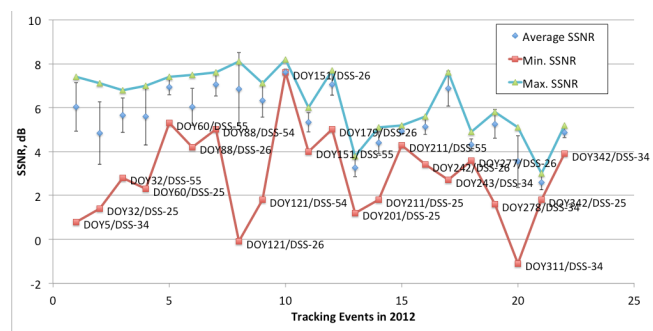


Figure 1. SNR characteristics of Kepler Ka-band passes

The data reflect the following observations:

1. The average SSNR varied quite significantly among the passes, as much as 4.8 dB (2.3 dB - 7.1 dB). Some factors affecting the variation are:
 - (a) There is some performance difference among the DSN antennas used for the tracks.
 - (b) Tracking passes are done at different elevation, as dictated by the selected antenna and the time of actual downlink within the pass. This results in different system noise temperature level.
 - (c) Different data rates are used in the downlink, which affects the signal energy and thus, the symbol SNR.
 - (d) Change in the spacecraft range from Earth.
 - (e) Potential degradation from the rains/clouds or winds.

One could theoretically normalize these geometric and link variations among the data of different passes to remove the effect of factors (b), (c) and (d). That would have resulted in a smaller variation, leaving just the effect of factors (a) and (e) remained. As a note, we estimate that the variation due to the ground and spacecraft antenna pointing error was small (less than 0.2 dB) because of the active conical scanning tracking used in the ground antenna pointing and because of spacecraft pointing precision driven by stringent science objectives.

On the link robustness, we note that the average SSNR of all Ka-band passes is about 5.5 dB. That level provides a healthy 6.2 dB link margin relative to the -0.7 dB threshold required for successful decoding of the concatenated convolutional (7, 1/2) and Reed Solomon (255, 232) codes that is employed in Kepler link. With such a large margin, it is expected that Kepler link be well protected against potential outages.

2. The standard deviations also varied among the passes. Some passes had standard deviation as small as 0.25 dB while others had deviation up to 1.4 dB. The passes with small standard deviation demonstrate that the SSNR measurements are stable down to 0.25 dB level. The passes with large standard deviation prompt a greater interest because they reflect atypical conditions that can negatively affect the link design. Two of these passes - DOY121/DSS-26 & DOY243/DSS-34 - were exposed to high wind, up to 45 kph. One pass - DOY32/DSS-55 - experienced rain. Other passes, such as DOY211/DSS-25, had a large SSNR fluctuation but the cause was not well understood. More specific detailed analysis of these atypical passes is discussed later in Section VI.

3. The SSNR minima generally lie further away from the average SSNR. Some of them were in the 3-sigma range, such as the passes on DOY121, DOY247 and DOY311. This large difference indicates that the signal likely experienced some large SNR drops caused by short bursts of impact.

4. The SSNR maxima generally lie close to the average values, not too far from the upper 1-sigma point. This is due to a non-Gaussian distribution of the measurements, as later seen in Section VI, where most of the points are close

to the maximum SNR level. They are not separated from the average values by 2 - 3 sigma.

There are a few observations about the data processing:

(1) Kepler occasionally changes the data rate in mid pass. So, the computation of representative metrics for the link performance – SSNR average, standard deviation, minima and maxima - need proper filtering to single data rate. Without such filter, the computed link metrics, especially the standard deviation, would be larger than what they actually are.

(2) Data on Ka-band link need to be separated from the X-band link. However, the positive benefit of having concurrent X-band data is that we can use it to validate the common impacts caused by environmental factors, such as winds and rains.

(3) Some of the passes were configured with dual receivers on Ka-band, for redundant processing. We expect that the measurements from both receivers would be within the 0.25 dB measurement noise indicated earlier. Such consistency can be seen in the upper plot of Figure 2 for DOY032/DSS-55 pass, where the difference between the two receivers was within 0.1 dB. Yet, there are passes where we observed a greater difference, as shown in the lower plot of Figure 2 for DOY342/DSS-25 pass. Here, the SSNR measurements reported by the two receivers differed on the average by 0.7 dB.

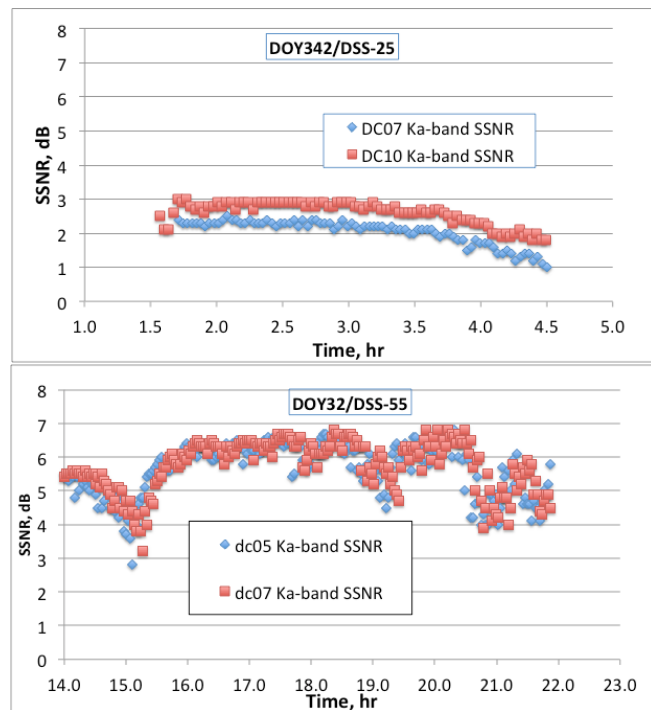


Figure 2. Variation of SSNR measurements from the two receivers on the same antenna in DOY32/DSS-55 and DOY342/DSS-25 passes

Fortunately, in this study, since we are less concerned with the absolute SSNR level between passes and more interested in the signal fluctuation within the pass, this measurement difference does not negatively affect the

analysis. If our analysis objective were to evaluate the loss in the ground system, this difference would have some impact.

IV. IMPACT OF RAINS/CLOUDS

In 2012, there was one Ka-band passes affected by rain or heavy clouds. The water content in the air column reduced the SSNR by as much as 3 dB. Figure 3 shows the SSNR variation in DOY32/DSS-55 pass over Madrid. The Ka-band SSNR measured by both receivers reflected a 3 dB, 2.5 dB and 3 dB drop near the time 15:00 hr, 19:00 hr and 21:00 hr, respectively. The X-band SSNR showed a similar degradation but with smaller impact, in the order of 1 dB, as expected. The drops in SSNR matched with the increases in the system noise temperature (SNT) around the same time. This correlation implies an impact from the external environment.

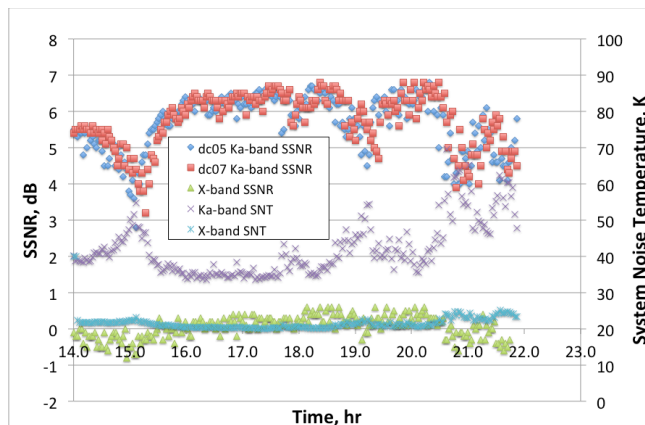


Figure 3. Variation of symbol SNR and system noise temperature at Ka- and X-band on DOY32/DSS-55

Each DSN Complex has a weather station that measures the wind speed/direction, humidity and precipitation. The precipitation data reflects the rainfall as measured by a rain gauge. The weather station however does not provide measurement on cloudiness where the water content in the air column would affect the system noise temperature and causing signal degradation. For the DOY32/DSS-55 data set, despite the presence of the SSNR variation, there was no indication of rainfall from the precipitation measurement. The absence of rain would make it hard to pinpoint the link between the SSNR degradation and weather. The only available collaborating evidence is the increase in the measured system noise temperature. Fortunately, we are able to independently confirm the system noise temperature measurement with the data from special research equipment called the Advanced Water Vapor Radiometer (AWVR) that independently measures the water content in the air. The AWVR is available at Goldstone and Madrid complex, but not Canberra, and has been in operations for over two decades. The AWVR measures the sky brightness temperature at 31.4 GHz [2]. The water vapor radiometer

data are collected continuously throughout the day, one sample every 10 minutes. The measurements are done at zenith but the data can be translated to any elevation of interest so that they can be compared with the measured system noise temperature of the pass (which is done by a different set of equipment, using the Y-factor method with a small injected noise-diode) [3]. This AWVR elevation translation however produces a uniform estimated noise temperature in all azimuth directions. In contrast, the SNT measurement is azimuth specific because the measurement is done along the line of sight of antenna tracking spacecraft. So, there may be some difference in the absolute measurements between the two data sets. Nevertheless, we found the data with reasonable consistency. Figure 4 shows the AWVR-derived noise temperature on DOY32 at 40-deg elevation, approximately the same elevation of Kepler tracking at 21:00 hr [4].

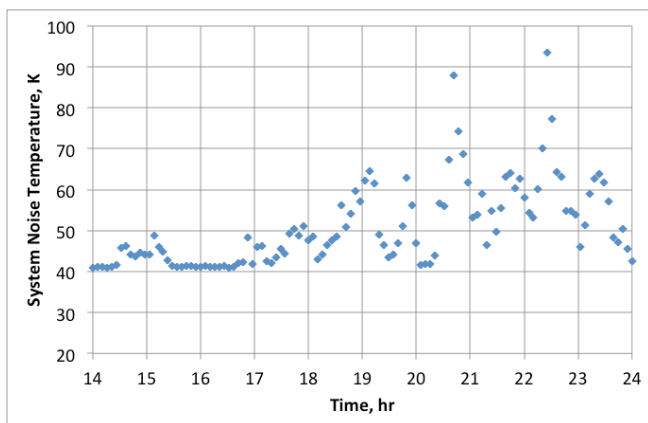


Figure 4. AWVR system noise temperature for DOY32/DSS-55

The temperature is observed to vary significantly at 18:00 hr, with big bursts of 30 K or more near 21:00 hr, which is consistent with the variation seen in the SNT measurement in Figure 3.

V. IMPACT OF WINDS

There are two tracking passes - DOY121/DSS-26 at Goldstone and DOY243/DSS-34 at Canberra - with high wind condition, up to 45 km/hr. The impact of wind on the SNR degradation is quite apparent on DOY243 while it is more ambiguous on DOY121.

We first look at the DOY243 data. Figure 5 shows the measurements of symbol SNR and carrier SNR (Pc/No), as well as the system noise temperature and wind speed on DOY243. Both the SSNR and Pc/No showed high level of fluctuation during the first hour of the pass. Several big drops in SNR occurred at the same time for both measurements, indicating the phenomenon was real rather than just a measurement error. The relatively constant system noise temperature implied that the variation in the SNR was in the signal power reduction rather than in the increased noise (as caused by rains or clouds). There were

high winds, up to 45 kph, in the earlier part of the track. Some of the highest peaks of wind speed aligned with the drops in the SSNR and Pc/No, as much as 4 dB. These sudden SNR drops are what cause the SNR minima of the pass to be much lower than the one-sigma point below the average SSNR, as mentioned earlier in Section III.

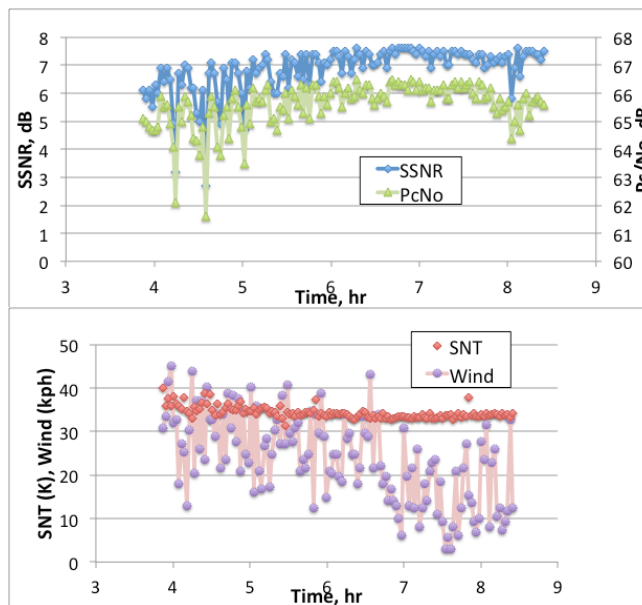


Figure 5. Variation of SNR, system noise temperature and wind speed on DOY243/DSS-34

Figure 6 shows a correlation between the SNR degradation and the wind speed. Here, the SNR degradation is defined as the difference between the SSNR maxima of a given pass (which is considered as the best possible SSNR without degradation) and the measured SSNR within the pass. A second order polynomial curve fit, with a forcing constraint of having zero degradation at zero wind speed, is also included. At 45-kph winds, the fitted degradation can be as much as 2 dB; however, we should note that the r-squared value is low at 0.29, indicating a large uncertainty with the fitting.

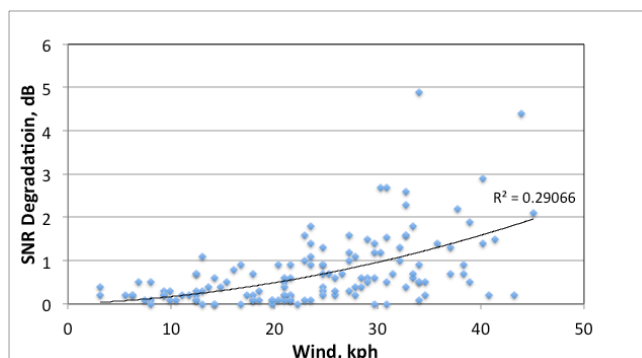


Figure 6. Correlation of SSNR degradation and wind speed on DOY243/DSS-34

Next we examine the other data set with high winds on DOY121/DSS-26. Figure 7 plots the SSNR, Pc/No, system noise temperature and wind speed for that pass. Both SSNR and Pc/No showed a drop around the time of 23.8 hr. The characteristics are however different. While the SSNR drop was prominent and abrupt, as much as an 8 dB in less than 6 minutes, the Pc/No drop was more gradual, just about 1 dB over 20 minutes. This raises an uncertainty on the SSNR measurement over this period of impact. Although the symbol tracking was reported to be in lock, we suspect it might be in error and thus, affected the reported SSNR.

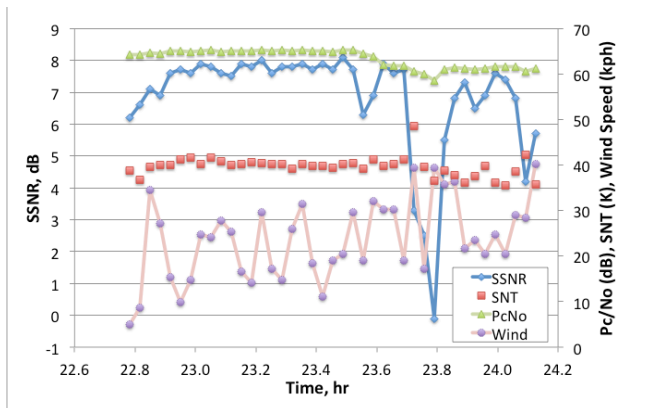


Figure 7. Variation of SNR, system noise temperature and wind speed on DOY121/DSS-26

Figure 8 reflects a possible correlation between the SNR degradation and the wind speed. The polynomial fit indicates a degradation of 3.1 dB at 40 kph; however, it is a relatively low-confidence fit, with an r-squared value of 0.19. One reason for the poor fit is the presence of some data points that are out of normal expectation. For example, the first two data points where the wind is below 10 kph seem to be erroneous. These are the same measurements right after successful signal acquisition, as indicated in the previous Figure 7 around the time 22.8 hr. There are also other data points with anomalous large degradation. Because the receiver reported the signal was in lock and there was no other indication that invalidate the measurements, we decide to keep these out-of-the-norm data points in the analysis, rather than rejecting them.

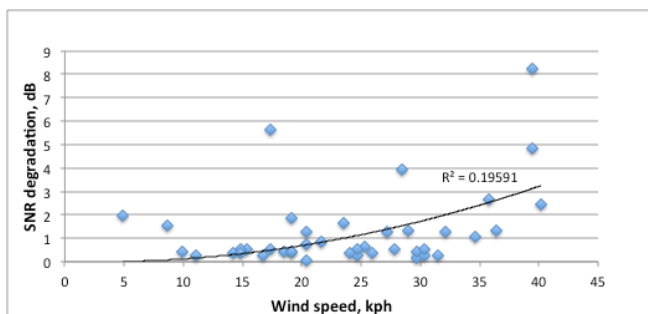


Figure 8. Correlation of SSNR and wind speed on DOY121

The above example reflects some of the challenges with data processing, e.g., what to include vs. exclude in the data analysis in order to arrive at the right model. Some operational measurements are not as consistent as we like them to be.

VI. SIGNAL FLUCTUATION STATISTICS

We are interested in characterizing the probability distribution of the signal variations to aid with the link design in future missions. In an ideal case, if there were accurate prediction on the signal SNR, any operational degradation would be reflected as a deviation of the measurement from the prediction since the prediction are model-based and have no knowledge of real-time weather impact. Unfortunately, predictions are not available with Kepler Ka-band passes.

To compensate for the lack of SNR prediction, we calculate the fluctuation by a degradation against the maximum SSNR of the pass, as discussed in Section V. Additional adjustment is also needed since both the antenna gain and system noise temperature change as a function of antenna elevation [5]. The antenna gain is affected by the gravity distortion of the antenna structure. The system noise temperature varies due to different path length through the Earth atmosphere that the signal traverses at different elevation. Lower elevation results in a higher noise temperature because of the longer atmospheric path.

For each pass, the measured SSNR's are subtracted from the SSNR maxima of the pass. Fluctuation data of all Ka-band passes in 2012 are then combined to generate the cumulative distribution function of SNR variation, as shown in Figure 9.

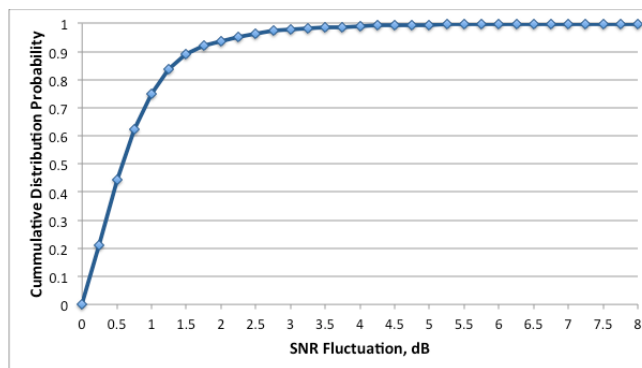


Figure 9. Cumulative distribution of SNR fluctuation

The distribution shows that 50% of the fluctuations are less than 0.6 dB, 90% are within 1.6 dB, and 95% being less than 2.2 dB.

VII. CONCLUSION

In summary, this paper examines the variation of Kepler Ka-band signal observed from the DSN tracking. In a benign condition, the SSNR measurements within a pass are stable within 0.25 dB. In adverse weather of heavy clouds or winds, the SSNR within the pass can vary as much as 1.5

dB (1-sigma). Out of 22 Ka-band passes in 2012, only one pass was affected by the heavy clouds (no rains) and two passes impacted by high winds. Both of these effects could result in an instantaneous change of SNR by up to 3 dB. Kepler mission, however, has a robust link with an average 6.2 dB margin, which helps minimizing the telemetry data outage. The cumulative distribution of the SSNR variation shows that 50% of the variation are within 0.6 dB of the maximum SSNR within the tracking pass, 90% are within 1.6 dB and 95% within 2.2 dB.

Through this analysis, we learned that one has to be careful with the data selection. Since a track could involve multiple receivers at multiple frequency (X- and Ka-band) and multiple data rates (spacecraft can change data rate within the pass to preserve link margin), proper filtering of data is essential for valid data compilation and analysis. Compensation for the changing elevations in the signal SNR is required to normalize the data to the same conditions. We also learned that while measurements from two different receivers of the same received Ka-band signal are generally the same to within 0.25 dB, at times they could differ by as much as 0.75 dB. This difference would have greater impact on future studies, such as system loss, that are dependent on the absolute, rather than relative, accuracy of the SSNR measurements.

ACKNOWLEDGMENT

The work described in this paper was carried out by the Jet Propulsion Laboratory, California Institute of Technology, under a contract with the National Aeronautics and Space Administration.

REFERENCES

- [1] S. Shambayati, "A Comparison of the Ka-band Deep-Space Link with the X-band Link Through Emulation," The Interplanetary Network Progress Report 42-178, Jet Propulsion Laboratory, Pasadena, California, August 15, 2009, p. 48.
- [2] A. Tanner and A. Riley, "Design and Performance of a High Stability Water Vapor Radiometer," *Radio Science*, vol. 38, no. 3, March 2003, pp.15.1–15.12.
- [3] C. T. Stelzried, R. C. Clauss, and S. M. Petty, "Deep Space Network Receiving Systems' Operating Noise Temperature Measurements," The Interplanetary Network Progress Report 42-154, April–June 2003, Jet Propulsion Laboratory, Pasadena, California, August 15, 2003, pp. 1–7.
- [4] S. Slobin, personal communications, Jet Propulsion Laboratory, Pasadena, California, October 15, 2015.
- [5] DSN Telecommunications Link Design Handbook (810-005), Module 104, 34-m BWG Antennas Telecommunications Interfaces, Jet Propulsion Laboratory, Pasadena, California, April 1, 2015, pp. A-1–A-12.

Simulation of SAR Jammer Techniques and Hardware Implementation for Point Scatterer Modelling

Emrah Ener

Rehis

Aselsan Inc.

Ankara, Turkey

e-mail: eener@aselsan.com.tr

Abstract— In this paper, the effectiveness of different jamming techniques against synthetic aperture radar (SAR) systems is provided. Some derivations regarding the noise jamming immunity of SAR systems are made and the results obtained are compared with the simulation results. Noise jamming techniques based on playback of pre-recorded noise sequence and repeater techniques based on random false targets are proposed. Simulations are used to show the effectiveness of those techniques for different jamming to signal ratios. A hardware structure for SAR jammer is proposed together with possible simplifications.

Keywords- SAR; Electronic Counter Measure (ECM) ; Noise Jamming.

I. INTRODUCTION

SAR is an imaging radar which transmits phase or frequency coded pulses to target region and forms 2D reflectivity image by coherently processing collected pulse returns. The final image is the Radar Cross Section (RCS) Distributions of point scatters on the surface. Different from their optical counterparts, SAR radars can form high resolution images of target regions in all weather conditions.

Jamming against SAR systems can be thought as protecting strategic regions from monitoring and this makes it an important problem in Electronic Warfare (EW). Jamming a SAR system is an easier problem compared to conventional radar jamming in some ways. SAR systems usually work with a fixed Pulse Repetition Interval (PRI) and frequency which makes them unprotected against jammer tracking. They also have large bandwidth and can easily be located in frequency by Electronic Intelligence (ELINT) systems.

It is also hard to generate an effective ECM signal against SAR systems. First of all, SAR radars are always highly coherent radars with both fast time and slow time operations in their receivers and this makes them immune to noise jamming. SAR images have high correlation, so low pass filtering or reconstruction algorithms using this correlation can be used to correct jammed images.

SAR Jamming has been studied for a long time but it is still a current research area. Several studies on the simplest jamming technique, noise jamming effectiveness have been published [1], [2]. Deceptive techniques using Digital Radio Frequency Memory (DRFM) which create spurious images in SAR scene is also a popular research area [3], [4]. Electronic Counter Counter Measure (ECCM) techniques for

countering SAR jammers have been studied deeply due to their similarity to conventional radar ECCM [5][6][7].

The rest of the paper is structured as follows. In Section II, an introductory information on SAR performance parameters and image construction is provided. Section III gives a classification of SAR ECM techniques in literature together with a comparison of their effectiveness. In Section IV, simulation results regarding the effectiveness of different jamming techniques will be provided. In Section V, a hardware structure for implementing SAR jammer will be proposed. Section VI concludes the paper.

II. SAR BASICS

One of the most important performance criteria for imaging radars is the final image resolution. Since SAR is a 2D imaging system, resolution is defined in both range and azimuth. Resolution in range can be improved by using pulse compression techniques. Resolution in azimuth can be approximated using 3dB pattern width times the range (R).

The cross range resolution ΔCR can be approximated using (1) where λ is the wavelength and L_{az} is the antenna size in azimuth direction [9]. For a low resolution at long range, the antenna size requirement becomes unrealizable.

$$\Delta CR = R \frac{\lambda}{L_{az}} \quad (1)$$

In SAR systems, a synthetic antenna array is formed by using the assumption of limited change in imaging region and a uniform motion of the radar platform during the imaging period. By using the size of this synthetic array, a large azimuth size L_{az} and high azimuth resolution is obtained for imaging. During the motion of the platform, a sequence of pulses is transmitted in the direction perpendicular to the platform motion. The pulses are transmitted at a rate defined by pulse repetition interval (PRI). If the platform speed is given by v and the duration of pulse integration is T_{INT} , then the aperture length will be the platform speed times the pulse integration time. The resultant azimuth resolution of the constructed image can be calculated using (2). [9]

$$\Delta CR_{SAR} = R \frac{\lambda}{2vTA} \quad (2)$$

There is a large number of algorithms related to image formation for SAR. Since these are not related to the subject of this paper, only a brief summary of the simplest algorithm (Doppler Beam Sharpening) going back to 1965 (Carl Wiley) will be described here.

The position of a point scatterer on a target region can be defined by using the axis parallel to platform motion (X axis) and the range axis (R) perpendicular to the motion. Let u define the position of the platform on synthetic aperture. If the distance to the imaging region is much larger than the diameter of the target region, then the distance to the point scatterer can be approximated using (3) where x is the position on X axis.

$$R(u) = \sqrt{(u-x)^2 + R^2} \approx R + u \frac{x}{R} + \frac{x^2}{2R} \quad (3)$$

Assuming the output of fast time match filter is approximated by $\delta_D(t-R(u))$ in baseband, the phase lag $\Theta(u)$ of pulse return from a point scatterer at coordinates (x,R) can be calculated using (4).

$$\Theta(u) = (R + u \frac{x}{R} + \frac{x^2}{2R}) \frac{4\pi}{\lambda} \quad (4)$$

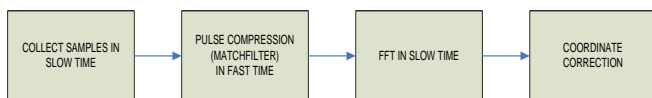


Figure 1. Doppler Beam Sharpening Algorithm

When we differentiate this phase lag with respect to u , we obtain a linear relation with x given by (5). The position of scatterer in azimuth corresponds to a complex sinusoid in slow time and by using the frequency of this sinusoid, we can obtain the azimuth position. By using all the assumptions stated above the simplest image formation algorithm “Doppler Beam Sharpening” can be summarized as stated in Figure 1.

$$\frac{d\Theta(u)}{du} = \frac{4\pi x}{\lambda R} \quad (5)$$

III. DEFINITION AND TYPES OF SAR ECM

SAR ECM can be defined as techniques which prevent a target from imaging, classification and identification of objects on a region by creating distortion or false targets in the resultant image. Possible techniques against SAR are classified as Passive, Non-Coherent, Semi Coherent and Coherent in [11].

Passive techniques include usage of reflectors and surface materials absorbing radar pulses. As stated in [10], by using special materials, a decrease of up to 15 dB in radar cross section (RCS) can be obtained.

In non-coherent techniques, the jam signal does include radar center frequency but does not have any other

correlations with the radar pulse. The jam signal is filtered in both fast time and slow time processing. Noise techniques are included in this group.

In semi coherent techniques jam signal is constructed by using target pulses recorded on Digital Radio Frequency Memory (DRFM) but the phase relation from pulse to pulse is not considered. Fast time match filtering does not decrease jam signal power but the power of the jam signal is decreased during slow time processing.

In coherent techniques, pulse to pulse phase relation is controlled such that the jam signal can pass both fast time and slow time operations with minimum loss. The most important gain in such techniques is that, a false target defined in both azimuth and range direction can be formed, resulting in a deception effect.

All SAR systems have a slow time processing which makes them highly resistive against noise jamming techniques. First, some calculations related to signal to noise ratio (SNR) in SAR receiver are provided. In these calculations, the noise source can be the thermal noise, jammer noise or sum of them.

Assume the azimuth resolution of the system is w_a . The required aperture length for this resolution can be calculated using (6). As shown in [9] two point scatters Δx separated from each other will have a Doppler difference given by (7). The maximum Doppler difference that can occur along the aperture length will correspond to $\Delta x = D_{SAR}$ and this will require a sampling rate of $1/\Delta F_d$. The aperture length is also limited by $\Theta_{az} * R$. By using (1), (6) and (7) we obtain a minimum pulse repetition frequency (PRF) for a system given by (8). The number of pulse returns along aperture can be calculated using (9).

$$D_{SAR} = \frac{\lambda R}{2w_a} \quad (6)$$

$$\Delta F_d = \frac{2v\Delta x}{\lambda R} \quad (7)$$

$$PRF_{min} = \frac{2v}{L_{az}} \quad (8)$$

$$n_c = \frac{D_{SAR} PRF_{min}}{v} = \frac{\lambda R}{w_a L_{az}} \quad (9)$$

$$PCF = PW * BW \quad (10)$$

The SNR gain obtained by pulse compression on range axis can be calculated using the Pulse Compression Factor (PCF) given by (10) where PW is the pulse width and BW is the band width of the SAR pulse.

The SNR gain in slow time processing is equal to the number of pulses processed in slow time n_c . In order to avoid Doppler ambiguities, an over sampling factor K_a is used. This factor is known as “Azimuth oversampling Factor” and has an effect in SNR gain. By combining all factors, SNR gain in SAR receiver is calculated using (11).

$$GAIN_{SNR} = \frac{PW * BW * R * \lambda * K_a}{w_a * L_{az}} \quad (11)$$

$GAIN_{SNR}$ only correspond to SNR gain in receiver. There are other factors effecting the amount of jamming noise power on the receiver system such as the attenuation due to distance between jammer and SAR, positioning of the jammer outside the main lobe of the SAR, mismatch between jammer and SAR frequency bands .

The immunity of SAR receiver against noise jamming is due to the fact that the noise samples sum up non-coherently in SAR receiver. An alternative technique to barrage, spot, pulsed noise techniques is the usage of the same prerecorded noise signal for each pulse. In this technique, a pre-calculated noise sequence is recorded to a memory and used repetitively. This will result in a filtering in fast time however due to pulse to pulse coherency, there will be lines in the resultant SAR image. The effectiveness of this technique will be shown in the simulations section.

In semi coherent techniques, recorded radar pulses are used to generate jamming signal, however the motion characteristics of the platform is not used for transmission timing or modulation of jammer signal. As a result, in semi coherent techniques phase coherency in slow time (azimuth) is not possible. Due to this fact, jamming signal power does not decrease during fast time match filtering but decreases during slow time operations.

Assume a technique similar to false target generation against conventional radar is used. A copy of the radar pulse is transmitted back after a fixed period of time. Since the timing of the jamming pulse is independent of radar position, there will be a scattering in the resultant SAR image. When the delay between pulse arrival to jammer and jam signal transmission is zero, there would be no scattering in resultant image and a single point scatterer in jammer location will appear in resultant image. When the delay between SAR pulse arrival and jam signal transmission is increased, the scattering in resultant SAR image will increase. In other words, if we want to create a single point scatterer with coordinates (R_{FT}, X_{FT}) , then the delay at different platform positions must be ΔT_{FT} . (12)

$$\Delta T_{FT} = \frac{2}{c} \sqrt{(u - x_{FT})^2 + (R_j + R_{FT})^2} \quad (12)$$

Parameters u and R_j (Jammer distance in range direction) are unknown parameters for semi coherent techniques, so they cannot be used while calculating the timing of jammer pulse transmission. An interesting example to semi coherent techniques is described in [12] where a random phase modulation is combined with noise jamming. Another example to semi coherent techniques, named in this paper as random range false target technique, is transmission of a radar pulse copy at random range or ranges. For each PRI, the delay between pulse arrival and transmission varies in an interval $[T_1 T_2]$. By this technique, a region in radar image corresponding to delays $[T_1 T_2]$ can be filled.

Coherent techniques, similar to semi coherent ones use radar pulse as a source for jamming signal generation. Different from the semi coherent case, the platform position is used for jam signal timing, so a coherency in slow time is also possible.

IV. SIMULATIONS

In this section, simulation results regarding effectiveness for different ECM techniques will be provided. The effect of Jamming to Signal ratio J/S is also simulated. The results validate the derivation provided in (11). In these simulations, the SAR system is assumed to be using the ‘‘2D Match Filtering and Frequency Interpolation’’ image formation method provided in [13]. The jammer is assumed to be protecting a region which is defined by a set of point scatterers shown in Figure 2. Each point scatterer is shown with a white dot and assumed to have the same RCS. The jammer location is the center of that region. Some of the SAR parameters chosen may differ from typical SAR systems. The reason for these selections is minimizing simulation run times. The SAR system parameters used in simulations are listed in Table-1. Using these parameters, the SNR gain or noise jamming attenuation in the receiver will be nearly 61 dB.



Figure 2. Set of Point Scatterers in target region

TABLE I. TABLE I SIMULATION SAR PARAMETERS

Center Frequency	1 GHz
Range	4 km
Aperture Length	1300 m
Number of Pulses processed	2470
Azimuth resolution	1.5m
Range resolution	1.25m
Bandwidth	100 MHz
Target Region Width (Azimuth)	200 m
Target Region Width (Range)	800 m

In Figures 3,4,5,6 2D and 3D plots of resultant SAR image magnitudes reconstructed under J/S ratios of 30 dB, 40 dB, 50 dB, 60 dB are provided. Up to the J/S ratio of 50 dB, point scatterers can clearly be selected. For the J/S of 60 dB, point scatterers are not distinguishable and lost in noise, which is an expected result since J/S improvement on receiver was calculated as 61 dB.

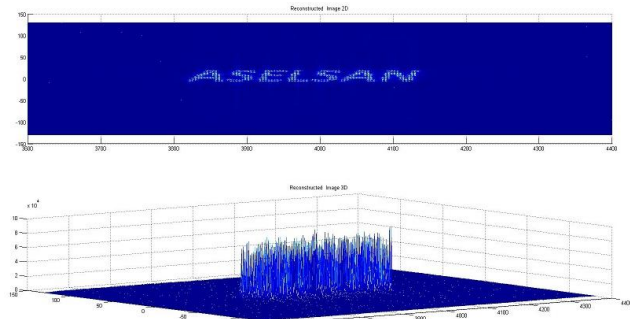


Figure 3. Barage Noise J/S :20 dB

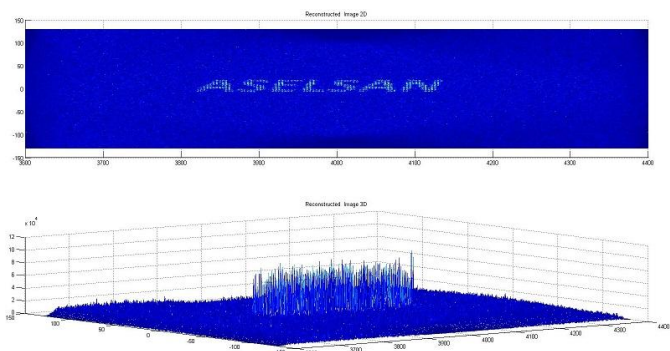


Figure 4. Barage Noise J/S :40 dB

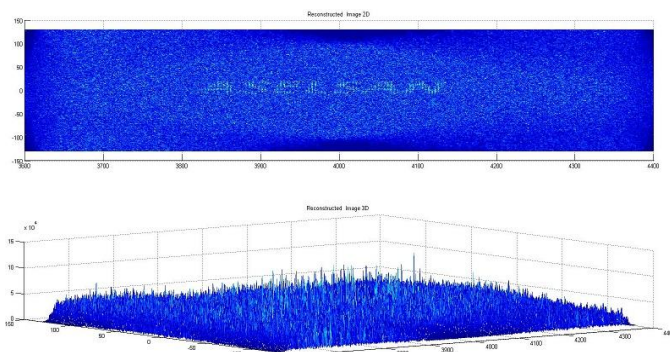


Figure 5. Barage Noise J/S :50 dB

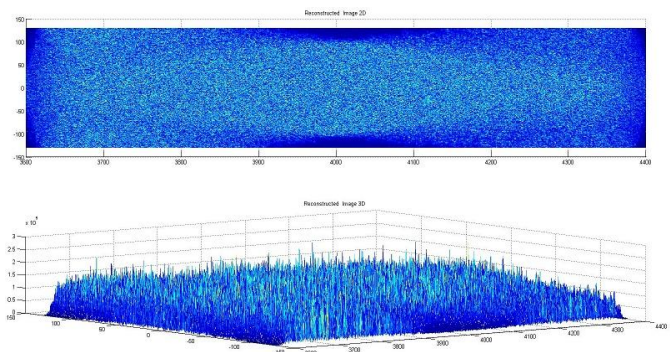


Figure 6. Barage Noise J/S :60 dB

As described in Section IV, a non-coherent noise jamming technique where a prerecorded noise sequence is

repetitively transmitted in each PRI is also simulated. Such a technique would require tracking of SAR pulse timing and a sufficient memory for noise sequence recording. The expected result is a filtering in fast time and obtaining a coherency in slow time. The simulation results provided in Figures 7 and 8 show lines in the resultant SAR image which shows that a coherency in slow time is obtained. Figure 7 shows the resultant image for J/S ratio of 50 dB and Figure 8 shows the resultant image for J/S ratio of 60 dB.

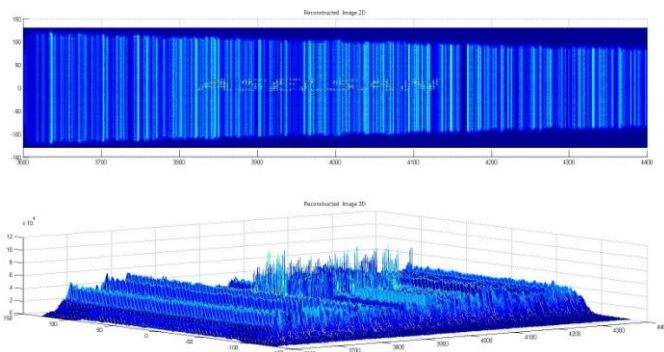


Figure 7. Repeater Noise J/S:50dB

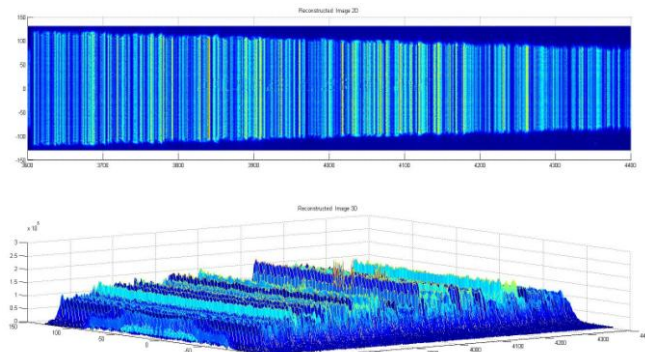


Figure 8. Repeater Noise J/S:60dB

As an example to semi coherent techniques, radar pulses are retransmitted with 16 different delays and the resultant SAR image is shown in Figure 9. As expected, a simple repeater with zero delay will result in a strong point scatterer in jammer coordinate. With an increase in pulse delay, the scattering in azimuth axis increases and the jamming effectiveness decreases due to blurring.

For simulating random delay pulse repetition technique, each radar pulse is delayed and retransmitted with 16 different delays in each PRI. The obtained results are shown for different J/S ratios. Figures 10, 11 and 12 show results for J/S ratios of 20 dB, 30 dB and 40 dB cases. 40 dB J/S case seem to be more effective on SAR system compared to barrage noise jamming case with the same J/S due to coherency in fast time.

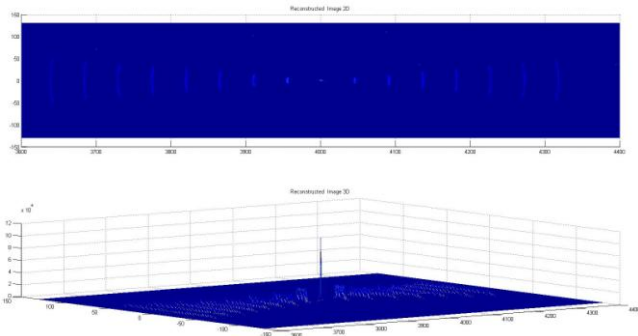


Figure 9. 16 Multiple False Target

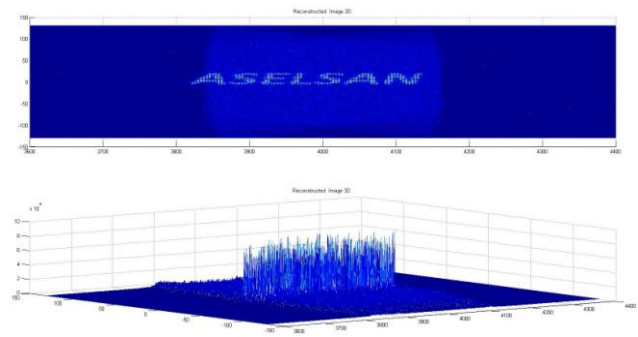


Figure 10. Random Range Multiple False Target J/S:20 dB

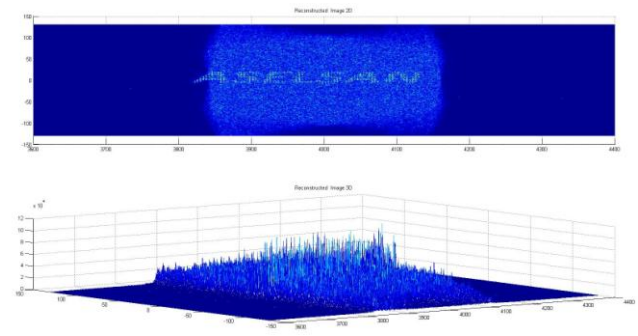


Figure 11. Random Range Multiple False Target J/S:30 dB

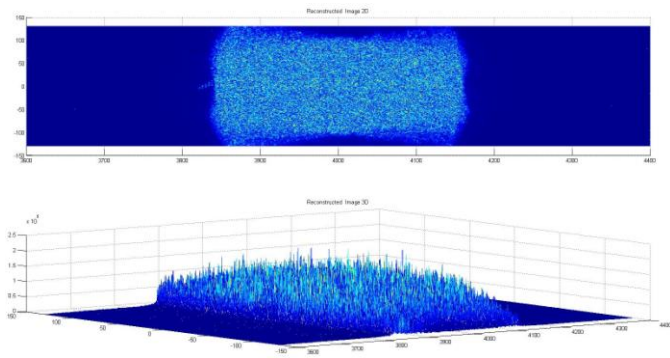


Figure 12. Random Range Multiple False Target J/S:40 dB

V. HARDWARE IMPLEMENTATION

In this section, a hardware structure for implementing SAR jammer will be proposed. The proposed HW structure is shown in Figure 13.

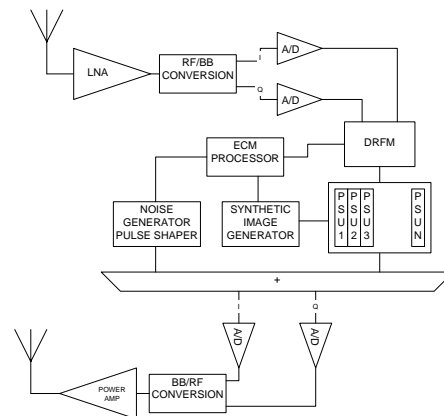


Figure 13. SAR Jammer HW Realization

The jamming techniques described above include generation of noise type and repeater type jamming techniques. Noise type jamming includes generation of pulsed or continuous wave type noise generation in radar band. Deceptive techniques aim to create false images. For this purpose assuming a baseband processing in jammer, the false objects are modeled using a point scatterer array as shown in (13) where $p(t)$ is the radar pulse, g_i is the gain coefficient corresponding to RCS of the scatterer and fd is the frequency shift corresponding to the coordinate of the point scatterer in azimuth axis.

$$J_{PS} = \sum p(t - td_i) g_i e^{j2\pi f d_i t} \tag{13}$$

The proposed HW structure realizes signal processing on a sampled baseband signal. First, the SAR pulse is recorded on DRFM and the main delay corresponding to the difference of delays between SAR to jammer and SAR to false image coordinates is realized on this memory. The false target is separated into point scatterers with different gain corresponding to their RCS, frequency shift corresponding to their azimuth positions and different delay lines corresponding to differences between point scatterer delays. The Point Scatterer Unit (PSU) array in Figure 13 realizes this using multiple PSU units. The outputs of the PSU are summed up and transmitted back to target. A synthetic image generator block continuously updates PSU parameters by using the coordinate estimation of the SAR platform. The number of PSU units is an important performance parameter for the effectiveness of the jammer. In order to have sufficient PSU units, the resource consumption of those units is an important consideration. If the frequency shift is implemented using complex I/Q (In

Phase and Quadrature Phase) data, a complex multiplication with 4 multipliers will be necessary. Similarly, the gain corresponding to RCS of the point scatterer would require 2 multipliers on I and Q channels. Figure.14 proposes a structure for PSU realization, which does not have any multipliers.

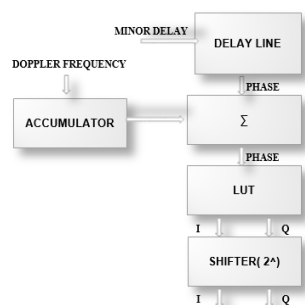


Figure 14. Point Scatterer Unit Realization

The sampled baseband signal is first converted into phase using COordinate Rotation DIGital Computer (CORDIC) algorithm or a low latency Look Up Table based algorithm described in [14] before the PSU array. Each PSU unit has its own minor delay line for compensating delay differences among modelled point scatterers. A frequency shifter, which is realized with an adder and accumulator, adds frequency modulation information coming from the synthetic image generator (SIG) block. The control of noise generator and SIG is done by an ECM processor. The signal in phase format is converted to Baseband I/Q signal using the look up table (LUT). The usage of LUT for phase to I/Q conversion is the main disadvantage in this structure. Assuming a 6 dB gain resolution would be sufficient, the RCS differences between point scatters are realized using shift registers which are controlled by SIG. Another advantage of this structure is the independence of the ECM signal from the SAR signal power due to I/Q to phase, phase to I/Q conversion where the amplitude information is completely lost. For realizing repetitive noise jamming technique, DRFM has a write port from ECM processor so that a pre-calculated noise pattern can be written to and repetitively read out of DRFM.

VI. CONCLUSION

In this study, effectiveness of non-coherent, semi coherent and coherent techniques against SAR radars are compared and some simulations results for those techniques are shown. The advantage of using semi-coherent techniques over non-coherent techniques are shown. A non-coherent technique based on repetitive transmission of pre-calculated noise signal is proposed and the effect obtained with this technique is shown using simulations. The effect of random delay repeater techniques is also simulated for different J/S cases and its area covering effect is shown. A possible HW realization of the SAR ECM generator system is proposed. A structure for false image generator which

uses multiple point scatterers modelling is proposed. For realizing several PSU in the same HW, a simple structure for PSU without any multipliers is proposed and its advantages and disadvantages compared to straightforward implementation are stated.

REFERENCES

- [1] K. Dumper, P.S. Cooper; A.F. Wons, C.J. Condley, and P. Tully, "Spaceborne synthetic aperture radar and noise jamming," *Radar 97* Oct 1997 , pp.411-414 doi: 10.1049/cp:19971707
- [2] R.S. Harness and M.C. Budge, "A study on SAR noise jamming and false target insertion" *SOUTHEASTCON 2014*, March 2014 pp.1-8 doi: 10.1109/SECON.2014.6950729
- [3] X.He, J. Zhu, J.Wang, D. Du and B. Tang, "False Target Deceptive Jamming for Countering Missile-Borne SAR" *IEEE 17th International Conference on Computational Science and Engineering (CSE)*, Dec 2014, pp.1974-1978, doi: 10.1109/CSE.2014.364
- [4] Q. Sun, T. Shu, S. Zhou, B. Tang and W. Yu, "A novel jamming signal generation method for deceptive SAR jammer" *IEEE Radar Conference*, May 2014 , pp.1174-1178, doi: 10.1109/RADAR.2014.6875774
- [5] M. Soumekh "SAR-ECCM using phase-perturbed LFM chirp signals and DRFM repeat jammer penalization" *IEEE Transactions on Aerospace and Electronic Systems*, Jan. 2006, pp.191-205, doi: 10.1109/TAES.2006.1603414
- [6] Y. Chunrui, M. Xile, Z. Yongsheng, D. Zhen and L. Diannong, "Multichannel SAR ECCM based on Fast-time STAP and Pulse diversity" *IEEE International Geoscience and Remote Sensing Symposium (IGARSS)*, July 2011, pp.921-924, doi: 10.1109/IGARSS.2011.6049282
- [7] L. Wei, W. Xingliang and W. Xian-ming, "Anti-jamming techniques for synthetic aperture radar" *IEEE International Geoscience and Remote Sensing Symposium*, July 2009, , pp.IV-605-IV-608, doi: 10.1109/IGARSS.2009.5417449
- [8] W.W.Goj "Synthetic Aperture Radar and Electronic Warfare" *UK Artech House* 1993.
- [9] M. A. Richards, "Fundamentals of Radar Signal Processing", USA: McGraw-Hill, 2005.
- [10] L. Nan and Q. Changwen, "Research on jamming synthetic aperture radar technologies" *Asian and Pacific Conference on Synthetic Aperture Radar*, Nov. 2007, pp.563-566, doi: 10.1109/APSAR.2007.4418674
- [11] Q. Liu, S. Xing, X. Wang, J. Dong, and D. Dai "A Strip-Map SAR Coherent Jammer Structure Utilizing Periodic Modulation Technology" *Progress In Electromagnetics Research B*, Vol.28, 111-128, 2011,doi:10.2528/PIERB10120901
- [12] W.Ye, H. Ruan, S. Zhang and L. Yan, "Study of noise jamming based on convolution modulation to SAR" *International Conference on Computer, Mechatronics, Control and Electronic Engineering (CMCE)*, Aug. 2010, pp.169-172, doi: 10.1109/CMCE.2010.5609875
- [13] M.Soumekh "Synthetic Aperture Radar Signal Processing with MATLAB Algorithms." New York: J. Wiley, 1999.
- [14] R. Gutierrez, V. Torres and J. Valls "FPGA-implementation of atan (Y/X) based on logarithmic transformation and LUT-based techniques", *Journal of Systems Architecture* 2010, pp 588-596

Fast and Efficient Satellite Imagery Fusion Using DT-CWT and WZP

Yonghyun Kim

Dept. of Civil and Environmental
Engineering
Seoul National University
Seoul, Republic of Korea
email: yhkeen@gmail.com

Jaehong Oh

Dept. of Civil Engineering
Chonnam National University
Gwangju, Republic of Korea
email: ojh@chonnam.ac.kr

Yongil Kim

Dept. of Civil and Environmental
Engineering
Seoul National University
Seoul, Republic of Korea
email: yik@snu.ac.kr

Abstract—Among the various image fusion methods, wavelet-based method provides superior radiometric quality. However, fusion processing is not simple or flexible because many low- and high-frequency subbands are often produced in the wavelet domain. To address this issue, a novel dual-tree complex wavelet fusion method that uses wavelet domain zero-padding (WZP) is proposed. Experiments conducted using high-resolution satellite images demonstrated promising results in terms of computation cost.

Keywords—image fusion; dual-tree complex wavelet; wavelet domain zero-padding.

I. INTRODUCTION

Satellite imaging sensors typically supply a low-resolution multispectral (LRM) image and a high-resolution panchromatic (HRP) image separately because of physical and technological constraints [1]. Among the many image fusion methods that are currently available, discrete wavelet transform (DWT) methods provide superior fused images that maintain the radiometric information of the LRM image. Although the DWT-based methods are spectrally consistent, there are two problems. First, DWT is shift-variant and exhibits artifacts because of aliasing in the fused image [2]. Second, these fusion methods have a high computation cost and complexity. The first problem can be overcome by the dual-tree complex wavelet transform (DT-CWT), which is nearly shift-invariant and directionally selective in two or more dimensions [3]. Additionally, if fused data from specific fusion method are nearly identical with other fused data from a more computationally efficient method, the latter method is ideal for a large quantity of remote sensing data. This paper proposes a fast and efficient DT-CWT fusion method to address the second problem. In Section 2, the proposed DT-CWT fusion method is presented and result and conclusion are drawn in Section 3.

II. DT-CWT AND IMAGE FUSION

A. DT-CWT

Kingsbury [4] introduced a new type of wavelet transform known as the DT-CWT, which exhibits a shift-invariant property and improves directional resolution compared with the DWT. The DT-CWT with the complex wavelet function and complex scaling function decomposes

an image into one complex scaling subband and six complex wavelet subbands at each decomposition level.

B. Perfect Reconstruction with WZP

An image can be decomposed into a series of low- and high-frequency subbands using the specific wavelet transform. Perfect reconstruction (PR) means that the final image is the same as the original image. WZP was used to produce super-resolved imagery by filling the unknown high-frequency subbands with zeros and applying the inverse wavelet transform [5]. The WZP method can be conversely applied in image fusion. That is, the known low-frequency subbands can be filled with zeros. Then, by performing the inverse wavelet transform, only a single high-frequency image in the spatial domain is produced. This approach can be applied to the DT-CWT. That is, the low frequency of the original image can be easily discarded. The PR condition and WZP method of the DT-CWT are shown in Figure 1. This approach can be simply implemented as an additive wavelet method.

C. Proposed DT-CWT Fusion Method

The procedure of the proposed DT-CWT with additive-wavelet (AW) fusion method can be summarized as follows:

- 1) Perform histogram matching between the HRP image and intensity image.
- 2) Decompose only the histogram-matched HRP image.
- 3) The low-frequency subbands of the decomposed HRP image are filled with zeros.
- 4) An inverse DT-CWT (IDT-CWT) is conducted to produce the wavelet plane (WP). The WP is the sum of the high frequencies and contains the detailed geometric information of the HRP image.
- 5) The WP is added to the resized LRM image, and finally, the fused HRM image is generated.

This fusion method can produce the same type of fused imagery produced by the conventional AW methods. However, the proposed method is simpler and more flexible in that this method fused in the spatial domain. The method is illustrated in Figure 2.

III. RESULT AND CONCLUSION

In this study, we used WorldView-2 satellite images. In our experiments, the LRM image size was 512×512 pixels, and the HRP image size was 2048×2048 pixels. We

compare our fusion method with DT-CWT with the substitute-wavelet (SW) method [3]. We compared the fusion processing time based on the computation cost. The reported times were measured in the Matlab 2014b environment and on a quad-core 2.5 GHz personal computer platform using the average elapsed time of 20 trials. Table I demonstrates the elapsed time. The DT-CWT with the SW method was very slow because of the decomposition of the LRM image and the substitution process in the wavelet domain. On the other hands, the proposed method is nearly five times faster than the DT-CWT with the SW method. If the histogram matching were performed with each LRM image rather than the intensity image, the elapsed time would be increased in proportion to the total number of bands. Most significantly, the proposed fusion method increases flexibility because the wavelet domain fusion is simplified to the spatial domain by adopting the WZP method. Also, Table II shows the performance comparisons of the fused images. The results indicated that the proposed fusion method provides a less distorted fused image compared with DT-CWT with SW method. Thus, the proposed approach facilitates the general and less computationally intensive fusion method using the DT-CWT.

TABLE I. ELAPSED TIME COMPARISON

Fusion Methods	Elapsed Time (Sec)
DT-CWT with SW [3]	17.2759
Proposed method	3.2554

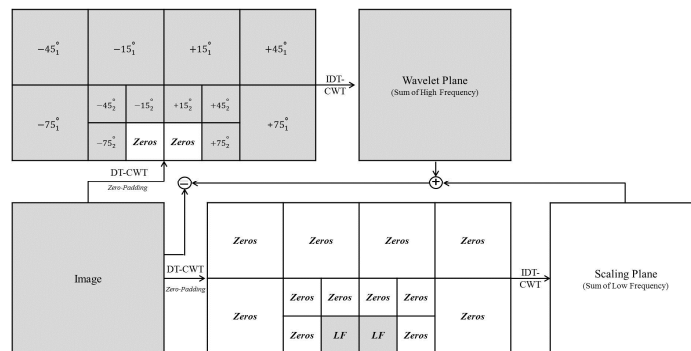


Figure 1. PR condition and WZP of the DT-CWT.

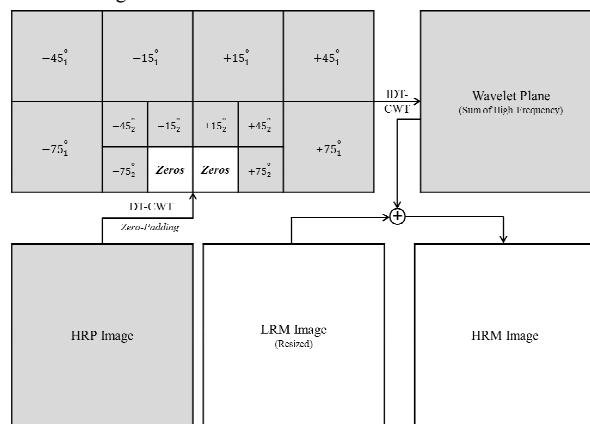


Figure 2. Proposed DT-CWT fusion method with the AW method.

TABLE II. QUALITY INDICES

Fusion Methods	D_i	D_s	QNR
DT-CWT with SW [3]	0.0269	0.0172	0.9564
Proposed method	0.0249	0.0165	0.9590

ACKNOWLEDGMENT

This study was supported by NRF (National Research Foundation) grant funded by the South Korea Government (NRF-2015M1A3A3A02014673, and NRF-2014R1A1A1001995).

REFERENCES

- [1] Z. Wang, D. Ziou, C. Armenakis, D. Li, and Q. Li, "A comparative analysis of image fusion methods," IEEE Trans. Geosci. Remote Sens., vol. 43, no. 6, Jun. 2005, pp. 1391-1402.
- [2] C. Thomas, T. Ranchin, L. Wald, and J. Chanussot, "Synthesis of multispectral images to high spatial resolution: a critical review of fusion methods based on remote sensing physics," IEEE Trans. Geosci. Remote Sens., vol. 46, no. 5, May 2008, pp. 1301-1312.
- [3] S. Ioannidou and V. Karathanassi, "Investigation of the dual-tree complex and shift-invariant discrete wavelet transforms on quickbird image fusion," IEEE Geosci. Remote Sens. Lett., vol. 4, no. 1, Jan. 2007, pp. 166-170.
- [4] N. Kingsbury, "Complex wavelets for shift invariant analysis and filtering of signals," Appl. Comput. Harmonic Anal., vol. 10, no. 3, May 2001, pp. 234-253.
- [5] A. Temizel and T. Vlachos, "Wavelet domain image resolution enhancement using cycle-spinning," Electron. Lett., vol. 41, no. 3, Feb. 2005, pp. 119-121.